UNIVERSITY OF SOUTHAMPTON

FACULTY OF ENGINEERING AND PHYSICAL SCIENCE

Optoelectronics Research Centre

Silicon Mid-infrared Waveguide-based Bio-Chemical Sensors

by

Yanli Qi

Thesis for the degree of Doctor of Philosophy

March 16, 2022

UNIVERSITY OF SOUTHAMPTON

ABSTRACT

FACULTY OF ENGINEERING AND PHYSICAL SCIENCE
Optoelectronics Research Centre

SILICON MID-INFRARED WAVEGUIDE-BASED BIO-CHEMICAL SENSORS

by Yanli Qi

The MIR spectral region contains strong absorption bands for many molecules and substances such as gases, liquids, proteins or drugs. Photonic devices operating in the MIR can be used, for example, in the treatment of aspirin and paracetamol overdose patients to identify and measure the concentrations of drugs in the body. The main aim of the project is to develop the MIR silicon photonic circuits for absorption spectroscopy, to be able to detect the quality and quantity of samples. By analysing the absorption spectra, identifiable absorption peaks and troughs at certain wavelengths can give knowledge of the composition of the sample present and the level of absorption can give information about the samples concentration.

In the first part of this work, a preliminary demonstration of a silicon-on-insulator (SOI) device with a microfluidic channel is carried out in which the absorption spectra of different concentrations of water-IPA solutions are measured at wavelengths between 3.725 μm and 3.888 μm. The devices were used to detect an expected IPA absorption peak at 3.77 μm, and a concentration as low as 1.5% IPA in water (by volume) was detected.

The second part of this work aims to reduce the noise floor. A new on-chip liquid sensor in the mid-infrared wavelength region was demonstrated, which uses Si waveguide switches and a microfluidic channel to allow for the circuit transmission to be switched between a reference waveguide and a sensing waveguide faster than fluctuations due to the noise. The results of this study show that the switch sensor can reduce the noise floor by a factor of 11 compared to a simple waveguide absorption sensor, which would ultimately allow the switch sensor to measure lower concentrations of a target analyte, and to reach a lower limit of detection. In future work, different methods of achieving longer wavelength (7-10 μm) sensing are discussed, with the current progress outlined.

Declaration of Authorship

I declare that this thesis and the work presented in it is my own and has been generated by me as the result of my own original research.

I confirm that:

1. This work was done wholly or mainly while in candidature for a research degree at this University;
2. Where any part of this thesis has previously been submitted for a degree or any other qualification at this University or any other institution, this has been clearly stated;
3. Where I have consulted the published work of others, this is always clearly attributed;
4. Where I have quoted from the work of others, the source is always given. With the exception of such quotations, this thesis is entirely my own work;
5. I have acknowledged all main sources of help;
6. Where the thesis is based on work done by myself jointly with others, I have made clear exactly what was done by others and what I have contributed myself;
7. Parts of this work have been published before submission

Print name: Yanli Qi Date: 08/03/2022

Publications

1. **Y. Qi**, Z. Zheng, M. Banakar, Y. Wu, A. Gangnaik, D. J. Rowe, V. Mittal, J. Butement, J. S. Wilkinson, G. Z. Mashanovich, and M. Nedeljkovic, "Integrated switching circuit for low-noise self-referenced mid-infrared absorption sensing using silicon waveguides," IEEE Photonics Journal, vol. 13, no. 6, pp. 1-10, Dec. 2021.

2. **Y. Qi**, D. J. Rowe, V. Mittal, M. Banakar, Y. Wu, M. Nedeljkovic, J. S. Wilkinson, and G. Z. Mashanovich, "Integration of mid-infrared SOI photonics with microfluidics," Photonics West 2019, Proc. SPIE, vol.10923, p.109230I, San Francisco, USA, 2-7 February 2019.

3. G. Z. Mashanovich, M. Nedeljkovic, J. Soler-Penades, Z. Qu, W. Cao, A. Osman, Y. Wu, C. J. Stirling, **Y. Qi**, Y. Cheng, L. Reid, C. G. Littlejohns, J. Kang, Z. Zhao, M. Takenaka, T. Li, Z. Zhou, F. Y. Gardes, D. J. Thomson, and G. T. Reed, "Group IV mid-infrared photonics," Optical Materials Express, vol. 8, pp. 2276-2286, 2018.

4. G. Z. Mashanovich, J. Soler Penades, Y. Wu, V. Mittal, A. Osman. W. Cao, Z. Qu, **Y. Qi**, C. Stirling, M. Milosevic, L. Reid, D. J. Rowe, D. J. Thomson, M. Nedeljkovic, "Mid-IR silicon and germanium photonic circuits for communications and sensing," IEEE Summer Topicals Meeting, Ft. Lauderdale, FL, USA, 8-10 July 2019. (invited)

5. M. Nedeljkovic, **Y. Qi**, V. Mittal, D. J. Rowe, Z. Qu, Y. Wu, A. Osman, Z. Zheng, C. Wei, James S. Wilkinson, and G. Z. Mashanovich, "Absorption spectroscopy in the mid-infrared using silicon and germanium waveguides," PIERS 2019, Rome, Italy, 17-20 June 2019. (invited)

6. M. Nedeljkovic, J. Soler Penades, A. Osman, **Y. Qi**, D. Rowe, Z. Qu, Y. Wu, W. Cao, V. Mittal, G. Senthil Murugan, A. Z. Khokhar, A. Sánchez-Postigo, J. G. Wangüemert-Pérez, A. Ortega-Moñux, R. Halir, I. Molina-Fernández, P. Cheben, J. S. Wilkinson, and G. Z. Mashanovich, "Group-IV material waveguide devices for mid-infrared absorption spectroscopy," EOSAM 2018, Delft, Netherlands, 8-12 October 2018. (invited)

Publications

7. D. J. Rowe, **Y. Qi**, V. Mittal, A. Osman, Z. Qu, Y. Wu, M. Banakar, J. Soler Penades, A. Sánchez-Postigo, J. G. Wangüemert-Pérez, A. Ortega-Moñux, R. Halir, Í. Molina-Fernández J. S. Wilkinson, M. Nedeljkovic, and G. Z. Mashanovich, "Silicon photonics for mid-infrared sensing," SENSORDEVICES 2018, The Ninth International Conference on Sensor Device Technologies and Applications, Venice, Italy, 16-20 September 2018. (invited)

8. G. Z. Mashanovich, J. Soler Penades, W. Cao, Z. Qu, A. Osmah, Y. Wu, A. Z. Khokhar, C. J. Littlejohns, S. Stankovic, S. Reynolds, V. Mittal, G. S. Murugan, J. S. Wilkinson, **Y. Qi**, F. Y. Gardes, D. J. Thomson, and M. Nedeljkovic, "Group IV mid-infrared devices and circuits," Photonics West 2018, Vol. 10535, p. 1053512, San Francisco, CA, USA, 27 January – 1 February 2018. (invited)

9. M. M. Milosevic, W. Zhou, H. K. Tsang, A. Osman, S. Stankovic, **Y. Qi**, M. Nedeljkovic, Z. Qu, X. Yan, A. Z. Khokhar, G. T. Reed, and G. Z. Mashanovich, "Hyperuniform disordered polarisers for the mid-infrared," CLEO 2019, pp. SW3J-5, San Jose, CA, USA, 5-10 May 2019.

10. C. G. Littlejohns, D. Rowe, H. Du, L. Ke, W. Zhang, W. Cao, T. Dominguez Bucio, X. Yan, M. Banakar, D. Tran, S. Liu, F. Meng, B. Chen, **Y. Qi**, X. Chen, M. Nedeljkovic, L. Mastronardi, R. Maharjan, S. Bohora, A. Dhakal, I. Crowe, A. Khurana, K. Balram, L. Zagaglia, F. Floris, P. O'Brien, E. Di Gaetano, H. Chong, F. Gardes, D. Thomson, G. Mashanovich, M. Sorel, and G. Reed, "CORNERSTONE's silicon photonics rapid prototyping platforms: current status and future outlook," Applied Sciences vol. 10, pp. 8201, 2020.

11. D. J. Rowe, **Y. Qi**, M. Nedeljkovic, V. Mittal, M. Banakar, J. S. Wilkinson, and G. Z. Mashanovich, "Microfluidic silicon photonics for aqueous mid-infrared sensing," NanoBioTech-Montreux 2018, Montreux, Switzerland, 29-31 October 2018.

12. B. Pant, W. Zhang, M. Ebert, X. Yan, H. Du, M. Banakar, D. T. Tran, **Y. Qi**, D. Rowe, V. Jeyaselvan, C. G. Littlejohns, G. T. Reed, and D. J. Thomson, "Study into the spread of heat from thermo-optic silicon photonic elements," Optics Express, Vol. 29, Issue 22, pp. 36461-36468 (2021).

Contents

List of Figures

Acknowledgements

My Ph.D. has been a challenging and exciting journey for me. It has been one I have massively enjoyed though. It has brought a lot of challenging aspects and opportunities to me. Luckily I have had a positive attitude and a variety of support.

I would like to thank Professor Goran Mashanovich, he is the person who has guided me to find the entrance of this long journey. He has taught me how to be calm and have a relaxed attitude to solve problems and work with other people. He also helped with many out of work skills, and has helped me play tennis and learn photography which was a really happy time. The most important is he let me know I should balance life and work, which is an important skill. I also appreciate Professor James Wilkinson. He let me know as a researcher we should not focus on only the end of tasks, but also think of the how, and the why of things, which I've learnt to be very important. Dr. Milos Nedeljkovic is a very smart, hardworking, patient, and kind supervisor. He has given me a lot of supports and guidance such as how to do experimentation, how to analyze data, and how to write a paper. I really appreciate his help and patience. A lot of thanks for my colleagues' support and help too, Dr. Yangbo Wu, Dr. Ahmed Osman, Dr. Zhibo Qu, Dr. Ali Khokhar, Dr. Anushka Gangnaik, Dr. Kian Shen Kiang, Dr. Wei Cao, Dr. Mehdi Banakar, Glenn Topley, Dr. Jia Bi, Dong Wu and Dr. Vinita Mittal. And thanks also to my previous supervisors Khaled Hayatleh, Yali Wang, and Zuochen Wang.

Of course, I need to thank Adam Lewis, thanks for his support, help, and caring to make this journey is much easier, and happier. Also a lot of thanks to my dear friends Xue, Zehong, Di, Amber, Qiu, Xiaoli, Mohamed, and other friends who did not mention here because of the limit of the words... thanks for your friendship to make this journey more wonderful.

Now is good time to say lots of thanks for family. Please allow me to use Chinese to tell them: 亲爱的爸爸妈妈，请允许我在我的博士论文里用文字向您表达我的感谢。谢谢你们的爱和支持让我一直可以保持初心完成了这段非常具有挑战的旅途。现在这段旅程即将结束，我想说："谢谢你们的坚强，善良，和坚韧的品质一直影响着我！"当然，还要谢谢我的姐姐及其家人，谢谢我哥哥及他的家人, 在此也要谢谢我的宝贝们，艺睿，果果，诗哲还有格格，谢谢你们的爱护和支持。希望这场读博旅行也为你们带来了一些美好！

Definitions and Abbreviations

BOX	Buried Oxide
DC	Direct Current
ER	Extinction Ratio
FTIR	Fourier-Transform Infrared Spectroscopy
Ge	Germanium
Ge-on-Si	Germanium-on-Silicon
GPIB	General Purpose Interface Bus
HF	Hydrofluoric Acid
HMDS	Hexamethyldisilazane
ICP	Inductively Coupled Plasma Etching
IPA	Isopropyl Alcohol
LOD	Limit of Detection
MCT	Mercury Cadmium Telluride
MIBK	Methyl Isobutyl Ketone
MIR	Mid-Infrared
MMA	Methyl Methacrylate
MMI	Multimode Interference
MZI	Mach–Zehnder Interferometer
N_2	Nitrogen
NIR	Near-Infrared
NMP	N-Methyl-2-pyrrolidone
PC	Personal Computer
PCB	Printed Circuit Board
PDMS	Polydimethylsiloxane
PECVD	Plasma Enhanced Chemical Vapor Deposition
PMMA	Polymethyl Methacrylate
QCL	Quantum Cascade Laser
RF	Radio Frequency
Si	Silicon
SiO_2	Silicon Dioxide
SOI	Silicon-on-Insulator
TE	Transverse-Electric

TM	Transverse-Magnetic
ZnSe	Zinc Selenide

Chapter 1

Introduction

A biochemical sensor is a system that can decipher biological or chemical information through the use of an external stimulus. This can take the form of an electrical or optical signal and then be measured to obtain quantitative data which can be analysed to learn interesting features about the sample [1] [2][3][4]. Biosensors can detect chemical elements that are related to the environment and humans [5]. Currently, there are many techniques addressing biochemical sensing such as electrochemical and optical techniques.

Electrochemical biosensors are devices which can use electrical parameters such as voltage, current or resistance as a stimulus to detect pH value, glucose concentrations or gas in an environment. As an example, a modern version of glucose sensor which works by measuring current can be seen in figure 1.1. It was able to continuously perform glucose monitoring. The device consists of a reference electrode, a working electrode, a selectively permeable membrane for glucose and O_2 to measure the concentration of glucose [6]. The principle of this device is to use GOx (Glucose oxidase) as a catalyst to help the glucose and O_2 perform a reaction and generate hydrogen peroxide (H_2O_2) in a selectively permeable membrane as equation 1.1 shows. The equation 1.2 shows that then H_2O_2 breaks down at the electrode to produce electrons, which forms a current that can be measured [7]. Comparing this to the reference electrode, the current change between the electrodes is related to the glucose concentrations.

$$Glucose + O_2 \xrightarrow{GOx} Gluconic\ acid + H_2O_2 \tag{1.1}$$

$$H_2O_2 \xrightarrow{electrode} O_2 + 2H^+ + 2e^- \tag{1.2}$$

There are various benefits of electrochemical biosensors such as their ability to work well at low currents, meaning such devices can be portable due to lower power usage, and even be battery powered [8]. However, they have a few shortcomings. Due to the

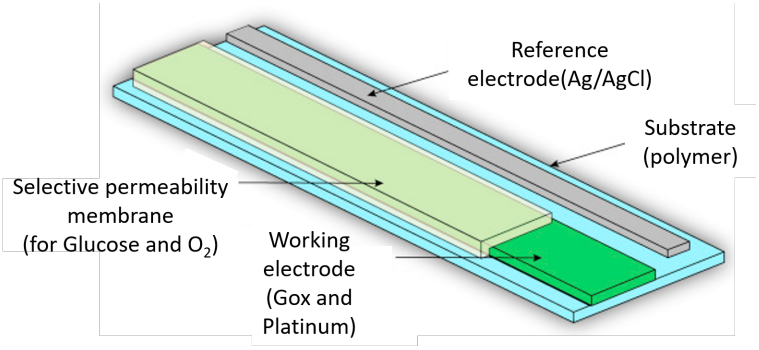

Figure 1.1: The diagram of an amperometric glucose sensor as a kind of electrochemical biosensor using electrodes to measure glucose concentrations through measured current [6].

mechanism by which they work, it takes a long time (potentially 5-20 minutes [6]) to produce a stable current, which can be used to give the final reading of the device. It was reported that for such a device, the mechanical drift of the different components of the electrochemical sensing affects the sensitivity of the measurement [9].

Optical biosensors are able to identify these analytes qualitatively and quantitatively [9]. Optical sensors use light as a signal source, and measure a change such as the absorption of the sample, or the phase shift of the light wave whilst propagating through the medium. It can be used for detection in a variety of applications, such as gas sensing, glucose sensing, chemical liquid sensing and therapeutic drug dose measurement.

Optical sensors are known to produce extremely quick response times, with some experiments producing results in the sub 1 second region. They also benefit from minimal drift, are able to detect separate gases efficiently and some have even been observed to detect with ppq (part per quadrillion) capabilities [10]. These factors allow for quick and reliable results. Compared to optical biosensors, electrochemical biosensors need a stable pH environment [11], and are easily affected by external features such as temperature, voltage and stress [2]. Optical biosensors offer a highly sensitive, rapid, potentially low-cost and non-destructive alternative. Currently, they are more frequently used in research because in the mid-infrared wavelength range they work at the technology of the laser, the waveguide, and the detector are not developed maturely enough to be integrated into a small package. After solving this issue, optical sensors have the potential to be able to be made commercially.

1.1 Optical sensors

Optical sensors are based on the interaction between light and a sample, such as absorption effects [12], refractive index changes, and signals from characteristic Raman scattering [13]. Raman spectroscopy is usually used to detect the vibration mode of

molecules, but Raman scattering is extremely weak in the MIR wavelength region [14]. Raman spectroscopy is a really useful tool for the interrogation of samples, however, it requires expensive equipment, and is not easily maneuvered. The refractive index spectroscopy is a technique measuring the refractive index of the sample, while absorption spectroscopy is used to measure the absorption of a sample. For biochemical sensing, absorption spectroscopy can provide the absorption spectrum to identify what is present and can also measure the concentration of the analyte.

1.2 MIR absorption spectroscopy

Absorption spectroscopy in the mid-infrared (MIR) wavelength region has a variety of potential applications [15] including atmospheric monitoring [16], detection of chemicals and explosives [17], human breath analysis [18], non-invasive glucose monitoring [19], and plant and crop science [20]. Absorption spectroscopy can provide unique spectra to identify substances present in a sample and can also measure their concentrations [21], based on the Beer-Lambert Law [22].

MIR absorption spectroscopy is based on the fact that different molecules have well characterised absorption peaks in the MIR wavelength region (2.5 μm to 20 μm). The MIR spectral region contains strong absorption bands for many molecules (see figure 1.2). Making use of existing experimental set ups, this project will focus on the 3.725-3.888 μm and 6-10 μm wavelength range. The limitations of absorption spectroscopy are that absorption spectroscopy is affected by the light source's spectral range, the absorption of other materials during measuring (waveguide platforms, claddings), and the photodetector wavelength range.

MIR absorption spectroscopy sensing could be used in the treatment of drug (Aspirin, Cocaine) overdose patients to identify the drug and measure its concentration, as well as therapeutic drug monitoring. Usually, in hospitals, a sample needs be taken from the body and sent to a lab for analysis. In some cases this procedure requires a long time for measurements and needs professionals to operate the tools. In addition, current measurement apparatuses are bulky and not convenient for moving to a place of need. MIR spectroscopy can also be used for gas sensing (e.g. CH_4), and in food safety diagnostics (acetic acid, mycotoxin). MIR absorption spectroscopy is important for clinical treatment and environmental monitoring, which can improve the quality of human life.

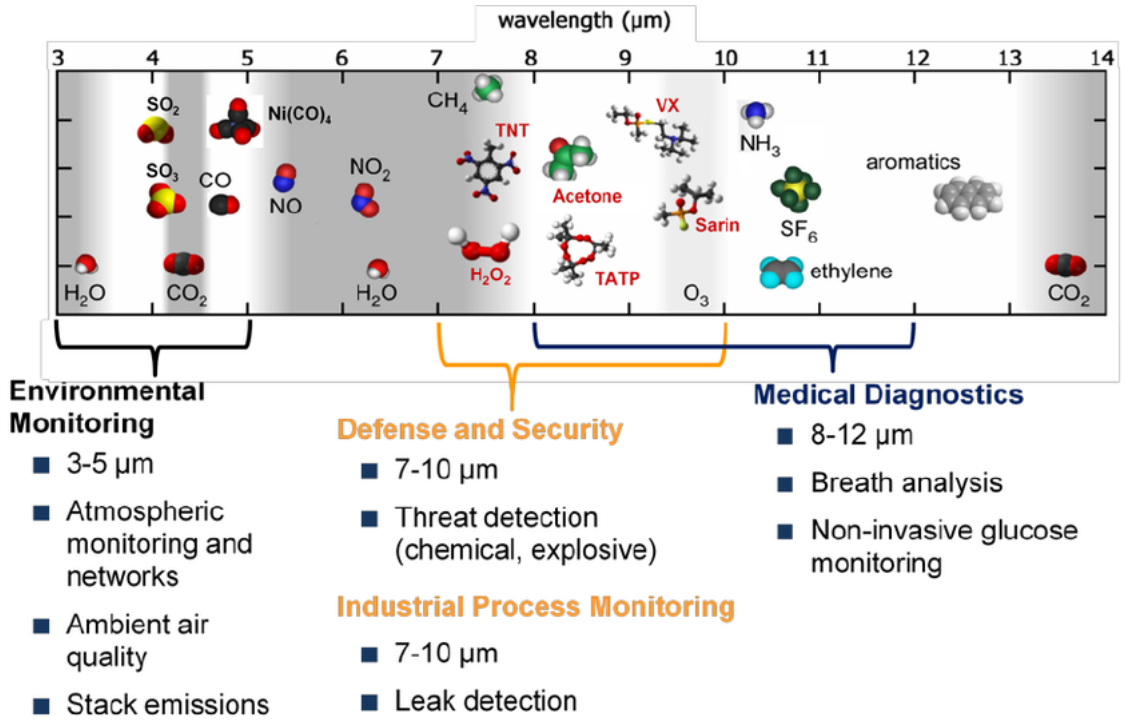

Figure 1.2: The transmission windows and some of the applications within the MIR region [15].

1.3 Enhanced waveguide MIR absorption spectroscopy in silicon photonics

On-chip waveguides which work through the mechanism of MIR absorption spectroscopy, are able to achieve the requirements highlighted in section 1.2, such as the production of unique spectra for the identification of analytes within a mixture. Moreover it also could significantly minimise dimensions, reduce the costs of manufacture and could also enable non specialists to operate diagnostic tools [23]. A future can be envisaged whereby such waveguides are integrated with other devices such as smart phones or watches, allowing for quick and easy diagnosis.

The performance of MIR absorption spectroscopy using waveguides is dependent on the waveguide platform used. Waveguide platforms should have wide transmissions in the MIR wavelength region, the material should be mechanically and chemically stable in contact with a sample, and should also have an easily deposited cladding layer which could be used for bonding microfluidic channels and opening different interaction lengths. Silicon photonic waveguides can have low loss in the MIR and can be fabricated using mature fabrication processes that result in high yield, small footprint and cost, and potential for photonic-electronic integration. These features can improve the possibility of realising sensors with small size and high sensitivity.

Microfluidic channels have been widely used to guide and deliver analyte samples to a sensing area and for more controllable interaction lengths in sensing measurements. They can also be used to avoid the evaporation of the liquid sample and make measurements repeatable. The most widely used material for microfluidic channels is Polydimethylsiloxane (PDMS), because it can be easily moulded and made using mature fabrication processes.

1.4 Project objectives

The principle of this project is based on the Beer-Lambert law [24], which is that the absorption of molecules at a specific wavelength can cause the attenuation of light. This research work aims to develop a device to measure mid-infrared absorption spectra of analytes, which can be used to detect the presence of a particular substance in the sample and can also quantify its concentration. The main aims of this project are to measure the spectra and concentrations of samples to realise highly sensitive, repeatable optical devices based on waveguides, working at the MIR wavelength range. Single analyte solutions are used for testing, meaning selectivity of the analyte is not considered in the scope of these works. This will be done by completing the following:

1. Integration of waveguides with microfluidic channels.

2. Finding proper claddings for different wavelength ranges; the claddings will protect the waveguide surface and will be also used for bonding of microfluidic channels.

3. Demonstration of chemical sensing for the realised integrated devices, using IPA as an example analyte.

4. Improvement of the signal to noise ratio by adding switches into the photonic circuit.

1.5 Thesis outline

This work will describe the integration of mid-infrared (MIR) silicon photonics with PDMS microfluidics to perform absorption spectroscopy of analytes. There are six chapters in this thesis: (1) introduction, (2) background, (3) silicon waveguides integrated with microfluidics for IPA sensor, (4) integrated switching circuit for low-noise self-referenced mid-infrared absorption sensing using silicon waveguides, (5) suspended Si with sub-wavelength waveguide and Ge-on-Si waveguide for sensing, (6) conclusions and future work.

Chapter 2 describes the background of MIR absorption spectroscopy, which includes methodologies and principles. Different spectroscopy methods such as on-chip spectroscopy and Fourier Transform Infrared (FTIR) spectroscopy are discussed, followed by the introduction of several MIR platforms. These include both shorter (up to 4 μm) and longer (7-10 μm) wavelength ranges, such as SOI, Ge-on-Si and suspended waveguides. The theory behind the usage of a thermo-optical switch is also introduced, with the methods by which it could be integrated into a sensing device outlined. MIR absorption spectra of water, IPA, paracetamol and aspirin are also presented at the end of this chapter.

Chapter 3 presents experimental work on silicon waveguides integrated with microfluidics for mid-infrared evanescent absorption spectroscopy, at the short wavelength range (3.725-3.888 μm). For this wavelength range, the 500 nm SOI waveguide was simulated, fabricated and characterised, and used to measure the absorption of IPA and water solutions. The spectra of measured water-IPA solutions of different concentrations are plotted and discussed.

Chapter 4 develops on the work in chapter 3. Switches are integrated with the waveguide to make a circuit that can improve the sensitivity of detection of IPA in water. In this chapter, the theory of how the circuit operates is presented, and the device design, fabrication, experimental setup, and experimental results are also shown.

For the longer wavelength region (7-10 μm), the suspended Si and Ge-on-Si waveguides are described in chapter 5. The discussion on the waveguides, which includes simulation, mask design and the fabrication, is given.

As the last chapter, chapter 6 gives a summary of the experimental work and also describes future plans for improving performance of the devices presented.

Chapter 2

Background

Absorption spectroscopy sensing takes advantage of different molecules having different absorption peaks at different wavelengths. The molecule consists of atoms and bonds, and the bonds are used to connect the atoms. When the bonds are excited by infrared light which has the same frequency as the bond's vibrational frequency, the light will be absorbed, and the molecule will be excited from ground energy state to a higher energy state (excited state) as shown in figure 2.1 [25][26]. The absorbed energy transfers to vibrational energy when the light is in the mid-infrared wavelength range [27]. When the light is in the far-infrared wavelength range, the absorbed light energy will become rotational energy [28]. For the near-infrared wavelength range, emissions from ro-vibrational spectroscopy of overtone and combination bands are measured. These arise from the fundamental absorption resonances present in the MIR [29].

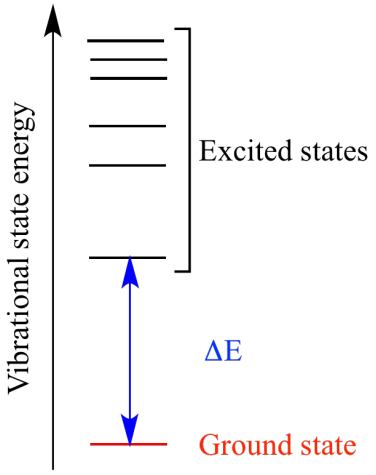

Figure 2.1: The absorption energy Δ E causes the molecule transfer from a ground state to a vibrational excited state [25].

2.1 Methodology of MIR absorption spectroscopy

Three well known methods of MIR absorption spectroscopy will be presented: Fourier-Transform infrared spectroscopy, QCL (Quantum Cascade Laser) absorption spectroscopy and on-chip (waveguide-enhanced) absorption spectroscopy.

2.1.1 Fourier-transform infrared spectroscopy

Fourier Transform Infrared (FTIR) spectroscopy is a technique for measuring IR spectra of solids, gases and liquids, and to identify chemical samples via absorption. The basic components of an FTIR are a broadband light source and a Michelson interferometer with a moving mirror.

As figure 2.2 shows, the method of obtaining a spectrum with FTIR is that when light from a broadband source goes through the beam-splitter, a part of the light is reflected to a fixed mirror (beam A), and a part (beam B) is transmitted to a movable mirror. Then the reflected light from the fixed mirror and movable mirror are recombined at a beam-splitter, and the result reaches a detector.

The distance between the fixed mirror and beam-splitter is constant, while the distance between the movable mirror and beam-splitter is changing, and this condition results in constructive and destructive interference for different wavelengths. The molecules of the sample will absorb specific wavelengths, causing the detected signal to contain characteristic absorption bands. The results from the detector are processed using a Fourier Transform.

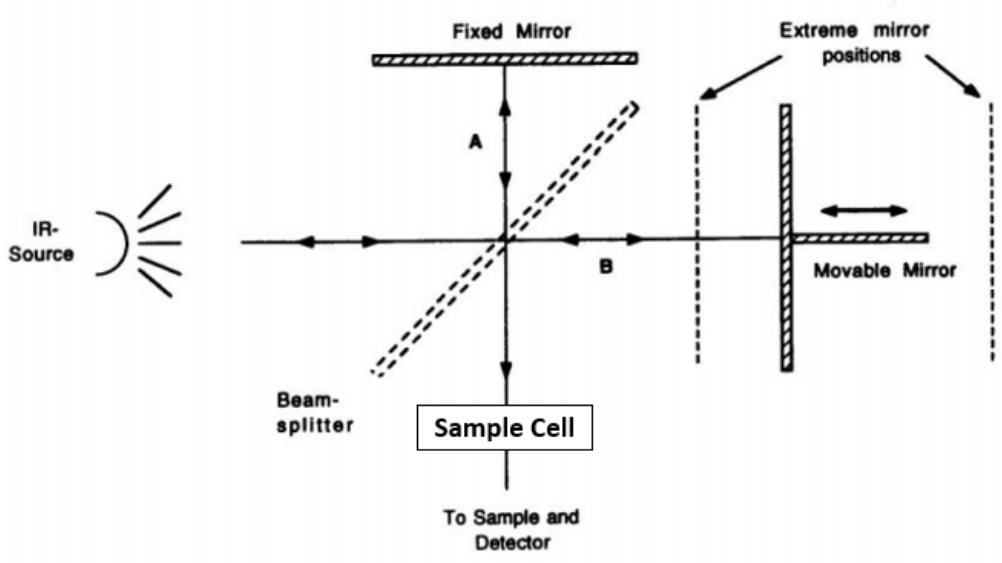

Figure 2.2: The basic schematic block of Michelson interferometer in FTIR [30].

Figure 2.3: Agilent Cary 600 series FTIR Spectrometer operating from near-IR to far-IR [31].

The advantages of the FTIR technique are that it is label-free meaning that it causes no damage to the sample, and it is a quite mature technology [32]. The light source normally used are lamps which are not expensive and can generate a wide range of wavelengths. For example, a tungsten-halogen lamp is used for shorter wavelengths [33]. For longer wavelength ranges, the lamp used is typically a mercury lamp [34]. An example of a commercial FTIR device is shown in figure 2.3. A limitation of FTIR is that the sample usually requires some surface treatment to ensure good transmission qualities. This can be countered with the use of ATR-FTIR which uses a crystal as a base, and instead measures reflectance. This allows for liquid samples to be easily tested. However, if the refractive index of the sample is larger than that of the crystal, the measured IR intensity is too low [35].

2.1.2 Tunable QCL mid-infrared chem/bio sensors

Tunable QCL MIR chem/bio sensors are normally based on only using an open path 'QCL - detector' configuration. For the QCL-detector system, a QCL is used as a light source, which lets the light interact with the sample (gas or liquid). After the light is absorbed by the sample, at the end, the detector or power meter will collect the rest of the light. Normally, a beam splitter will be used to split light into two parts. One part goes through the analyte, and it is then collected by PD1 (photodetector 1). Another

part goes to a reference detector (photodetector 2) to check the stability of the optical signal (figure 2.4).

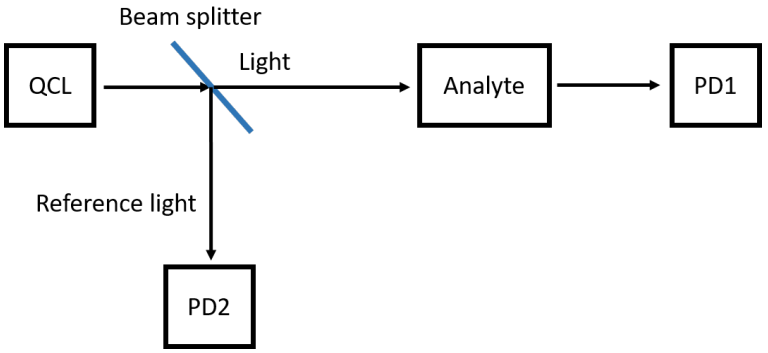

Figure 2.4: QCL-detector sensor with a reference photodetector (PD 2).

For example in [36], an open path system with QCL and detector was used to measure the concentration of ozone and other gases at the 9.3 - 9.81 μm wavelength range. The open path was an interaction length, which for the O_3 gas measurement was 76 m.

Figure 2.5 shows the QCL open path system structure with a QCL as a light source (9.3 - 9.8 μm, Daylight Solutions Inc.). Firstly the light was split into two parts: a few percentages of light reached the yellow coloured detector at the top of the figure (a liquid-nitrogen-cooled detector), which was used to monitor the stability of the QCL source as a reference detector. Most of the light was transmitted to a beam expander that can make the beam diameter 10 times bigger which can reduce the beam divergence and enables longer path lengths. Then the light goes though the open path via an elliptical flat mirror and is reflected by a corner-cube mirror. The output light was directed onto a retroreflector placed a distance of 76m from the laser source for O_3 measurements, propagating through air. During the open path propagation, the light interacted with the gas. The reflected light was received by a telescope and another elliptical flat mirror, and finally collected at the red coloured detector (a thermoelectrically cooled mercury cadmium telluride (MCT) detector). A diode laser was used to align the QCL beam. The O_3 absorption spectrum measurements took 8 minutes to collect sufficient data, limited by the capabilities of the computer controller. The total experiment ran for 10 weeks and was continually running for 24 hours per day highlighting the stability of the laser source.

Ozone levels in Beijing were measured at room temperature, in the 0-150 ppbv (parts per billion by volume) range. As figure 2.6 shows, the O_3 concentration data were recorded for five days by the QCL open path system and an unnamed commercial sensing instrument [36]. During this monitoring, the QCL sensing system measured peaks of O_3 concentrations agreed well with the data from the commercial sensing instrument which proved the QCL sensing was reliable and repeatable.

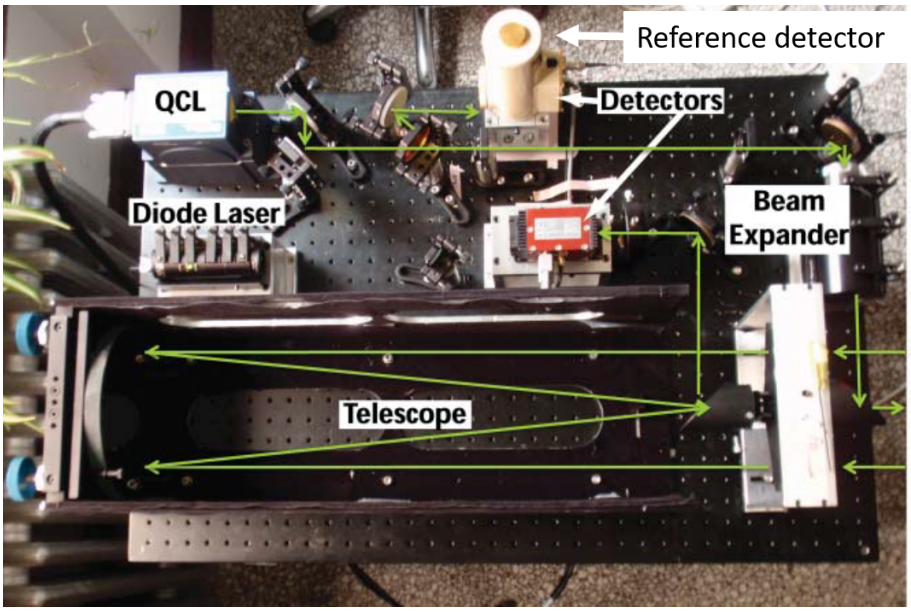

Figure 2.5: The quantum cascade laser open-path system for measuring trace gases in free space [36].

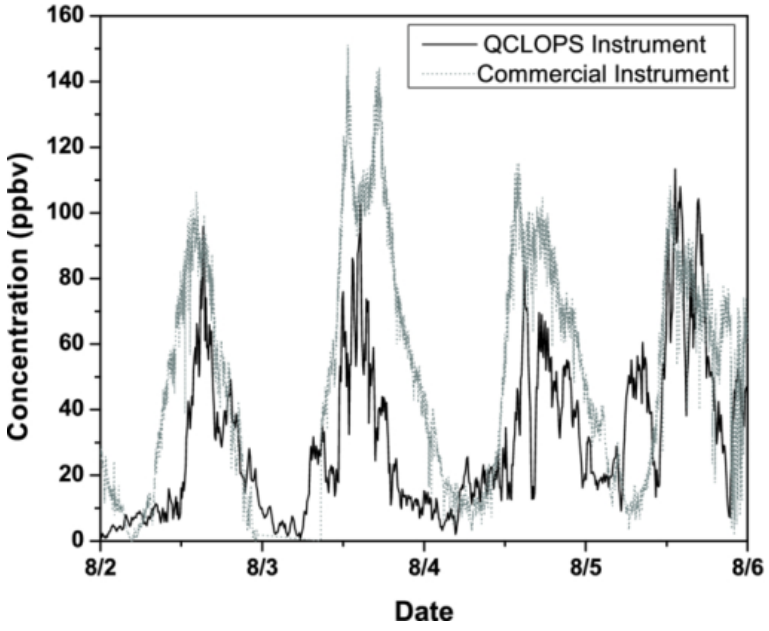

Figure 2.6: The concentration spectra of O_3 measured over five days using a QCL open path system (QCLOPS) and a commercial instrument [36].

Compared to FTIR, the advantages of QCL sensors are easily changing path length, and repeatability for air quality measurement. However, to reliably measure low concentrations, the QCL laser sensor requires a long open path (76 m for O_3 in this case), which results in large dimensions of the whole system and larger noise. Realistically, for liquid samples, a much shorter path length is needed due to the differences in particle density of liquids and gases. There is also the limitation that the large path length would not be easily feasible for liquid samples. Instead, other mechanisms that are able to maintain a

large path length, but a small total size should be considered. One such technique could be to use a spiral waveguide to replace the open path. This will give the device a small footprint as the dimensions of the system can be reduced. By using a waveguide device, the light is confined mainly to the waveguide with a small percentage interaction with the sample. However, it benefits from ease of alignment, and more control of the guided light. It would therefore be expected to have less noise.

2.1.3 Figures of merit for sensing devices

In the evaluation of the quality of sensing devices, there are a few key figures of merit to take into account. Foremost of these is the limit of detection (LOD), which essentially tells us the lowest sensitivity that a sensing device is able to detect between an analyte and a host solvent. A high quality device can usually be described as having a low LOD, or high sensitivity. One method to achieve this is for the device to have a low loss. Here, loss is described as the difference in the output and input power of such a device. In most photonic circuits, loss is seen as a negative aspect, as essentially power is lost. However, in sensing devices there must be the consideration that loss occurs due to interaction with the sample. So ideally a small amount of loss is needed (to ensure we have sample interaction), but not too much as this would greatly diminish the quality of the results. A further figure of merit to consider is the signal to noise ratio. When observing the transmission change when the analyte is introduced to the system, the noise of the spectra can sometimes hide intensity drops. It is therefore key to minimise the noise in the system, and have a low signal to noise ratio. In real world applications, measurements may need to be taken quickly, so recording the time taken for sensing is another key point of evaluation in such devices.

Other aspects of the device must also be considered for ensuring the device is up to standard for real world applications. These are more qualitative measurements. Factors such as the repeatability of measurements, the controllability of the liquid analyte and the ability to clean devices are worth considering. These figures of merit will be further discussed in the literature, and be evaluated in device created in this project.

2.1.4 On chip MIR absorption spectroscopy with tunable lasers

A tunable QCL mid-infrared sensor can use a waveguide to guide light and a sample/analyte is placed on the surface of the waveguide and the basic configuration of it is ‘QCL - waveguide - detector’. The principle of this sensor is usually based on absorption effects of the sample on the evanescent field [37] of the optical mode in the waveguide [23]. The evanescent power determines the absorption effects with the chemical material and also influences the interaction with the waveguide cladding layer (figure 2.7). As is known

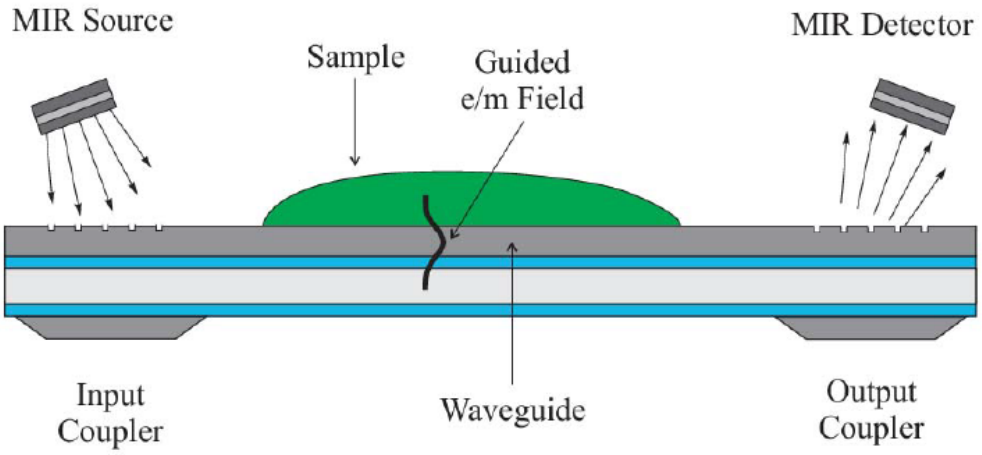

Figure 2.7: Evanescent field waveguide absorption sensing in the MIR [38].

that in the MIR region, different samples absorb at different wavelengths. The Beer-Lambert law can describe this relationship between the concentration of the chemical sample and optical signal power received by the detector [24]:

$$P = P_0 exp(-\eta \varepsilon C L - \alpha_{prop} L) \tag{2.1}$$

where P is the optical signal power, the input power is P_0, η (%) is the evanescent power factor and ε is the molar absorption ($Lmol^{-1}cm^{-1}$). C and L stand for the concentration (mol/L) and optical path length (cm) respectively, and α_{prop} (cm^{-1}) is the intrinsic optical propagation loss from the waveguide. The increase of attenuation of the signal power is associated with higher concentration of the chemical substance and evanescent power factor η (%). The evanescent power factor η (%) is given by the following equation [39]:

$$\eta = \frac{P_{sup}}{P_{total}} \tag{2.2}$$

where P_{sup} is the optical power in the superstrate media [39], and P_{total} is the total guided optical power.

In this project, focus is placed on measuring concentrations (C) of samples whilst using different optical path lengths (L). Theoretically, the longer optical path lengths can detect lower concentrations of samples, however they introduce larger optical propagation loss from the waveguides (α_{prop} (cm^{-1})). Table 2.1 discusses the expected impact of tuning various parameters in sensors design.

A discussion of previously reported research work will now be shown. Figure 2.8 [23] shows a germanium-on-silicon nitride waveguide that was used with a tunable QCL and a bonded fluidic channel to measure the concentration of IPA (analyte) in acetone

Parameter	Change to Device Performance
Optical path (L)	If the optical path is larger, the sensitivity of the device will be higher. A longer optical path means more analyte can interact with light, leading to an increase in absorption from the analyte.
Waveguide loss (α_{prop})	If the waveguide loss is smaller, the sensitivity will be better. At constant input light power, if the waveguide loss is small, then light will be able to achieve a longer optical path. As above, a longer optical path will produce a larger absorption of the analyte, leading to better sensing ability.
Evanescent power factor (η)	If the evanescent power factor is larger, the sensitivity will be higher. It means more light can interact with analyte. However, if this factor is too large, the mode will be poorly guided in the waveguide, meaning it will be hard to obtain high quality results.
Wavelength (λ)	If the wavelength changes, the selectivity of the sensing will be affected. Different analytes have different absorption peaks, so ensuring the wavelength is correct for the chosen sample is key.

Table 2.1: Summary of the expected impact of tuning various parameters in sensor design.

(solvent). The lowest concentration of IPA in acetone was 5% and the authors also measured the IPA and acetone absorption spectra. The limitation of the device is the noise floor of the system, with a theoretical limit of 4.5% due to the signal to noise ratio. Also, the minimum concentration measured is quite large, taking into account that acetone does not have very large absorption at this wavelength ($\sim$ 3.8 μm). In addition, considering the dimensions of the sensing chip, the spiral waveguide can be used to reduce the footprint and increase the interaction length (see figure 2.8). The total length of the 260 $\times$ 260 μm sensing area was 4.02 mm and it is smaller than the length of FTIR and QCL free space sensors. The loss of the waveguide was 7.86 dB/cm which is not ideal [40] (the effect of the waveguide loss and an ideal value of this loss will presented in section 2.2.1).

Another research work [41] also presented an IPA spectrum at 2.6 to 3.7 μm, with ZnSe (zinc selenide) on silicon waveguides (figure 2.9). The authors did not choose a fluidic channel, but used a filter paper instead. The spectra were slightly different than the theoretical ones and they also detected the lowest concentration of IPA in water of 20%. The interaction length was 3 mm which was shorter than the length reported in [23]. It is possible that a microfluidic channel could have helped to improve the accuracy, because it can reduce the evaporation of the IPA. Also the filter paper had a thickness of 3 mm, but the glass thickness was 6 mm, so it was unclear that the interaction length was exactly 3 mm. Using a cladding region to open a sensing window should reduce the error in the interaction length.

On chip tunable QCL MIR absorption spectroscopy sensing can result in more controllable sensing. However, the FTIR uses a broad band light source and can achieve

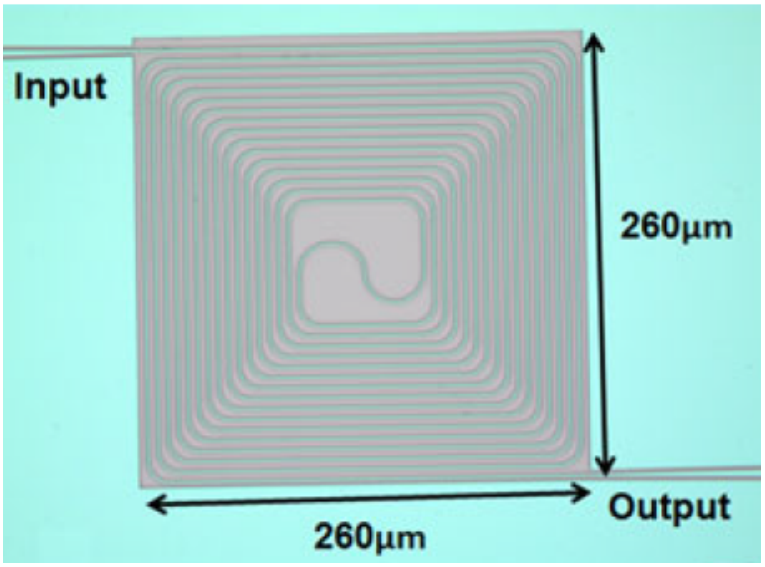

Figure 2.8: The top view of the spiral waveguide on Ge-on-SiN platform for mid-IR sensing applications [23].

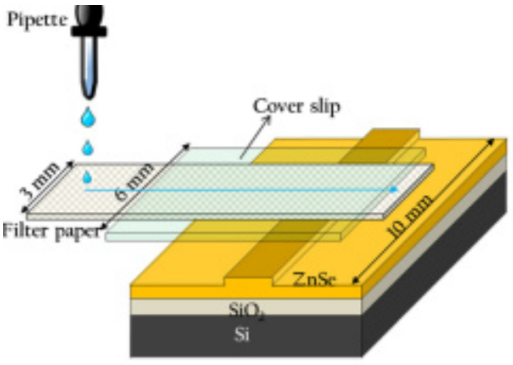

(a)

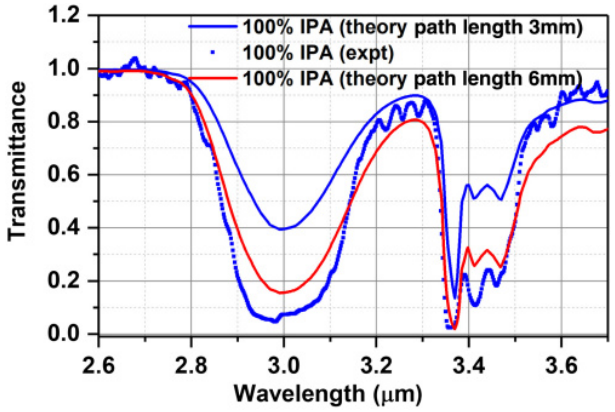

(b)

Figure 2.9: (a) Illustration of the waveguide assembly. (b) Transmission spectra of pure IPA with experimental and theoretical results [41]

.

larger spectral range. On the other hand, considering the size of the sensor, FTIR systems are larger than on chip MIR absorption spectroscopy devices meaning they are less applicable to on demand testing of samples.

Another advantage of the on-chip absorption spectroscopy sensor is a controllable mode profile. Because the evanescent field is dependent on the dimensions of the waveguide, sensitivity and other sensing parameters are controllable.

2.2 Mid-infrared platforms for on chip absorption spectroscopy

2.2.1 Group IV materials for MIR

As was mentioned in the previous section, the waveguide loss is related to sensing performance, because lower loss of a waveguide means a higher signal can be delivered to a detector. The waveguide loss is dependent on the waveguide material and geometry. The most attractive material platform in group IV photonics in the near-infrared (NIR) is silicon-on insulator (SOI), but silicon dioxide has high absorption beyond 4 μm and Si has high absorption for $\lambda > 8\mu$m (see figure 2.10) [40]. That is why for short MIR wavelengths the SOI platform can still be used, but for longer wavelengths in the MIR alternative materials are needed [42], such as suspended Si where the lossy oxide has been removed, or Ge-on-Si.

Recently, the properties of group IV devices based on Ge-on-Si (germanium-on-silicon) platforms have been investigated, due to its performance qualities such as excellent transmission, high refractive index contrast, and low cost.

In this section, SOI waveguides, Ge-on-Si (GOS) waveguides and suspended Si waveguides will be outlined from material, structure, operating wavelength and performance points of view.

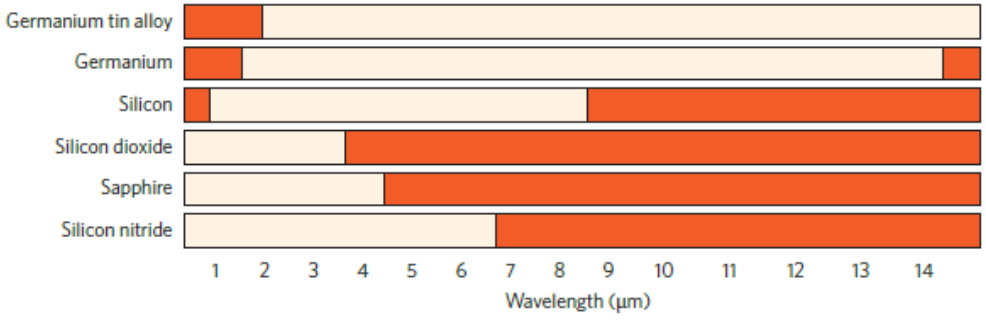

Figure 2.10: Infrared wavelength ranges over which waveguide propagation loss is less than 2 dB/cm. The light areas present optical transparency, the dark areas signify high loss [40].

2.2.1.1 Group IV waveguides operating at short MIR wavelengths

For short MIR wavelengths (up to 4 μm), strip, rib SOI, and slot waveguides, 3000 nm thick Ge-on-Si rib waveguides and 850 nm thick Ge-on-SOI waveguide have been reported.

Rib SOI waveguides at 3770 nm

A 400 nm rib SOI waveguide was designed with 220 nm etch depth, the width was 1.35 μm, and it operated at a wavelength of 3.77 μm in a single mode. The propagation loss was 1.46 $\pm$ 0.2 dB/cm which is acceptable. The fabrication process involved e-beam lithography with ZEP-520A and dry etching with an Oxford Instruments ICP (Inductively Coupled Plasma Etching) 380 plasma tool [43].

The benefit of low propagation loss waveguides is that they can be used with long path lengths for sensing. However they still suffer from loss, hence further improvements need to be made. One option is to remove the silica, to make the rib waveguide as a suspended waveguide that can reduce the propagation loss (as the silica has high absorption in MIR range). However, this additional fabrication step to remove the silica can weaken the structure of the waveguide meaning it can be fragile to work with.

The other option is to reduce the interaction of light with the side walls which can have high surface roughness. To do this, we can decrease the etch depth. However, this will increase the bend loss, as the mode will become less confined particularly in bends. Therefore, for a device that is a straight waveguide, choosing a shallow etch will be the best configuration to fabricate.

Strip SOI waveguides at 3770 nm

A 500 nm strip SOI waveguides was also demonstrated as well as a library of passive devices operating at 3.77 μm. They were fabricated with the same fabrication steps as the 400 nm SOI waveguides. The loss was similar, at 1.28 $\pm$ 0.65 dB/cm. The waveguide width was 1.3 μm so slightly narrower than the 400 nm rib SOI waveguides [44]. Since the 500nm SOI strip waveguide is larger than the 400 nm rib waveguide, the mode was more confined in the core resulting in slightly lower propagation loss. This can however, also reduce the sensitivity of a sensor based on evanescent wave absorption.

Slot waveguides at 3800 nm

For a SOI (Silicon on insulator) slot waveguide, there is a slight distance between the two Si tracks which is named the gap (figure 2.11). The optical mode can be confined in the air gap [45], and SOI slot waveguides can improve the sensitivity as the electric field amplitude in the gap can be increased up to 50 times, compared to the evanescent-wave sensing (figure 2.11) [46]. A slot waveguide was designed as a 2D waveguide with a height of 500 nm, width of 1300 nm, and gap of 78 nm in the middle. The propagation loss at 3.8 μm was quite low (1.4 $\pm$ 0.2 dB/cm) and the loss of transition from strip to slot waveguides was only 0.09 $\pm$ 0.01 dB/transition [47]. The main problem of this

structure is the very high electric field confinement in the slot, which then has a high overlap with any roughness of the Si surface in the slot. The propagation loss of the waveguides can therefore be easily affected.

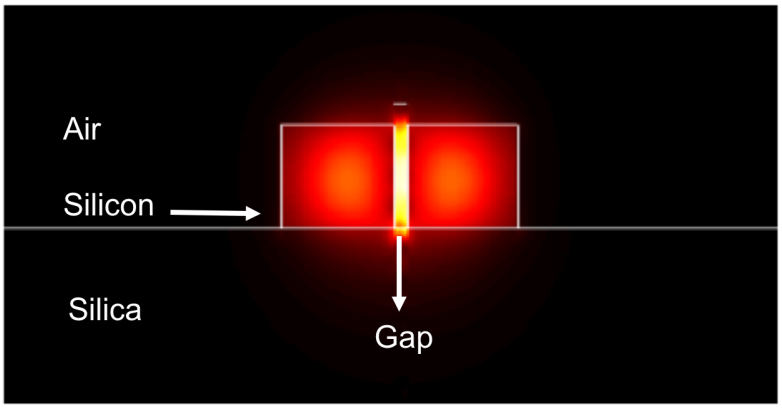

Figure 2.11: Simulated mode profile in a slot SOI waveguide at $\lambda = 3.8$ μm [47].

Since silica has high absorption in the MIR range, ideally, removing the silica can reduce the propagation loss. However, etching errors of the middle gap and the roughness of the side wall contribute to high loss. Shallow etching or a wider waveguide design can reduce the propagation loss, but they will reduce the interaction of light with the analyte as well. These elements need to be considered for sensing applications, the propagation loss and light interaction should be balanced.

Ge-on-Si waveguides

A Ge-on-Si rib waveguide (see figure 2.12) was designed for a single mode operation at 3.8 μm wavelength with a low propagation loss of only 0.6 dB/cm. The dimensions of this waveguide were: height = 2.9 μm, width = 2.7 μm and etch depth = 1.7 μm [42]. The main reason for low loss operation of this rib waveguide is that the mode is well confined in Ge and consequently there is less interaction between the mode and threading dislocations at the Ge-Si interface, which act as scattering centres. Also, there is less interaction with the side wall roughness. The fabrication again involved e-beam lithography and ICP etching.

Recently, the improvement of strip waveguides was presented, the Ge-on-SOI platform was chosen to be the platform with 0.85 μm thick Ge, with a width of 6 μm, at a wavelength of 3.682 μm. The propagation loss was about 10 dB/cm [48]. Compared to the Ge-on-Si rib waveguide at 3.8 μm, the propagation loss of these Ge-on-SOI strip waveguides are larger due to larger mode interaction with the side walls.

Summary of Group IV waveguides operating at short MIR wavelengths

A summary of the waveguides discussed in this section are shown in table 2.2.

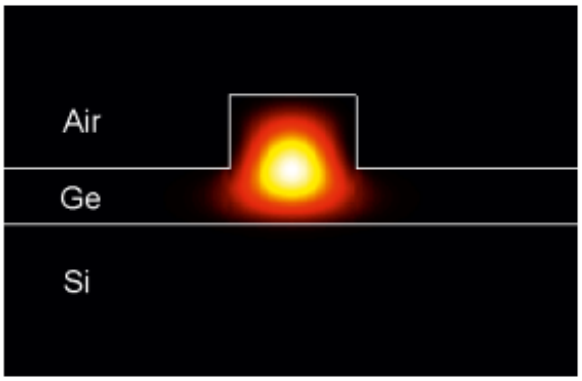

Figure 2.12: Simulated TE mode profile in the Ge-on-Si waveguide at $\lambda = 3.8$ μm [42].

Waveguide	Propagation loss (dB/cm)	Operating wavelength	Width of waveguide	Etch depth	Thickness of waveguide	Reference
Rib SOI waveguides	1.46±0.2	3.77 µm	1.35 µm	220 nm	400 nm	[43]
Strip SOI waveguides	1.28±0.65	3.77 µm	1.3 µm	500 nm	500 nm	[44]
Slot SOI waveguides	1.4±0.2	3.8 µm	Width of 1300 nm/ 78 nm (gap)	500 nm	500 nm	[45]
Rib Ge-on-Si waveguides	0.6	3.8 µm	2.7 µm	1.7 µm	2.9 µm	[42]
Strip Ge-on-SOI waveguides	10	3.682 µm	6 µm	0.85 µm	0.85 µm	[48]

Table 2.2: Summary of group IV waveguides operating at short wavelengths.

2.2.1.2 Group IV waveguides for longer wavelengths

For long MIR wavelengths there are two group IV platforms to choose from: Ge-on-Si and suspended Si [49]. This section will introduce 2 μm thick and 3 μm thick Ge-on-Si waveguides, 11 μm thick Ge-rich graded SiGe waveguide, and 1.4 μm thick suspended Si with sub-wavelength grating claddings for operation at wavelengths >4 μm.

2000 nm Ge-on-Si waveguide at 5.8 μm

The first Ge-on-Si waveguides were reported by Herzig's group from EPFL. These were strip Ge-on-Si waveguides optimized for TM polarisation at a wavelength of 5.8 μm. The propagation loss was 2.5 dB/cm [50]. As figure 2.13 shows, this strip waveguide consists of three main parts: coupling taper (500 μm long), funnelling part (350 μm long) and a straight section. The dimensions of this waveguide were: thickness 2 *um* and width 2.9 μm [50].

After this design, a group in Glasgow presented a Ge-on-Si waveguides at 5.8 μm, with the loss at about 2 dB/cm [51].

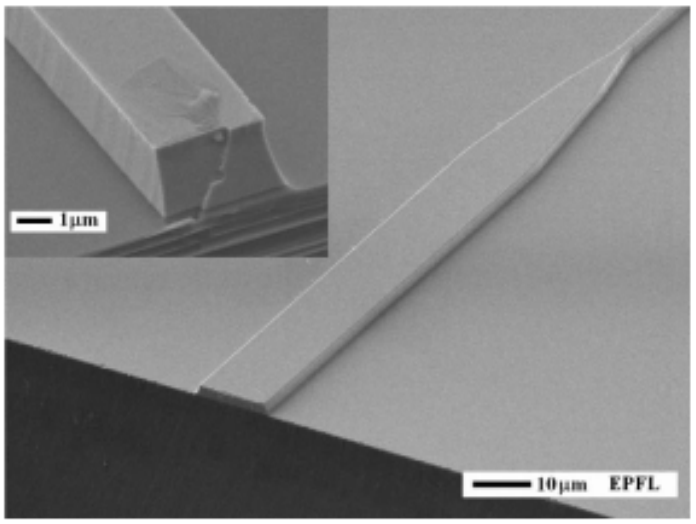

Figure 2.13: Scanning Electron Microscope (SEM) image of a strip GOS waveguide operating at $\lambda = 5.8$ μm [50].

Ge-on-Si rib waveguides at wavelengths up to 8.5 μm

Ge-on-Si (GOS) waveguides were also characterised at a wavelength range of 7.5-8.5 μm, the minimum propagation loss of the GOS waveguide was 2.5 dB/cm at 7.575 um [52]. The dimensions of this waveguide were: 3 μm thick Ge layer, 4.3 μm width, 1.5 μm etch depth. The process of fabrication was the same as previously for the 3 μm GOS waveguide operating at 3.8 μm, but required a dicing (lapping and polishing) process, because the input was butt-coupled and the output was grating coupled. Figure 2.14 shows the diced waveguide cross-section. Compared to the 3 μm GOS waveguide at 3.8 μm, this rib was wider, which can be expected since the mode size scales with wavelength. With the increasing of the wavelength, a larger mode is produced, which needs a larger core [52].

Ge-rich graded SiGe rib waveguides at wavelengths up to 11 μm

A graded SiGe platform operating at a higher wavelength range which is between 5 μm to 11 μm is demonstrated in [53]. Figure 2.15 shows the schematic of such a waveguide, with a width of the graded SiGe rib waveguide being 6.2 μm, and the etching height H being 6.1 μm which includes a 2 μm thick $Si_{0.2}Ge_{0.8}$ layer.

As figure 2.16 shows, at this wavelength range, below 8 μm the loss is less than 1.2 dB/cm; between a wavelength range of 9.5 to 11.2 μm, the loss is below 3 dB/cm; the loss is slightly high when the wavelength is between 8 to 9.5 μm but is still less 4.6 dB/cm. In the wavelength range of 5.1-8μm, the loss mainly comes from the roughness of the sidewall of the rib waveguide and free carrier absorption of residual dopants. Between 8.1 - 11μm wavelength range, the loss occurs due to absorption from the silicon substrate, sidewall roughness, and free carrier absorption of residual dopants. However,

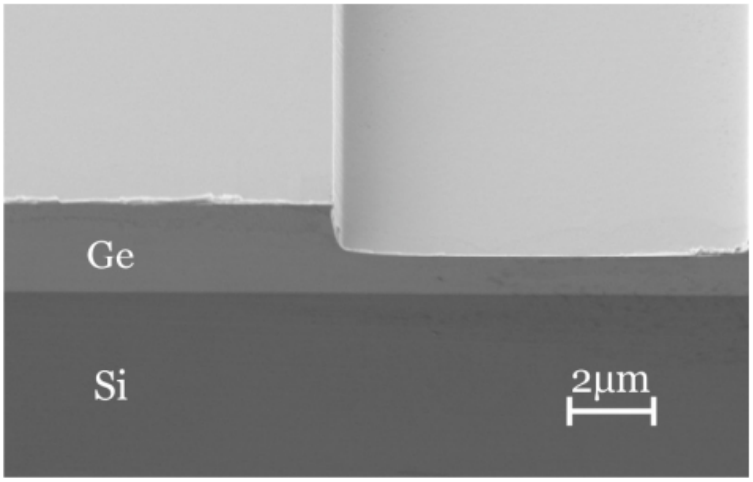

Figure 2.14: SEM image of a 3 μm rib GOS waveguide cross-section after dicing [52].

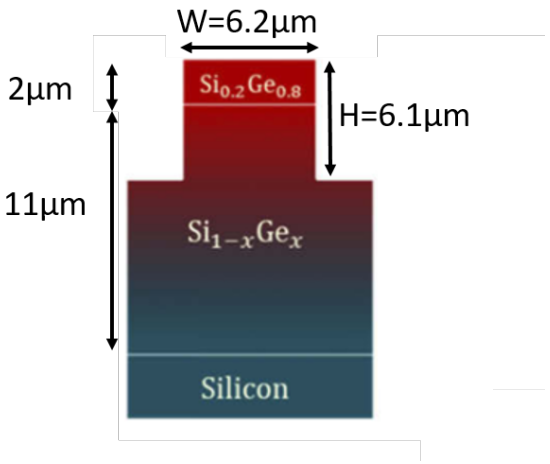

Figure 2.15: Rich-Ge graded rib waveguide's dimensions with 6.1 μm etch depth and 6.2 μm width, this waveguide operates at a 5 μm to 11 μm wavelength range [53].

the loss between 9.1-9.3 μm is predominantly because of the absorption of O_2. During the deposition of rich Ge graded SiGe layer on substrate Si platform, the deposition process includes O_2 gas resulting in Si-O-Si bonds being created during the deposition process, which absorbs light.

This waveguide is able to operate at a longer wavelength range which is up to 11 μm with low loss. This means that the device will be good for sensing more analytes which have absorption peaks at longer wavelengths. However, this design requires one complicated deposition process for the $Si_{0.2}Ge_{0.8}$ layer [54].

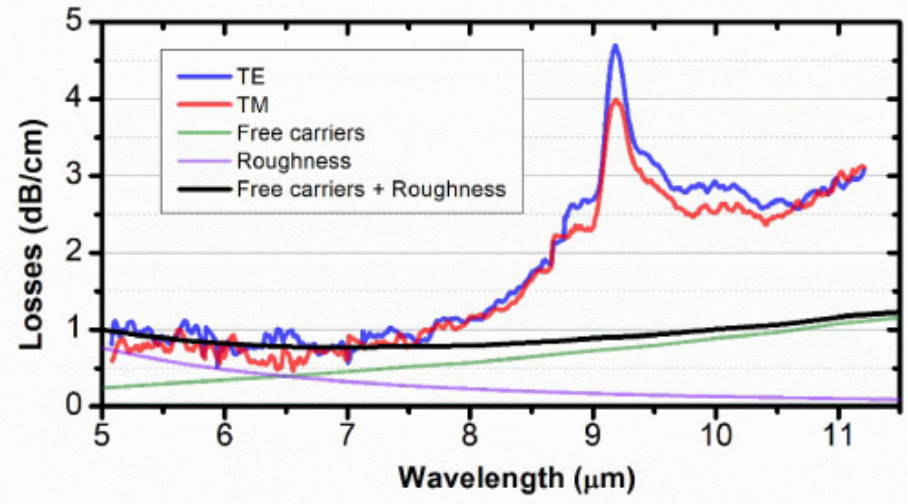

Figure 2.16: The propagation loss of a graded SiGe waveguide, the green line shows the loss of free carrier absorption, the violet line shows the loss due to roughness of the sidewalls, and the total loss of these factors are plotted with a black line. The propagation loss from TM and TE are seen as the red and blue curve [53].

Suspended Si waveguide with a sub-wavelength grating cladding operating at 7600 nm

Another option at longer wavelengths is to use suspended waveguides to remove the high loss of silica. A suspended Si waveguide with a sub-wavelength grating cladding was realised from the SOI platform by opening holes in the top Si layer, and subsequently removing the silica layer. As figure 2.17 shows, the grating period (Λ) in top view is smaller than the wavelength, such that there is no scattering of light propagating in the waveguide core. Such waveguides have been recently demonstrated with a propagation loss of 3.1±0.3 dB/cm at 7.67 μm wavelength. The dimensions of the suspended waveguide were (see figure 2.17): width of core $W_{core} = 2.9$ μm, cladding width $W_{clad} = 3$ μm which limits the leakage to the lateral silicon region, silicon thickness $t_{Si} = 1.4$ μm, buried oxide layer thickness $t_{BOX} = 3$ μm, $L_{hole} = 900$ nm, $L_{Si} = 250$ nm [55].

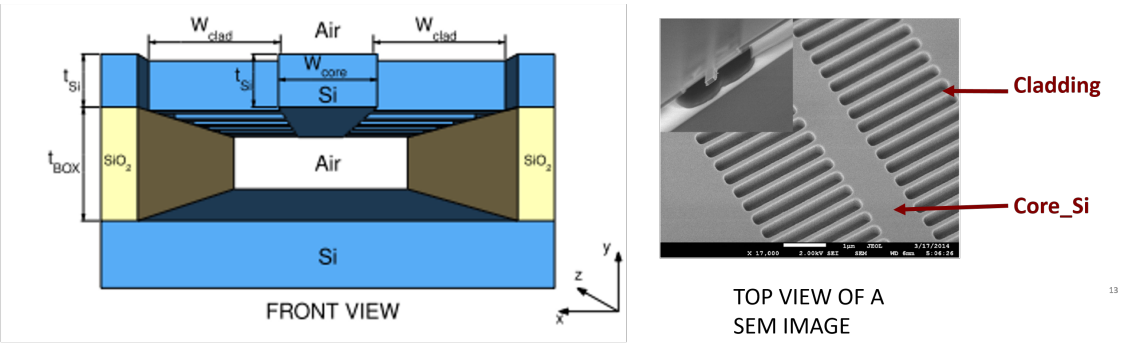

Figure 2.17: Suspended Si waveguide with sub-wavelength grating cladding (front and top view) [55].

Compared to the GOS platform, it is also able to achieve higher sensitivity in the detection of analytes, because the Ge-on-Si waveguide air interface has a higher index contrast (Ge/air) than the suspended Si waveguides (Si/air), which results in Ge-on-Si waveguides having smaller mode overlap with an analyte [55]. The suspended waveguide can offer two side evanescent fields, thus increasing the mode overlap with an sample. However, suspended SOI waveguides need two etching steps, which are the opening of holes on the top Si layer and removing the silica underneath as seen in figure 2.17. This means it has a more complex fabrication process.

Summary of Group IV waveguides for longer wavelengths

A summary of the waveguides discussed in this section are shown in table 2.3.

Waveguide	Propagation loss (dB/cm)	Operating wavelength	Width of waveguide	Etch depth	Thickness of waveguide	Reference
Strip Ge-on-Si waveguides	2.5	5.8 µm	2.9 µm	2 µm	2 µm	[50]
Rib Ge-on-Si waveguides	2.5	7.575 µm	4.3 µm	1.5 µm	3 µm	[52]
Ge-rich graded SiGe rib waveguides	< 1.2	< 8 µm	6.2 µm	6.1 µm	13 µm	[53]
	< 4.6	8-9.5 µm	6.2 µm	6.1 µm	13 µm	[53]
	< 3	9.5-11.2 µm	6.2 µm	6.1 µm	13 µm	[53]
Suspended Si waveguide	3.1 ± 0.3	7.67 µm	See figure 2.17	See figure 2.17	1.4 µm	[55]

Table 2.3: Summary of group IV waveguides operating at longer wavelengths.

2.3 Mid-Infrared silicon-on-insulator thermo-optic waveguide switch for sensing

With the technological advancements of SOI waveguides and integrated optics, different types of SOI thermo-optic waveguide switches have been produced. Based on MIR silicon photonics materials, SOI and SiO_2 platforms will be discussed, as they are a key component to the work completed in this thesis. Furthermore, a background on Multi-Mode Interference (MMI) and Mach-Zehnder (MZI) switches will be introduced. Some typical performance metrics for the MZI and MMI optical switches will also be described.

The principle working mechanisms of a thermo-optic waveguide switch centres on the ability of a waveguide to guide light and the use of a heater to change the effective index of the platform. This then leads to a change in the phase of the light, through a process known as the thermo-optic effect [56]. The thermo-optic effect refers to the change of the real part of the refractive index with temperature, with the rate of change being named the thermo-optic coefficient ($\frac{dn}{dT}$) [57].

Taking silicon as an example, the phase change of the light $\triangle \varphi$ is relative to the change of Si refractive index $\triangle n$ by the thermo-optic effect as shown in equation 2.3, where λ is the wavelength, and L is the length of the heated area [58].

$$\triangle \varphi = \frac{2\pi \triangle nL}{\lambda} \tag{2.3}$$

If the phase change $\triangle \varphi$ of light is π, ie destructive interference occurs, then the change of temperature $\triangle T$ can be found by equation 2.4:

$$\triangle T = (\frac{dn}{dT})^{-1} \frac{\lambda}{2L} \tag{2.4}$$

2.3.1 Thermo-optic analysis of silicon and silica in the MIR region

Silicon and SiO_2 (silica) have been already successful demonstrated experimentally as suitable photonic materials for integrated photonic circuits [59][60]. Silicon is a good choice as a waveguide material.

SiO_2 has a stable and low thermo-optic coefficient. As figure 2.18 shows, at 23.5°C, the thermo-optic coefficient $(\frac{dn}{dT})$ of SiO_2 is 0.5× 10^{-5} C^{-1} , 0.3× 10^{-5} C^{-1} and close to zero at a wavelength of 2.73 μm, 3.05 μm, and 3.37 μm respectively [61].

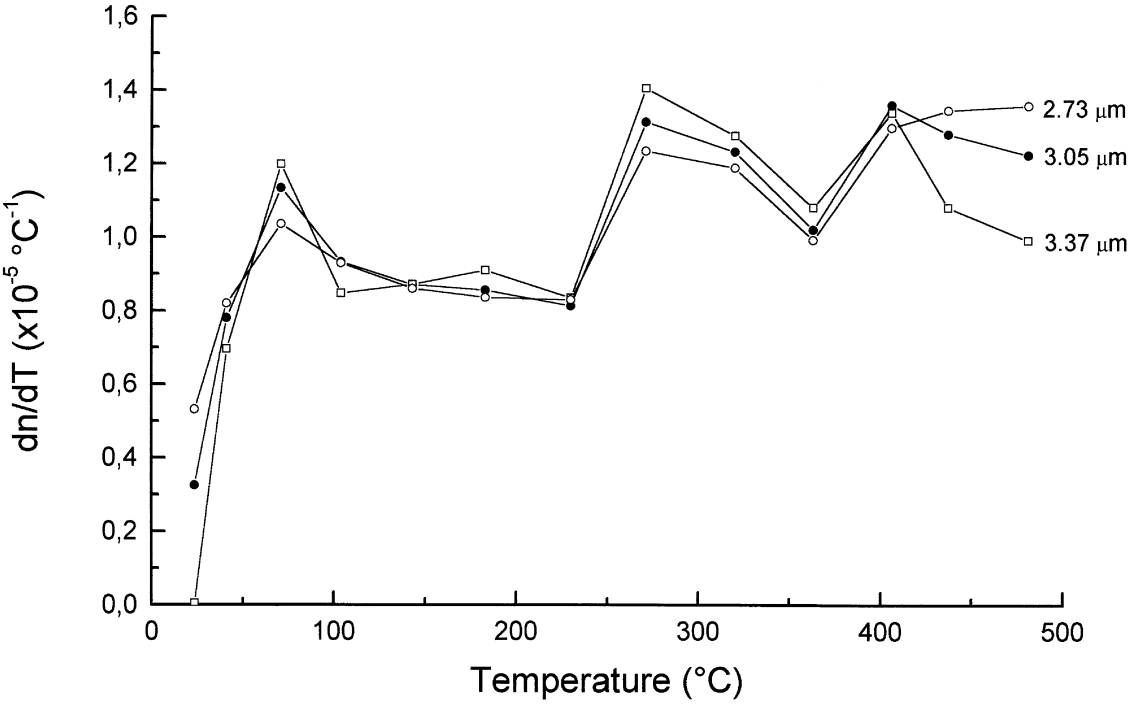

Figure 2.18: Spectrum of the silica thermo-optic coefficient (dn/dT) for the 0 - 500 °C temperature range at varying wavelengths in the MIR region [61].

Compared to SiO_2, silicon undergoes a larger thermo-optic effect and the coefficient which is 1.7 $\times$ 10^{-4} C^{-1} at a wavelength around 3 μm (see figure 2.19). The thermo-optic coefficient of Si is much bigger than SiO_2 at 26.85 °C (300 °K), which means Si is a more efficient material for thermo-optic modulation at a wavelength around 3 μm. This is because the refractive index of Si can be changed by small change of temperature which means for the switch to function only a low input power is needed [43].

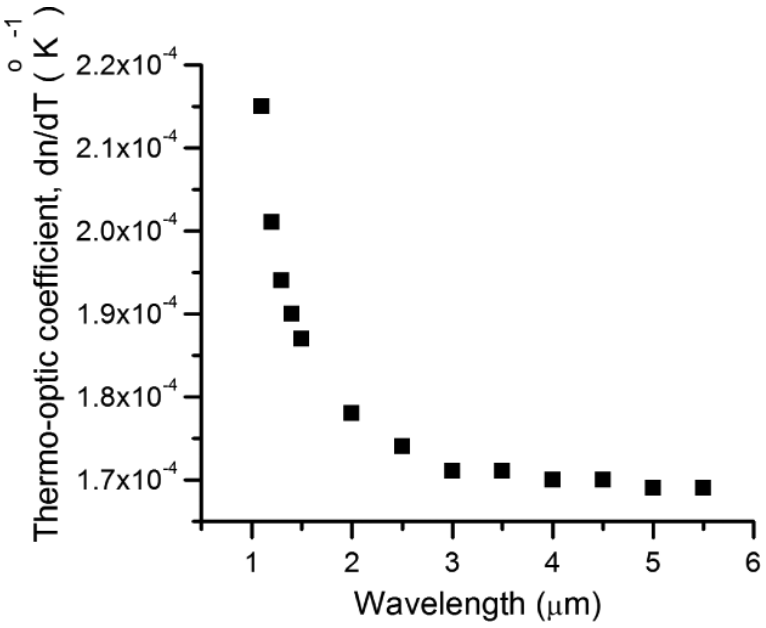

Figure 2.19: Spectrum of the silicon thermo-optic coefficient (dn/dT) at 300 °K for varying wavelengths [43].

2.3.2 Multi-mode interferometers and Mach-Zehnder interferometers for thermo-optic switches.

Mach-Zehnder Interferometers (MZI) and Multi-mode Interference (MMI) devices are regularly used for optical switches. In optical switch circuits, MMIs are usually used as a power coupler or splitter. Figure 2.20 shows one 1×2 MMI as a power splitter (figure 2.20(a)) and a 2×1 MMI as a power coupler (figure 2.20(b)). For the 1×2 MMI structure, there normally is an input waveguide which is supporting the single mode. Then a taper will help guide the light to a multimode waveguide. In the multimode waveguide, the light will be excited to multimode states. After that, two tapers are able to guide two single modes to output waveguides separately. This design can be used as a splitter in a switch circuit. In the 2×1 MMI structure, compared 1×2 MMI, there are two input waveguides and one output waveguide. This design can be used as a power coupler in a switch circuit.

When the light goes from a single mode input waveguide to a multimode waveguide, higher order modes can be excited (see figure 2.21). Figure 2.21 shows 9 guided modes

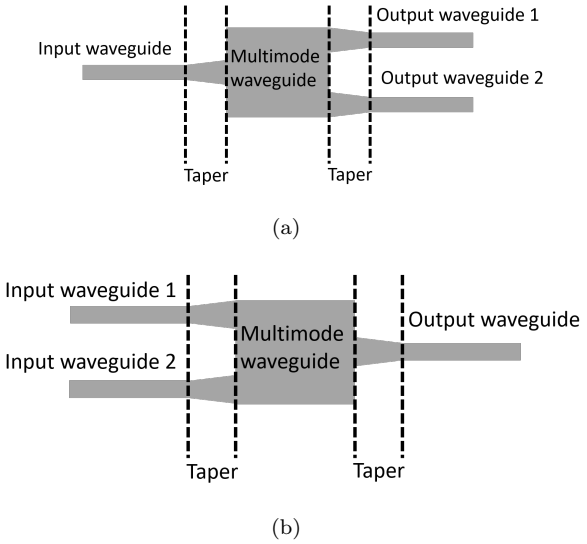

Figure 2.20: (a) The schematic of 1×2 MMI structure and (b) 2×1 MMI structure.

(υ is the number of the mode and W_M multimode waveguide width). These modes have different group velocities because they have different propagation constants β. They interfere with each other while travelling in the same waveguide. If the interference pattern happens to be periodic, as in figure 2.22, it is called self-imaging. The interference pattern is related to beat length (L_π) which is the length at which there is a π phase difference between the fundamental and first higher order modes of the waveguide.

$$L_\pi = \frac{\pi}{\beta_0 - \beta_1} \tag{2.5}$$

where β_0 is the first mode's propagation constant, and the β_1 is the propagation constant of the second mode.

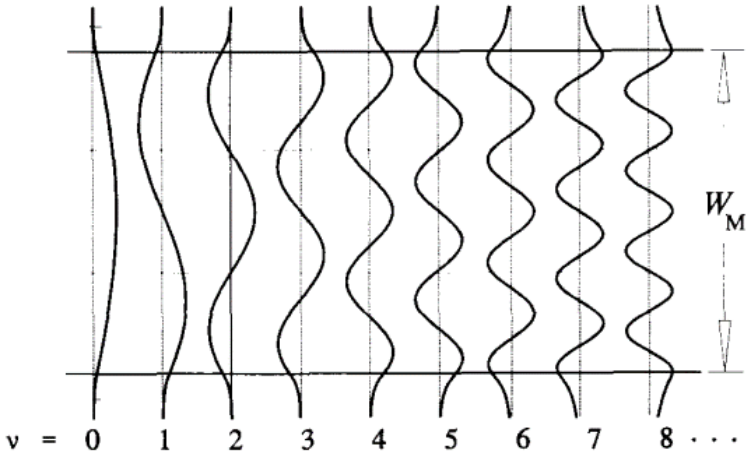

Figure 2.21: Multimoded waveguide with W_M width supports 9 modes and their field profiles are displayed [62].

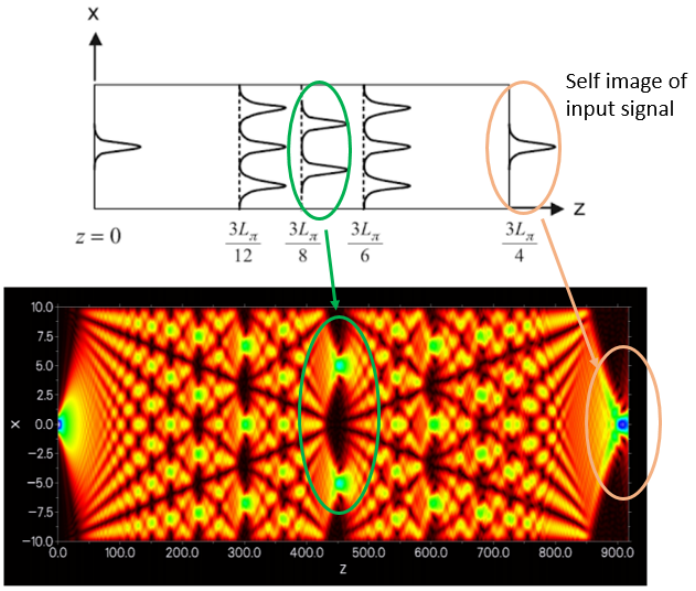

Figure 2.22: An intensity map of power for symmetric interference against length [63][64].

The yellow circle in figure 2.22 is the self-imaging point of the input signal, and is found to be at $3L_\pi/4$. For a 1×2 MMI as a power splitter, the length between the input and two output waveguides should be $3L_\pi/8$ [43], as it is here where we can see that the input light is split into two equal intensities (see the green circle in figure 2.22).

For a 2×2 MMI, there are two input waveguides which are input waveguide 1 and input waveguide 2. Two input tapers guide light from the input single mode region to the multimode waveguide. Two output tapers guide the light from the multimode waveguide into single mode output waveguide 1 and output waveguide 2 (see figure 2.23). When the input optical power is divided into two output ports, there is a 0.5 π phase shift between the two output signals [65].

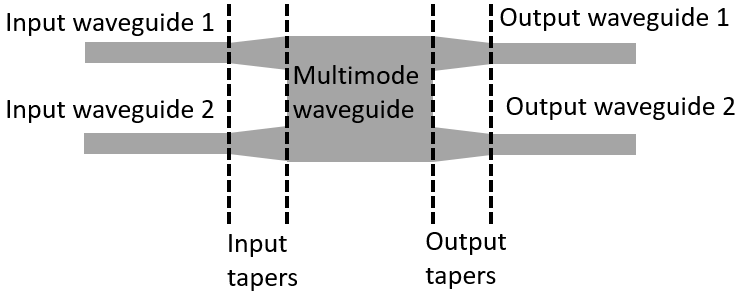

Figure 2.23: The schematic of 2×2 MMI with two input waveguides, two input tapers, a multimode waveguide, two output tapers and two output waveguides.

The MZI-based optical sensor is made by a sequence of separate components. There is a 1×1 Mach-Zehnder Interferometer (MZI) and a 1×2 MZI. The 1×1 MZI contains one

input and one output, to which the working mechanism is shown in figure 2.24(a). A 1×2 MZI contains one input (1×1 MMI) and two outputs (2×2 MMI), which can be used as a switch. It can switch the light beam between two output ports by changing the phase of the light and then combine the light to cause interference in a 2×2 MMI, like figure 2.25.

The 1×1 Mach-Zehnder Interferometer is a conventional configuration with two phase shift arms, one splitter and one combiner (see figure 2.24(a)) [66]. The splitter is used to split the input light power into two arms, which are known as the upper-waveguide and the lower-waveguide, equally, creating two 'paths' for the light. In the case where the two light paths are equal, one would expect to find a constructive interference pattern when the light recombines at the combiner. This state can be considered to being the open state for the switch. However, when one of these paths is modified, the interference pattern would be expected to change. If the modulation is severe enough to produce a phase change whereby the two light paths are fully out of phase, the interference will be destructive which means the switch can be considered as off. To alter the path length and hence the output signal of an interferometer there are a variety of methods. Two of the simplest methods to do this modification are by varying the length of one of the arms (see figure 2.24(a)) or by the thermo-optic effect (see figure 2.24(b)) [67] being applied to one of the arms. As figure 2.24(a) shows, there are two varying lengths of the arms in the MZI. Figure 2.24(b) shows heaters on both arms that are used to change the waveguide's refractive index. MZIs can transform very minor differences in path length to greater, more readily detectable changes in optical intensity [68].

As figure 2.25 shows, the light is split by a 1×2 MMI. The light beams then travel into two channels. These channels have a thermal phase shifter (heaters) placed on top of each of them. These shifters are used to change the phase of the light in the arm. Then the light beams are recombined which causes interference in the 2×2 MMI. The light will be guided into output 1 or output 2, which depends on the difference of the lights' phase and the subsequent interference pattern in the 2×2 MMI.

There are several performance metrics for the MZI such as insertion loss and extinction ratio (ER).

(1) Insertion loss:
The total loss of the modulator or switch is the insertion loss, which includes the coupling loss of light from the laser to the waveguide, the propagation loss of the waveguide, and the loss of the splitter as well as bends, etc. If the input power is P_{in} and the output power is P_{out}, then the insertion loss in dB can be calculated using equation 2.6.

$$Loss(dB) = 10 * \log_{10} \frac{P_{out}}{P_{in}} \tag{2.6}$$

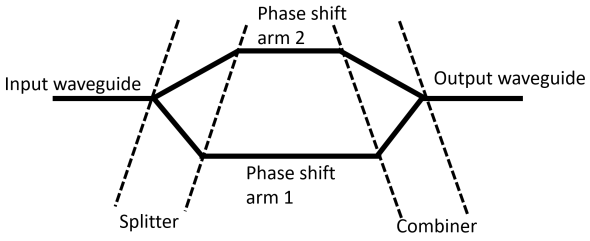

(a)

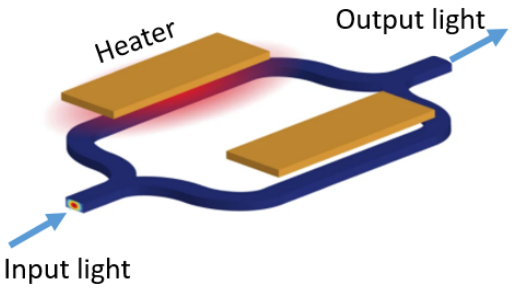

(b)

Figure 2.24: The schematic of Mach-Zehnder Interferometers. (a) Asymmetric MZI structure. (b) thermo-optic Mach-Zehnder Interferometer with heaters on SOI waveguides [67].

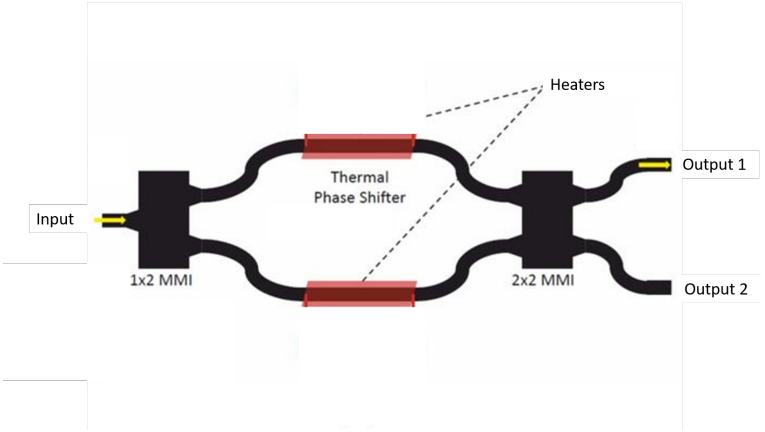

Figure 2.25: The diagram of a 2×2 MZI switch, it has one input which is a 1×2 MMI. This splits into two arms, each with a thermal phase shifter deposited on top of the separate waveguide. These recombine at the output, into a single 2×2 MMI [69].

(2) Extinction ratio (ER):

The extinction ratio of the modulator is defined as:

$$Loss(dB) = 10 * \log_{10} \frac{P_{max}}{P_{min}} \tag{2.7}$$

In the MZI, if the maximum transmission and minimum transmission are presented in dB, then the extinction ratio can be defined as the differences between them. In [70], the authors used silicon spiral waveguides as two arms of the asymmetric MZI. One arm was covered with a metal layer as the heater's contact pad, and the electrical probes were used to contact the heater. The electrical probes are connected with a DC power supply. Figure 2.26 shows the optical transmission versus the DC power of the probes. The maximum transmission is around -0.2 dB and the minimum transmission around -18 dB, therefore, the extinction ratio is 17.8 dB.

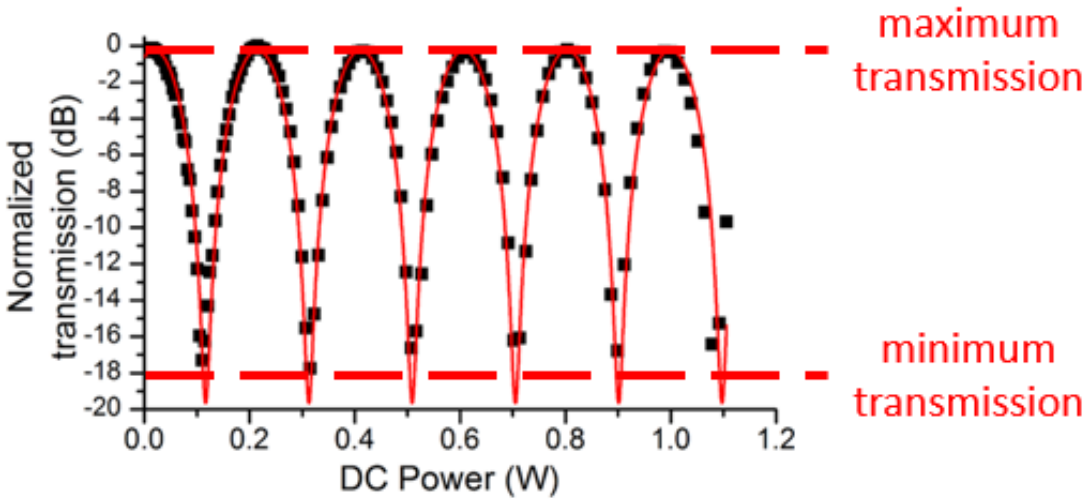

Figure 2.26: The spiral waveguide MZI's normalized transmission in dB of the experimental result (black squares) and the fitted theoretical result (red line). As can be seen, a small change of power to the probes can lead to a large change in transmission [70].

2.3.3 MIR on-chip switch sensor application based on Mach-Zehnder Interferometer

A research work [71] used a plasmonic MZI as a liquid optical bio-sensor which is based on metal-insulator (MI) plasmonic waveguides at the wavelength of 690 nm. This work aims to measure the sensitivity of BSA (bovine serum albumin) sample with SA (serum albumin) as background. The principle of plasmonics is the use of electromagnetic waves to generate coherent charge oscillations on the metal interface. The idea is that more light is guided on the metal surface, which makes the refractive index of the metal surface very sensitive to the accumulation of particles from the surrounding medium [72].

As figure 2.27 shows, in this refractive index sensor design, the authors chose two slits as the input waveguide and the output waveguide, and the middle silver film as the cladding layer of the reference arm to protect the reference arm from the samples. There are three layers on this platform, the upper plasmonic metal layer as the sensing arm

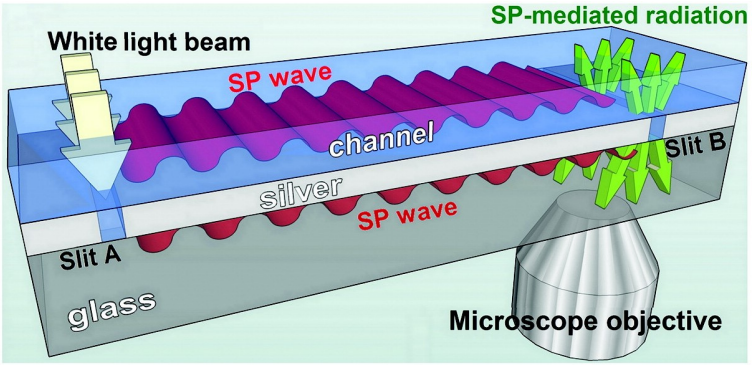

Figure 2.27: Plasmonic MZI sensor with reference channel and sensing channel. The upper metal layer is a sensing channel, and the substrate glass is a reference channel [71].

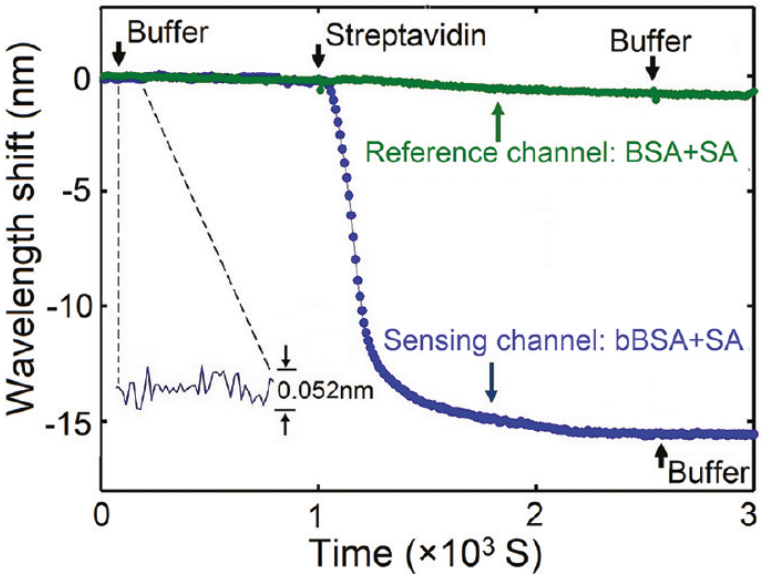

Figure 2.28: Response of the sensor device using plasmonics to generate refractive index changes when in a sample medium. Here we see two distinct traces, one for the reference arm and one for the sensing arm. For different sample media, a wavelength shift is detected, significantly larger than the noise level of 0.052 nm[71].

and the bottom plasmonic metal layer as a reference arm. As figure 2.28 shows, their experimental results proved this plasmonic MZI biosensor could distinguish the bBSA (biotinylated bovine serum albumin) and BSA samples, the analyte bBSA in the sensing arm can generate a 15.7 nm wavelength shift with 0.052 nm of noise.

This design has few components which means less integration loss. However, there is no tuning, which means there is no opportunity to compensate for the fabrication error. A small fabrication error can lead to the light being unequally split between the reference and the sensing channel. This could be solved using thermo-optic tuning.

2.4 Sample Spectrum for MIR

Chemical substances are composed of atoms, which are known to be constantly vibrating. The molecules absorb specific wavelengths which are consistent with the vibrational and rotational frequencies of the molecule. Hence, according to the peak positions and the intensity of absorption, the chemical substance can be qualitatively analysed. In addition, the functional groups could lead to specific absorption spectra of molecules.

An ideal sample in the MIR should fulfil the requirements below:
1. The solute and solvent have no chemical reactions with the chip material.
2. The solute should have strong absorption in the MIR.
3. The selectivity between solute and solvent at the same wavelength range should be high.
4. The solvent is not highly volatile.

Based on the laser sources that are available in the lab, this section will report some absorption spectra of several specific samples at three MIR wavelength ranges. There is one laser which functions in a short wavelength region 2.5 - 3.9 μm and another which works in a longer wavelength region 5.3 - 12.8 μm. For the 2.5 - 3.7 μm region, aspirin and paracetamol can be used as analytes because they have absorption peaks in this wavelength range (figures 2.29 and 2.30). For the 3.725 - 3.880 μm wavelength range, Isopropanol (IPA) has been chosen as the analyte because it has absorption peak at this wavelength range (figure 2.33). Since water is a very important element in our body, and it does not have high absorption in this wavelength range (figure 2.32), water will be used as the host solvent. In reality, sensing devices are less interested in testing for samples within water hosts. Instead, solutions such as blood may be tested for medical diagnostics. However, laboratory sensing devices may use water as a sample for testing, as water and blood have very similar absorption spectrum in the wavelength range of 2 - 14 μm [73].

For longer wavelength region experiments (5.3 - 12.8 μm), acetone [74], and cocaine [75] will be chosen as analytes, because they have high absorption at this wavelength range, and carbon tetrachloride as a solvent as it has low absorption [76].

Aspirin
Aspirin is frequently used as a painkiller [77], but if overdosed, can cause a fatal outcome [78]. The spectra appears to have multiple wide peaks notably at around 3.7 μm and 3.85 μm. These are also relatively wide, likely due to interactions between high frequency O-H and low frequency O-O bonds which have been widened [79]. Aspirin's complex shape leads to multiple bands in it's absorption spectra. Formula: $C_9H_8O_4$
Absorption peak: 3.3 - 3.9 μm, solid state (figure 2.29).

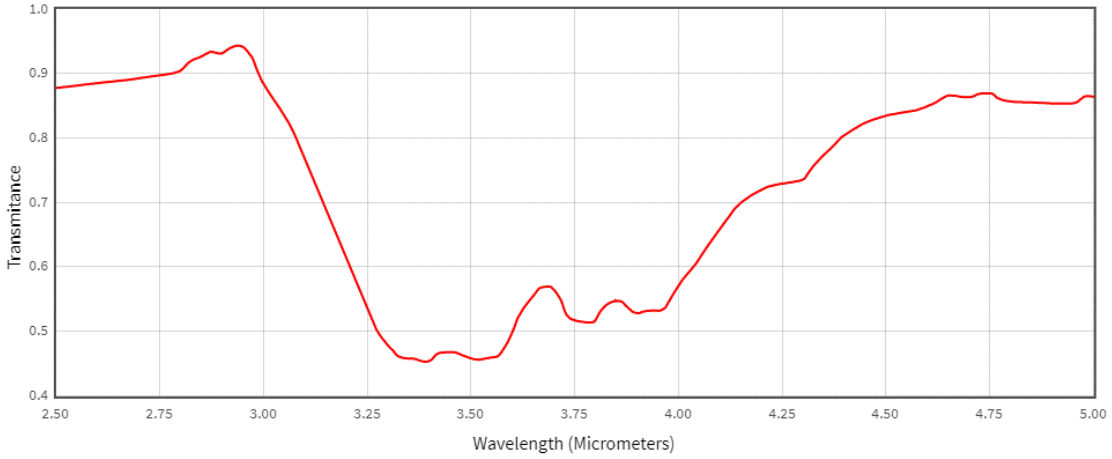

Figure 2.29: Spectrum of a 10 μm solid aspirin sample at the 2.5 - 5 μm wavelength range [76].

Paracetamol

Paracetamol is also a painkiller, sometimes called acetaminophen. Paracetamol is a common drug for self-poisoning, which can cause liver damage and can even cause death [80]. Timely treatment (within 4 hours) is important to prevent liver damage [81]. Typically, diagnosing paracetamol drug level is based on laboratory blood analysis, which requires at least 30 minutes. That means rapid detection of the level of paracetamol in blood is important as it can can reduce the risk of liver damage, and enables treatment to be timely provided to a patient.

Formula: $C_8H_9NO_2$

Absorption peak: around 3.25 μm, solid state (figure 2.30).

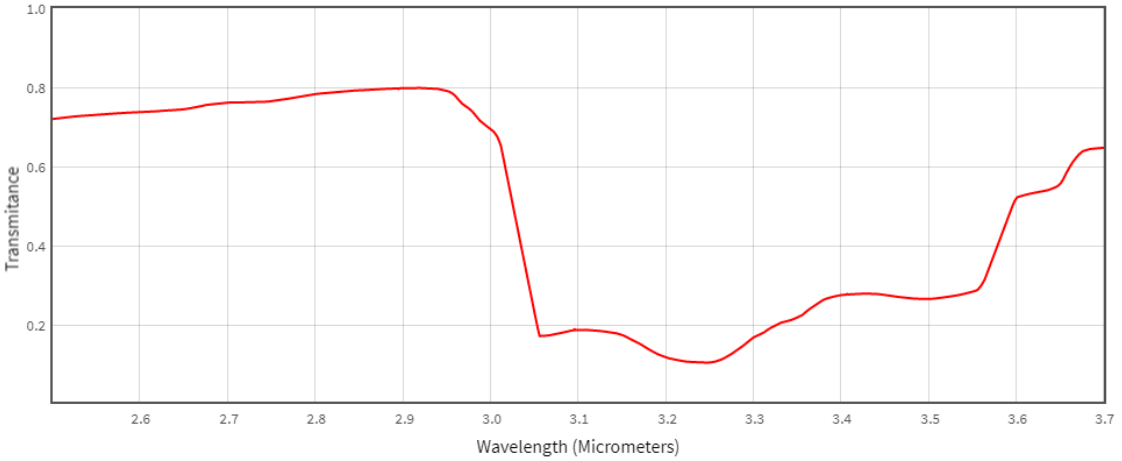

Figure 2.30: Paracetamol (solid state) spectrum between 3 to 5 μm wavelength range [76].

Water

Water is the most important element in our body (70 - 75% in weight). It is also an

abundant solvent and transport medium in biochemical reactions [82]. As the NIST [76] standard database shows, the spectrum of water between 3.725 to 3.888 μm wavelength is almost flat (figure 2.32), whilst there is an absorption peak at 2.7 - 3.5 μm (figure 2.31).
Formula: H_2O

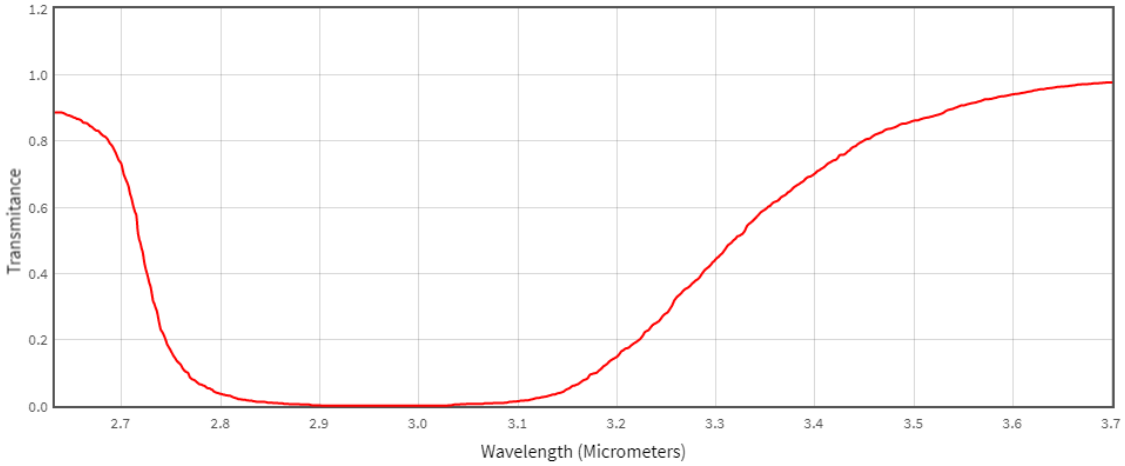

Figure 2.31: Pure water spectrum between 2.5 to 3.7 μm [76].

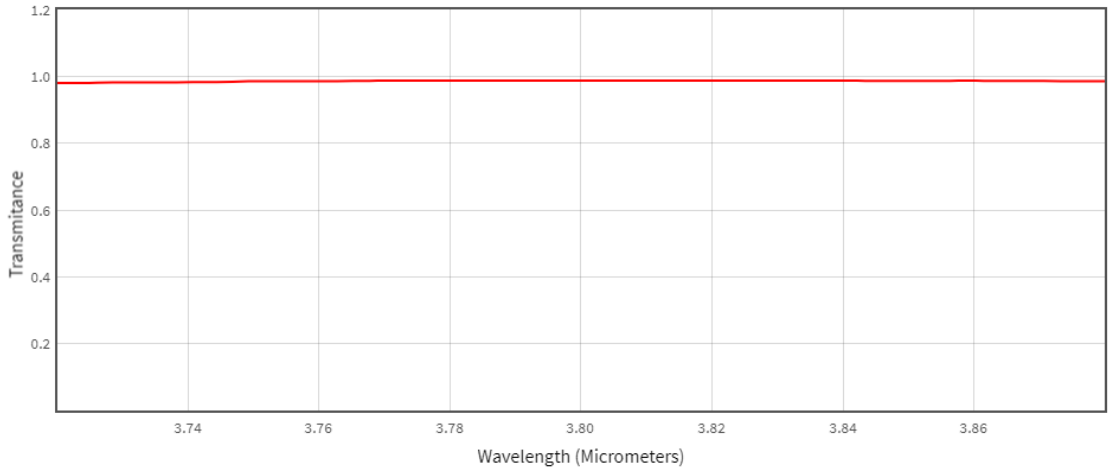

Figure 2.32: Pure water spectrum between 3.725 to 3.888 μm [76].

Isopropanol

Isopropanol (IPA) is a colourless alcohol liquid. It dissolves in water but it is highly volatile. Usually, it is used in pharmaceutics, plastics, paint, and cosmetics.
Formula: C_3H_8O
Absorption peak: around 3.77 μm (figure 2.33).

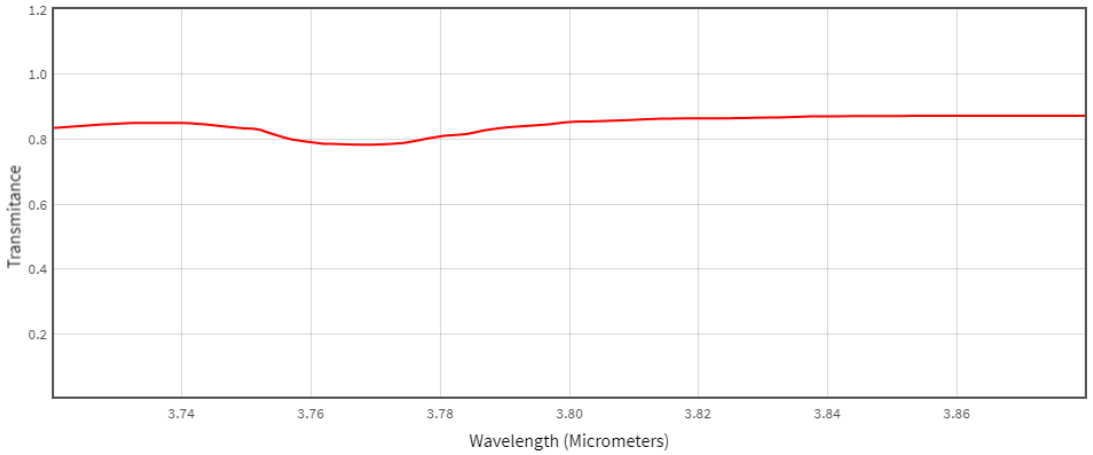

Figure 2.33: Pure IPA spectrum on 0.01 *cm* path length between 3.725 to 3.880 μm wavelength [76].

2.5 Summary

This chapter reports features of different techniques for MIR absorption spectroscopy sensing, waveguide platforms, thermo-optic waveguide switch sensors and target samples.

For short MIR wavelengths, GOS and SOI platforms are described. Compared to the GOS platform, the SOI platform is more mature in terms of fabrication. In addition, SOI waveguides can be easily covered with SiO_2 which is usually used for bonding with a microfluidic channel. Also, the GOS platform is a relatively new platform and there are not well known recipes for covering Ge with suitable claddings.

For the SOI platform, 500 nm slot SOI waveguides, 500 nm strip SOI waveguides and 400 nm rib SOI waveguides have already been demonstrated. Compared with the 500 nm slot SOI waveguide, the strip waveguides have lower propagation loss as discussed in section 2.2.1. Therefore, for short wavelengths, the 500 nm strip SOI waveguide will be used for sensing systems.

For longer wavelength ranges in the MIR, 1.4 μm suspended Si waveguides with sub-wavelength gratings, 3 μm GOS and 2 μm GOS platforms have been described. Considering the fabrication process, the 1.4 μm suspended Si waveguide is more mature than the GOS waveguides. However, the former has higher propagation loss than the latter at a wavelength of $\sim$ 7.6 μm and requires more design effort for liquid sensing scenarios. The GOS platform has lower propagation loss than the suspended SOI platform, but needs a protection layer and deposition of a bonding layer for the integration with microfluidic channels. Potential analytes include acetone, or cocaine, and carbon tetrachloride as the solvent.

Chapter 3

Silicon waveguides integrated with microfluidics for IPA sensor

In this chapter, the experimental work of the silicon waveguides integrated with microfluidics for mid-infrared evanescent absorption spectroscopy will be presented in 4 sections: (1) simulation and fabrication processes for low loss waveguides; (2) controlling the interaction length with mask design; (3) fabrication processes for the PDMS microfluidics channel; (4) addressing the repeatability of the measurements and avoiding the evaporation of the sample using a microfluidics system.

The sensing device used in these works include two key aspects - a microfluidics part and an optical part (see figure 3.1). The microfluidics part includes a syringe pump (1 ml) which is used to pump the sample into and out of the microfluidics channel. The optical part includes a tunable QCL source, input/output fibres, a detector and a waveguide. The microfluidics part was bonded onto the waveguide and will be described in chapter 3.5. This system operates at the 3.725 μm to 3.888 μm wavelength range.

For this wavelength region, considering the requirement for low loss waveguides, we have based our work on previously demonstrated SOI waveguides with a low loss of 1.3 $\pm$ 0.7 dB/cm at 3.8 μm [44]. The SOI platform was chosen because it uses only standard fabrication processes, and a library of well-optimized passive components is already available for the 3-4 μm wavelength range. Because silicon-on-insulator (SOI) technology can be accessed at low cost through multi-project wafer services in which near-infrared and MIR devices can be made on the same wafer, SOI technology is an attractive prospect.

The samples under analysis are mixtures of IPA as the analyte and water as the solvent, because in the 3.725 μm to 3.888 μm wavelength range, IPA has a signature absorption peak [76] making it easy to distinguish. Water can mix with IPA and does not react with it, meaning different concentrations will be easy to make and test. In addition, water

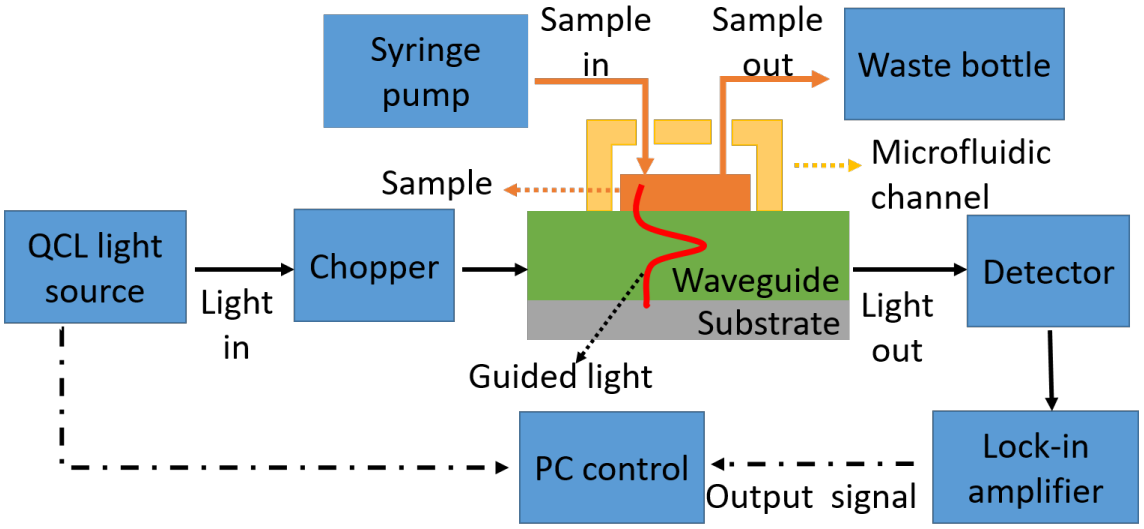

Figure 3.1: The block diagram of the whole system for sensing.

is an important molecule and has very similar absorption spectrum in the wavelength range of 2-14 μm [73] with blood, meaning that testing absorption of aqueous solutions could be useful outside of the lab.

The preliminary demonstration of the device was carried out by sensing different concentrations of water-IPA solutions at wavelengths between 3.725 μm and 3.888 μm. The aims of these measurements was to use absorption spectra to differentiate between IPA and water, and also to detect the concentrations of different mixtures of IPA in water. This work used microfluidics in integrated SOI waveguide sensors in this wavelength range to improve the repeatability of sample handling, reduce reagent volumes and prevent evaporation of volatile species.

3.1 SOI rib waveguide's design and simulation

A 500 nm thick SOI rib waveguide was designed for IPA sensing with single mode operation at 3.8 μm. The performance of the waveguide is determined by the dimensions of the SOI rib waveguide. If the waveguides is too wide, the light will begin to propagate in multiple modes, and the aim for our device is to be as wide as possible as this should help to reduce scattering loss from modal interaction with the side walls, while maintaining single mode propagation. The dimensions of the waveguide was simulated by Lumerical MODE solutions software. Lumerical MODE solutions software is able to show a 3D structure of the waveguide and calculate the supported TE mode in a waveguide with a 2D cross-section mesh of the waveguide by solving Maxwell's equations.

The buried oxide (silica layer) thickness of the SOI platform was 3 μm, labelled as Silica BOX in figure 3.2 (a). As figure 3.2 (a) shows a cross-section of the SOI rib waveguide

design, at 3.8 μm wavelength, where h is the thickness of the slab, H is rib height, and by using simulations the rib width was designed to be 1.3 μm. Figure 3.2 (b) shows the simulated result that the light is confined in the waveguide with TE mode, which means the waveguide can guide the light with low loss of 0.47 dB/cm at a wavelength of 3.8 μm. A light wave can be considered as having two types of polarisation. These are known as TE (transverse electric) and TM (transverse magnetic). When considering their electric field vector components, a TM wave will have it's vector pointing in the incidence plane, whereas a TE wave will have it's vector pointing normal to the incidence plane. Any width larger than 1.3 μm produced multi-mode propagation.

The rib can be fully etched by 500 nm in order to increase lateral mode confinement so that the waveguides can have a small bending radius. However, considering that in the subsequent step SiO_2 will be deposited as a cladding, which will then be fully etched to create sensing windows of varying lengths along the waveguide, a thin un-etched slab is needed to act as an etch stop layer, the partially etched rib design ensures that the silica BOX layer is not affected by the HF etching of the cladding, as the 50 nm thick Si layer protects the BOX. Therefore the rib waveguide is etched 450 nm Si to leave a 50 nm thick Si slab layer.

In order to control the interaction length between the waveguide and the analyte, a 2 μm thick SiO_2 top cladding was deposited onto the sample, which was simulated in Lumerical MODE Solutions and confirmed that a 2 μm cladding was thick enough to completely isolate the waveguide mode from an analyte. Holes are then patterned into the SiO_2 to create sensing windows of varying lengths which will be described in the next section.

Lumerical is also used to simulate the percentage of light in air and the TE mode profile at a wavelength of 3.8 μm. The simulations showed 10.6% of the light is evanescent, which means this light can be used to interact with the analyte for sensing measurements. In sensing applications based on the evanescent field, the balance of the evanescent field fraction and the propagation loss should be considered. As the evanescent field fraction increases, the light has more interaction with the analyte and the sensitivity of the device will be higher. However, a device with a large evanescent field will intrinsically have a large loss. Therefore the device needs to be tailored to ensure that this loss is not too high, but still maintains a high evanescent field so that interaction with a sample can be observed. The overall output of the device also needs to be larger than the noise floor of the detector after travelling through the waveguide. This will allow the detector to be able to receive a strong signal from the output light. We can compare the output light and input light to calculate the absorption of the analyte. In this case, 10.6% of the light is the value we picked up to understand the relationship between evanescent field fraction, propagation loss of waveguide and sensitivity of analyte. This percentage is not the optimal value of such an experiment, as translating the device to real world applications raises too many issues such as device size and light interaction

with the sample, however the chosen percentage is a good compromise due to the issues surrounding loss and evanescent field strength.

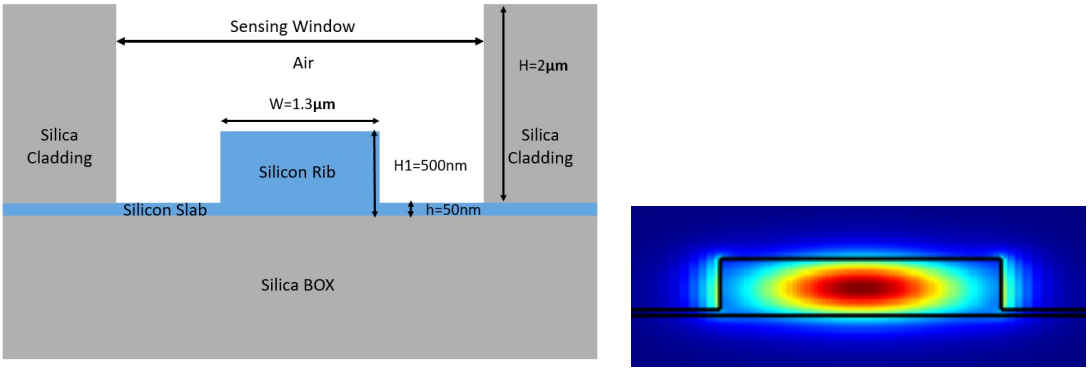

(a) (b)

Figure 3.2: The design of SOI rib waveguide. a) 2D schematic of the SOI rib waveguide cross-section with W_{rib}=1.3 μm, H_{rib}=500 nm, h_{slab}=50 nm, with a silica cladding layer and an etched sensing window. b) Simulated TE mode profile at λ=3.8 μm.

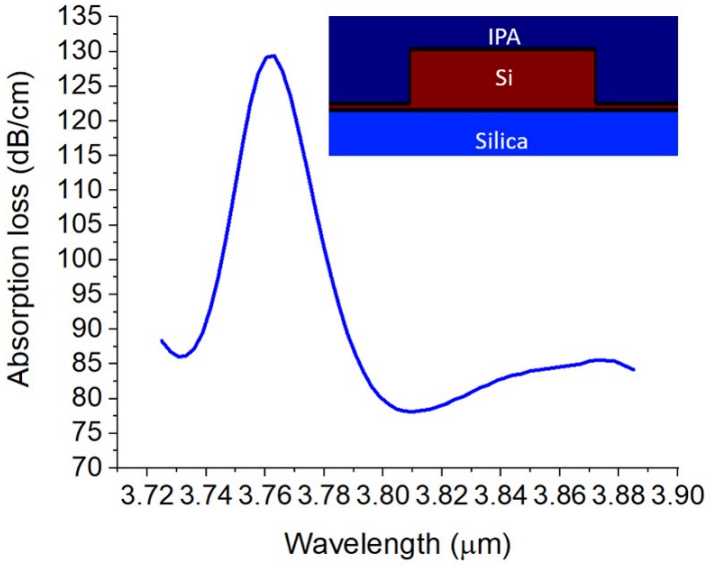

Figure 3.3: Modelled absorption spectrum of the SOI waveguide covered with IPA between 3.725 μm and 3.888 μm, using literature data for IPA absorption and refractive index [83].

3.2 Simulation of the IPA spectrum on a SOI rib waveguide

Lumerical MODE Simulations was used to simulate the absorption loss spectrum of a SOI waveguide with a top cladding of pure IPA as well. In this simulation, using the

wavelength-dependent refractive index, n, and extinction coefficient, k, of IPA [83], as well as the same parameters for Si and SiO_2, the model was constructed with a semi-infinite region of IPA above the waveguide. The absorption loss was simulated over a wavelength range from 3.725 μm to 3.888 μm . The result (see figure 3.3) for TE polarization shows the absorption spectrum of pure IPA near 3.77 μm, with a peak waveguide absorption of ∼130 dB/cm. This simulated spectrum of IPA on the SOI rib waveguide can be used to compare the experimental spectrum of IPA in the measurements section later.

3.3 Mask design of the chip

From the result of the simulation, to begin to make the waveguide a reality, focus turned to the mask design of the chip. The Beer-Lambert law [84] states that the absorption of a sample depends on the interaction length. Different interaction lengths were defined by etching windows in the cladding layer to test the sensitivity of the device to water-IPA solutions as an exemplar biochemical mixture. In this case, 10 μm to 3 mm interaction lengths were designed, which were chosen based on a preliminary measurement that was carried out using SOI waveguides and the same 3.8 μm wavelength setup with pure IPA as the sample (see Appendix). This also allowed the chip to be used for measurements of different concentrations, and different analytes, which might have different absorption strengths, without the need for further fabrication.

This mask was designed with both grating couplers and edge couplers. This is because there were two experimental setups. The first set up can operate at the wavelength range of 2.5 - 3.7 μm and had a tunable laser as it's source. Due to this wide wavelength range, to couple into the chip devices, butt-coupling was used, as it would allow for a wide range of wavelengths to be coupled into the device. Butt-coupling works via free space optics focussing the beam into the waveguide on the chip. This setup can be used to detect aspirin and paracetamol, because these analytes have absorption peaks between 2.5 and 3.7 μm. The second setup required a grating coupler to couple light into waveguides as the laser was directed into an optical fibre alignment. Grating couplers function by arrays of materials of a refractive index accept incident light to be coupled to the device as the incident light is at resonance to the grating design. This allows for filtering of non-resonant light. This setup guided light in the wavelength region of 3.7 - 3.9 μm. The grating coupled waveguides can be used to detect IPA at the 3.7 - 3.9 μm wavelength range, as IPA has absorption peaks in this wavelength range. The grating coupler design from [44] was used in this work.

Figure 3.4 shows the designed mask of the chip with both grating coupler waveguides and butt-coupling waveguides. They are drawn in the red colour and with purple shading in

the open sensing area. The blue section is the microfluidics channel position with input and output holes (which will be introduced in section 3.5).

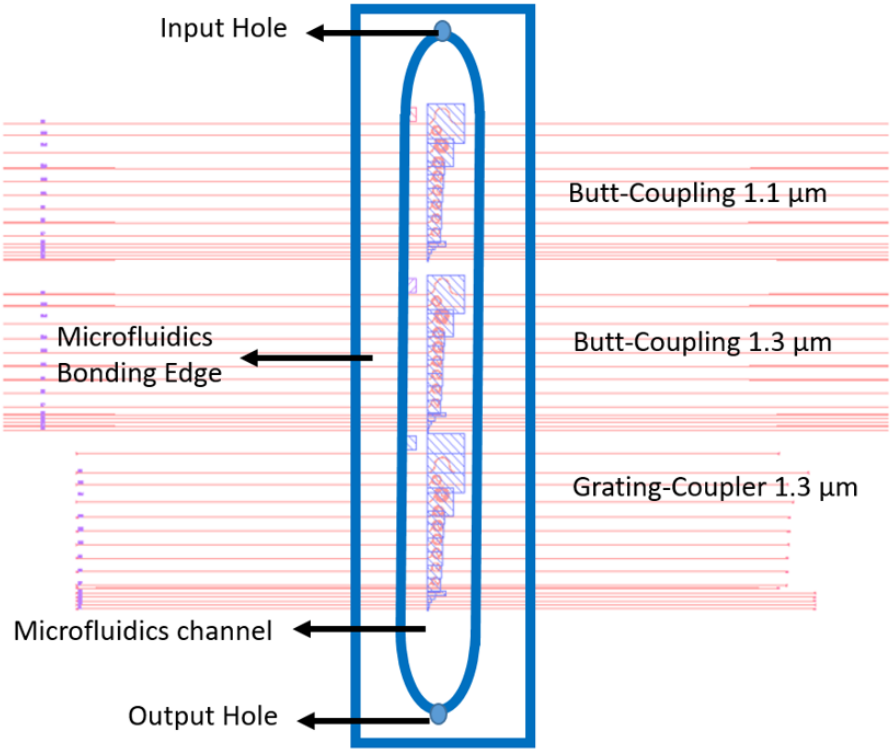

Figure 3.4: Mask design with SOI waveguides with grating coupler section (red colour), SOI waveguides butt-coupling section(red colour), microfluidics section and sensing section (purple shading).

Figure 3.5 (a) shows the block diagram of the grating coupler waveguides and figure 3.5 (b) shows the design of the grating coupler waveguides with a microfluidics channel. It can be seen that the design is symmetrical, with two grating couplers (GC), two 0.5 mm long tapers (Taper), two 9 mm long access waveguides (Access WG), of 1.3 μm width, and the middle part is a 1mm long sensing window (SW) with silica (red colour).

For the GC (see figure 3.6), the widths are 20 μm (W1) and 40 μm (W2), and the length (L) is 60 μm. The width is dependent on the input and output fibre mode field diameter, and the length L is found by the grating coupler design [44]. After the input grating, the input taper was designed, which is used to adiabatically transform the mode from the wide waveguide at the grating coupler to the single mode waveguide. The width of the input side of the taper is 20 μm, while the output side has the same width as the access waveguides (1.3 μm). The length of the taper is 500 μm. There are two main waveguide parts: two access waveguide regions (Access WG) and a sensing window region (SW). There are three main sections for each access waveguide, which are WG1 (3 mm long waveguide 1), WG2 (5 mm long waveguide 2) and WG3 (1 mm long waveguide 3). WG1 is used to guide light from the taper to WG2, the 5 mm WG2 space is used as bonding edge for a microfluidics channel, and the 1 mm WG3 is used as an error margin when

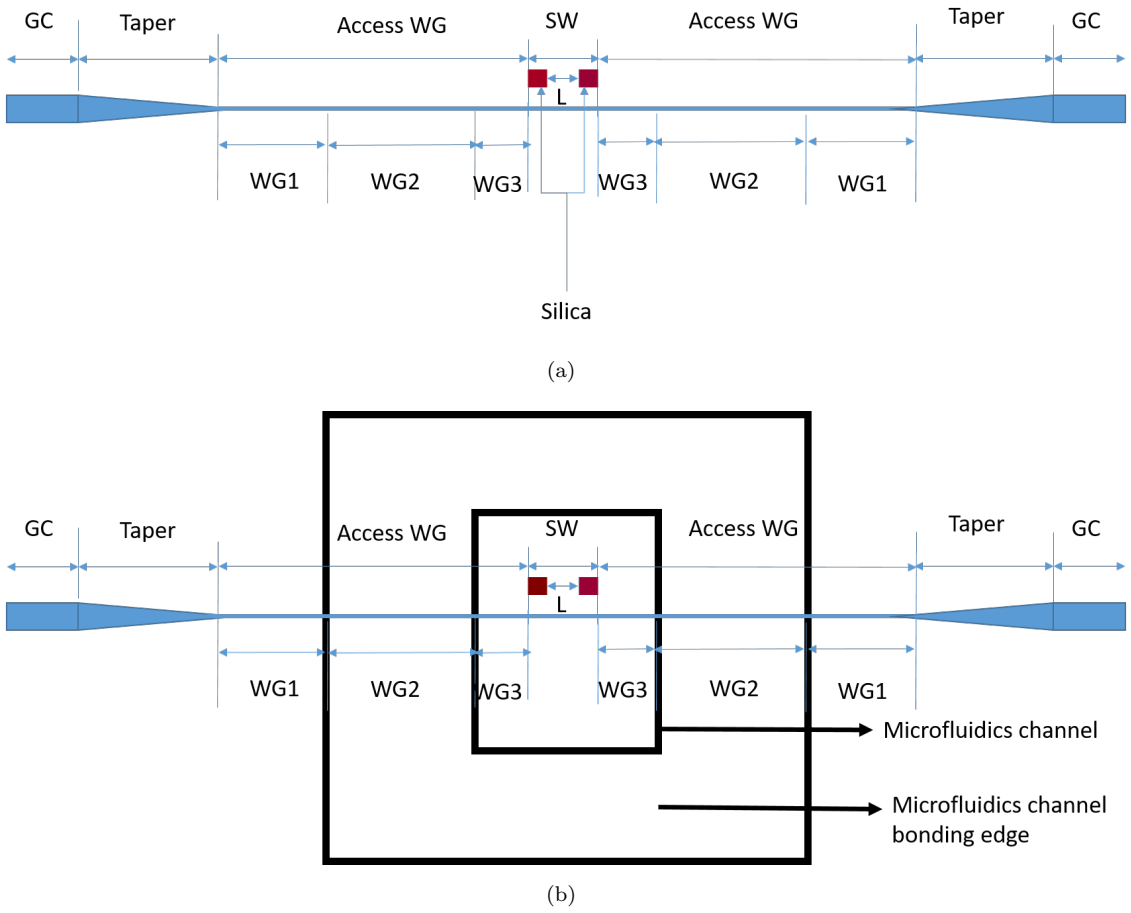

Figure 3.5: Block diagram of the grating couplers for the waveguide design with a microfluidics channel operating at 3.725-3.888 μm. (a) Diagram of the grating waveguide design L_{WG1}= 3 mm, L_{WG2}= 5 mm, L_{WG3}= 1 mm, L_{SW}= 1 mm, L_{Taper}= 0.5 mm. (b) Block diagram of the microfluidics channel block $L_{Microfludics-channel}$= 3 mm, $L_{Microfludics-channel-bonding-edge}$= 5 mm.

bonding. Based on previous experience in our group, the 5 mm bonding edge is needed to make a strong bond between the Si chip and microfluidics. The 1 mm SW is used as the sensing area that will be covered by the microfluidics channel. The 1 mm error margin is needed when bonding by hand because it is difficult to align precisely. Therefore, the microfluidics channel should be 3 mm long (including the two error ranges and the sensing window)(see figure 3.5 (b)).

A butt-coupling waveguide in this mask is used to bring light from the input fibre into the start waveguide (Start WG) via an input taper. The butt-coupling waveguide structure design is similar to the grating waveguide design, and it includes start and end waveguides (End WG), input and output tapers, access waveguides (Access WG) and a sensing window (SW). The width of the tapers was 10 μm and the length was 500 μm. For the start WG and end WG, the width was 10 μm and the length was 3 mm. The width depends on the input and output fibre width, and the length depends on the chip

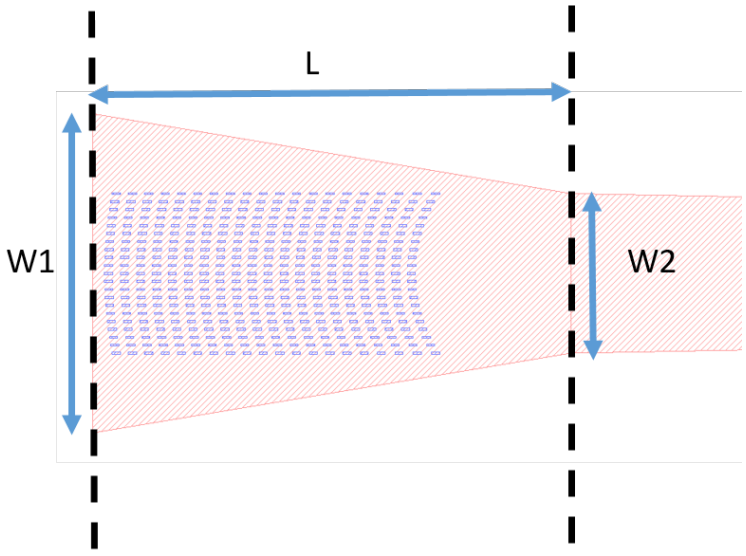

Figure 3.6: Mask design with SOI grating coupler (red colour) design from [44], with length L, width W1 and width W2.

width and should enable lapping and polishing of the chip. The access WG and SW are the same as in the grating waveguide design.

For the butt-coupling section design (figure 3.7), there are two waveguide widths which are 1.1 μm and 1.3 μm. These two different widths are chosen as it is intended that the waveguides will work at different wavelength, and hence be used to detect different samples. For the 1.3 μm width waveguides, they will be used at a wavelength of 3.725 - 3.888 μm and are to measure IPA in water. For the 1.1 μm width waveguides, they are to be used for preliminary tests at a wavelength of 3.3 μm to detect aspirin and paracetamol.

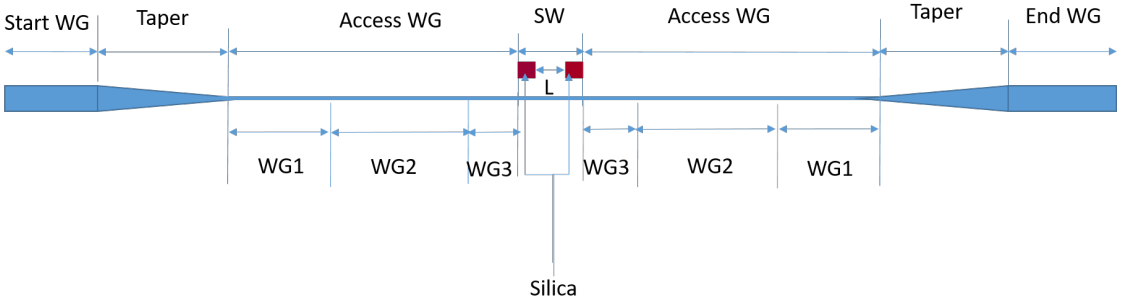

Figure 3.7: Structure of the butt-coupling waveguide design $L_{Start-WG}$= 3 mm, $W_{Start-WG}$= 10 μm, L_{WG1}= 3 mm, L_{WG2}= 5 mm, L_{WG3}= 1 mm, L_{SW}= 1 mm, L_{Taper}= 0.5 mm.

As figure 3.8 shows, in the 1 mm wide sensing window (1mm SW), 10 μm to 500 μm interaction lengths were designed with straight waveguides, as figure 3.8 (a) shows: silica lengths (L (Silica)) is shaded white, and interaction length (L) is shaded purple. For 1.2 mm to 2 cm interaction lengths, spiral waveguides were used. Taking 1400 um and 2

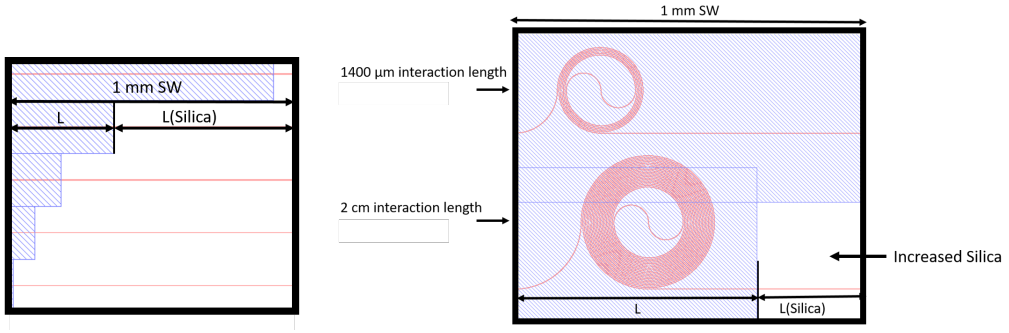

(a) (b)

Figure 3.8: The sensing window (SW) region of the waveguide design in the mask. (a) The straight waveguide design. (b) The spiral waveguide design.

cm interaction lengths as examples (figure 3.8 (b)), a 1400 μm interaction length could fit within the 1 mm sensing widow, whilst 2 cm interaction length could not fit within 1 mm sensing window, and therefore L (Silica) was increased.

3.4 Fabrication

3.4.1 Introduction to the process of chip fabrication

The chip is made by dicing of the wafer. Figure 3.9 shows the electron beam lithography (e-beam) process with an etching step. The wafer was spun with an organic material that is called photoresist, then the mask design is written on to the surface of the wafer by e-beam in this case. The pattern was written point by point, which means that the e-beam needs a long time to write the pattern. However, this is outweighed by the benefits of e-beam lithography as it is able to generate flexible features with no expensive physical mask required, and the features can be made to be below about 10 nm. In this case, the e-beam system used was a JEOL JBX9300FS electron beam lithography system.

For the e-beam resist, there are two types of resists used which are positive resist and negative resist. The type of resist defines what happens after the development step of the photolithography. A developer step is performed after the e-beam pattern, where the patterned wafer is placed in a chemical liquid (ZED-N50) which can remove the e-beam resist. The region that had been a pattern by the electron beam will wash off, except the unpatterned part. This occurs for positive resist. The opposite effect occurs for negative resist.

In this project, ZEP-520A and PMMA (Polymethylmethacrylate) which are positive tone resists are both used. PMMA is used in the large regions of the mask as larger features do not require a high resolution, such as the sensing window. However for high resolution features such as the rib waveguides, ZEP-520A is used. This resist requires

the electron beams to have a high energy, around 80-100 keV [85]. For lower beam voltages, such as 10-30 keV, the resolution will be smaller, as the electron beam has less energy to interact with the resist material.

Compared to ZEP-520A, PMMA has a faster etching rate, which means the etching is less controllable [86]. ZEP-520A has stronger tolerance to dry etching which means can work under higher plasma power, and still maintain a slow etching rate, meaning a shallower etches can be performed without the risk of overetching. However, it costs approximate 25x more than PMMA [85].

In figure 3.9, the resist is positive. After the developer step, the wafer is ready to be etched. In the etching step, the wafer with the resist part will not be etched, and the part without resist will be etched.

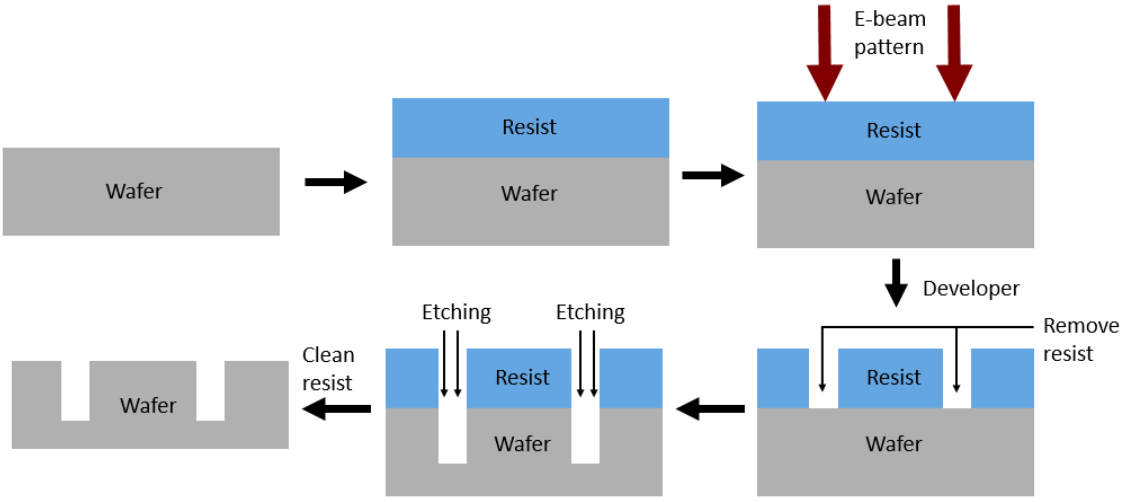

Figure 3.9: Electron beam lithography process with an etching step.

ICP (Inductively Coupled Plasma) etching is a method of dry etching with a plasma. Compared to wet etching, ICP etching produces vertical walls, due to the etching direction being focused vertically down towards the sample by a potential difference between the sample and the plasma (used in section 3.4.2). Figure 3.10 shows the principles of ICP etching. Gases are pumped into an electrical field (blue dotted line) which is created by electrodes in the ICP chamber. Some of the gas will become ionized into a plasma state. The plasma will react with the exposed material, and the reacted product is volatile, meaning it will be evacuated out by the vacuum pump. The etching performance is dependent on the selective gases, gas flow rate, plasma generator (RF) power, stage temperature, ICP power and pressure [87].

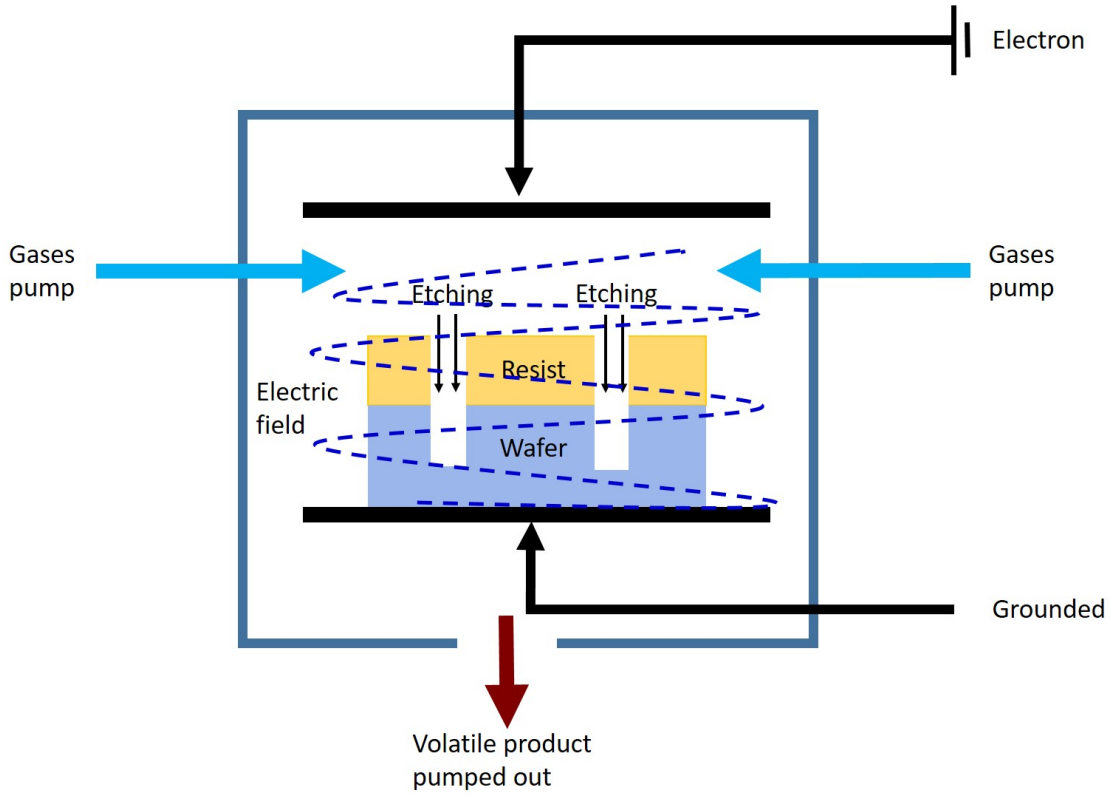

Figure 3.10: ICP etching with etching wafer.

3.4.2 Fabrication of 500 nm SOI waveguides

For this section, the fabrication process will be split into 6 steps, with figure 3.11 (a) used as a reference for these. These steps are mature process steps for photonic devices, and as such many standard procedures were performed. However, the details of the fabrication are discussed:

1. A 500 nm SOI wafer (see figure 3.11 (a)) was put in an oven for 1 hour at 210°C, as a warm wafer is easily coated with the resist. 500 nm thick ZEP-520A photoresist was deposited on the warm wafer surface with a spinner at a speed of 4370 rpm for 180 seconds. It was then baked on a hot plate at 180°C for 3 minutes as advised by the manufacturer, ensuring the resist can stick on the wafer surface properly and the resist is dry. To guide the electron beam on the location of the wafer surface, the photoresist Espacer (ESpacer 300Z) layer is required, because it has a high conductivity. Espacer is used to remove excess charge on the surface of a wafer, which can help ensure good patterning when e-beam lithography is used. The wafer was then patterned using e-beam.

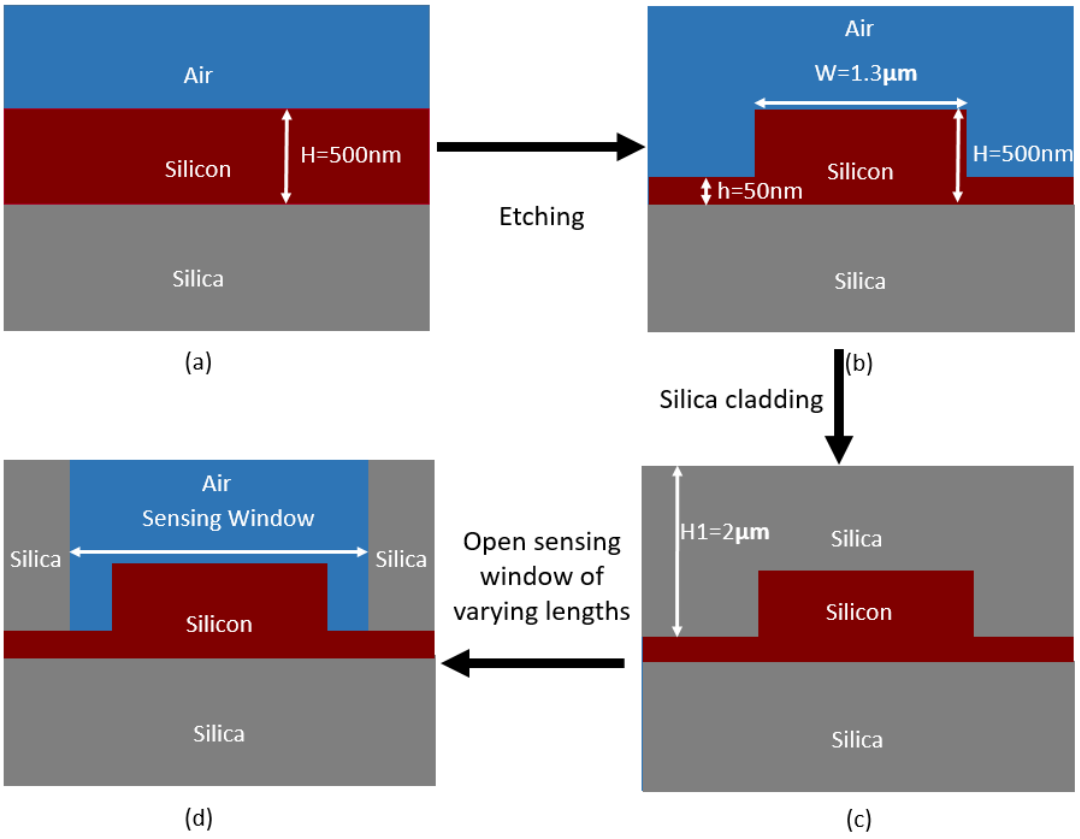

Figure 3.11: The process of fabricating waveguides with sensing windows.

2. A developer step is performed using water to rinse the surface of the wafer to remove the Espacer in a 2-3 minute process to make sure the Espacer is removed. Then the wafer is put in a beaker with ZED-N50 liquid for 2 minutes 15 seconds, whilst shaking the wafer to ensure circulation. Once it was certain that the patterned part of the ZEP had been removed, the wafer was then put in another beaker with IPA, and shaken gently for 30 seconds. Finally, the wafer was dried with a spin rinse dryer tool after the IPA step.

3. The wafer then has 500 nm of Si etched using an Oxford Instruments ICP 380 system. This step is used to etch gratings. The gases used are SF6 and C4F8 with 25 sccm and 45 sccm gas flow rate respectively, the stage temperature was 15°C and the chamber pressure was 15 mTorr. The RF power is 50 W and the ICP power is 800 W. The etching rate is calculated to be 7.5 nm/s. In this fabrication run ellipsometer measurements showed that the etching results were that the Si was etched 468 nm, and the ZEP had a remaining thickness of 384 nm. Then an asher is used to remove the photoresist after the first etch.

4. ZEP and Espacer resists are then spun again, and e-beam patterning is carried out again to pattern the waveguides. The ICP is used to etch 450 nm of Si (figure 3.11

(b)), the process is the same as the grating etching step. The wafer was cleaned using acetone, IPA and DI (deionized) water. After this, the wafer was placed in the asher for 15 minutes to remove the photoresist.

5. The next step was to deposit 2 μm of SiO_2 by PECVD (Plasma Enhanced Chemical Vapor Deposition) (figure 3.11 (c)). To create the sensing windows, the wafer was first put in an oven for 2 hours, then HMDS (hexamethyldisilazane) was deposited on top of the wafer to facilitate PMMA adhesion to the chip. A 2 μm thick layer of PMMA photoresist was then spun on the wafer again, and it was subsequently e-beam patterned. Liquid hydrofluoric acid (HF) was used to remove 2 μm SiO_2 in order to open sensing windows, with 20:1 ratio of water:HF. HF selectively etches SiO_2 but not Si (figure 3.11 (d)). The wafer is then placed in NMP at 50°C for 20 minutes to remove the PMMA, then the wafer was put in the asher for 15 minutes, to make sure that any dust or any remaining photoresist were removed from the wafer's surface.

6. Before dicing the wafer into chips, S1813 photoresist was spun onto it to protect the wafer surface. After dicing the wafer, it is quickly rinsed with DI water to remove large debris particles, then it was cleaned using acetone in an ultrasonic bath for 10 minutes and then rinsed first with IPA, then with DI water, and finally dried with a nitrogen gun.

Table 3.1 shows the summary of the most critical steps in the fabrication process.

Challenge	Solutions
Ensuring ICP etching does not overetch	Calculating the total etching time needed based on experience of the Si etching rate, then perform 3 separate short etches. After every etch step, use of the ellipsometer to measure the thickness of etched Si.
Ensuring HF etching does not overetch	A low concentration of HF was used, HF:water = 1:20, which leads to a slow etching rate. This means there is more control on the etching of the silica.
Ensuring the Lithography is not overdeveloped	Use of the manufacturers suggested timing for development and use of gentle shaking when developing. By also using a large beaker for developing, it can be ensured that removing the chips from the developer liquid can be done easily and quickly, which helps keep the timing as accurate as possible.
Ensuring equal thickness of the photoresist on the chip	Resist was spun at a speed of 4370 rpm for 180 seconds. A high spin speed should correlate to good coverage of the chip. After the resist was deposited, the ellipsometer was used to measure the thickness of photoresist at different points of the chip.

Table 3.1: Summary of the most critical steps in the fabrication process.

Figure 3.12 shows an optical microscope image of a part of the fabricated chip with several straight waveguides and a spiral waveguide. The spiral waveguide is used for a longer interaction length while maintaining a small footprint. The interaction lengths of the sensing areas were over-etched by 140 μm, as it is difficult to control the HF etch rate. Therefore, the fabricated interaction lengths were between 150 μm and 2 cm. The

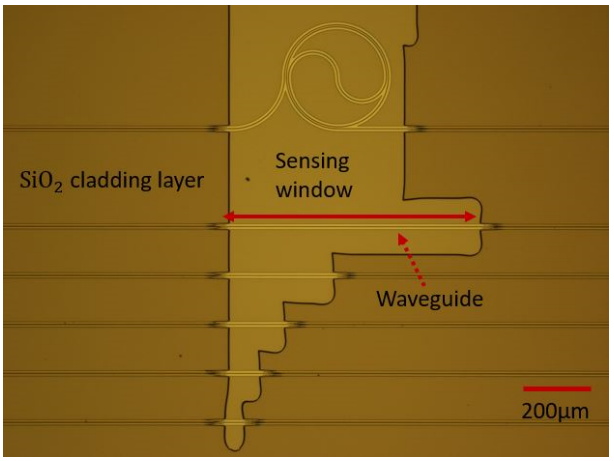

Figure 3.12: Top view microscope image of the sensing window covering different lengths of several waveguides. The darker regions of the image are those covered by the SiO_2 cladding layer, while the lighter areas are the sensing windows.

lighter regions are the open sensing areas, while the darker regions are those covered by the SiO_2 cladding layer. The entire open area is covered by a microfluidic channel which will be introduced in section 3.5: design and fabrication of PDMS microfluidics.

3.5 Design and fabrication of PDMS microfluidics

For on chip MIR absorption sensing, one way to introduce a liquid sample to the waveguide is to place a droplet on the chip surface and to then measure the change of output signal. However, a liquid sample might easily evaporate and therefore the amount of sample is not easily controllable. Instead, a microfluidic channel bonded onto an SOI chip would guide the liquid in a controllable way. The bonding position of the microfluidic channel used here is shown in the previous section (figure 3.4).

PDMS is a widely used material for making microfluidics systems, as it can easily be fabricated and moulded [88]. The microfluidic channel was designed to cover all sensing windows with the sample to be characterized. The microfluidics model was designed with Solidworks software (figure 3.13) and fabricated using the standard procedure described here. Sylgard 184 (a type of PDMS) was chosen as the microfluidic channel material and it was stamped using a 3D printed mould (figure 3.14 (a)). A clean petri dish was prepared to put the PDMS materials which are Sylgard 184 base and agent with 10:1 ratio (Sylgard 184 base : agent) [89]. Once mixed together, the mixture was poured into the mould. The filled mould was put into a vacuum chamber for at least 30 minutes until no bubbles were left in the PDMS. The mould and mixture were then placed into an oven at 150°C for 10 minutes for curing the PDMS. After curing the microfluidics channel, a 1mm Miltex Biopsy punch with plunger was used to make holes through the channel (figure 3.14 (b) (c)), so that tubes can be inserted. A plasma asher was used to

heat the SiO_2 and Sylgard 184 in an O_2 environment to cause covalent bonding between the two surfaces. The result is shown in figure 3.15. The microfluidic channel had a width of 3 mm, a height of 0.5 mm, and a length of 20 mm.

Figure 3.13: 3D model of the microfluidics model, designed with Solidworks.

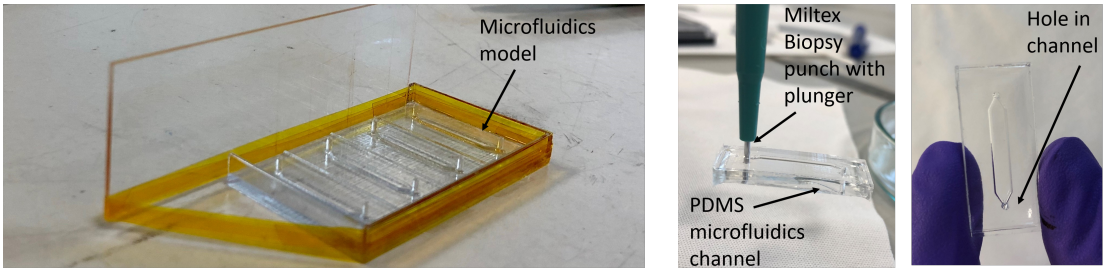

Figure 3.14: Photographs of the microfluidics channel fabrication process: (a) PDMS model made using a 3D printer. (b) PDMS microfluidics channel showing how the Miltex plunger is used to open up the holes to the channel. (c) Completed PDMS channel with the hole to the channel highlighted.

Figure 3.15: An optical microscope image of the PDMS cell bonded onto an SOI chip.

3.6 Experimental setup

In this section the set-up for the measurements using a wavelength of 3.8 μm is described. A diagram of the optical experimental set-up is shown in figure 3.16. It is composed of a MIR tunable laser, a half-wave plate, a chopper wheel (used to cut the beam with a controlled periodicity), a ZnSe lens, MIR fibres, two 3-axis stages, a visible camera, a screen, a MIR detector, a lock-in amplifier, a computer with Labview program to control the laser and save data from the detector, and a chopper controller. In this work, the chip was measured by using optical fibres and surface grating couplers (out of plane coupling). A camera was used as an aid for precise alignment of the fibres and waveguides on the chip. The MIR QCL was tunable from 3.725 to 3.888 μm at 21°C

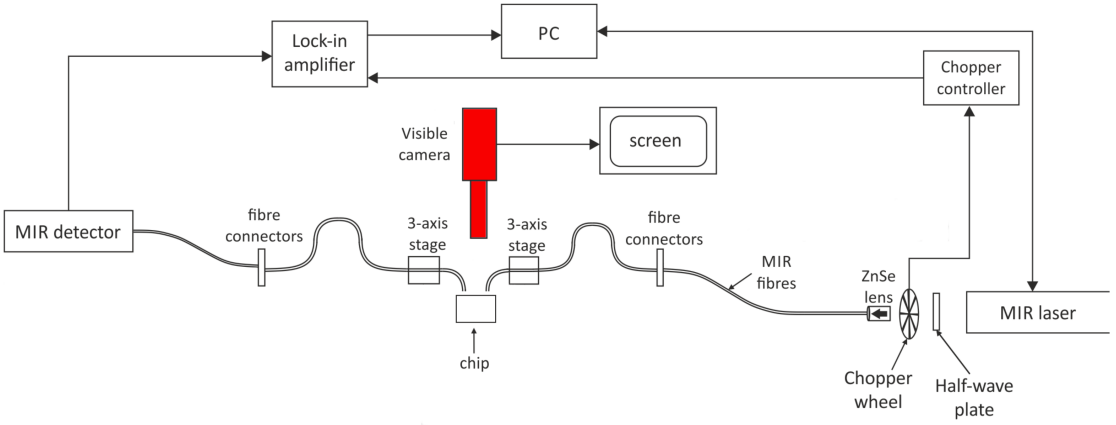

Figure 3.16: A block diagram of the 3.8 μm optical experimental set-up [43].

and has its peak output power of 150 mW at a wavelength of 3.8 μm (see figure 3.17). The laser was connected to a chiller, which keeps the laser at constant temperature. Placed after the path of the the laser is a ZnSe lens which focuses the light into the MIR fibre, to enhance the coupling. For the MIR fibres, in this setup, the fibre is single mode fluoride fibre which guides well in the MIR wavelength range from 3.2 to 5.5 μm. The product name is P3-32F-FC-2 from Thorlabs. This fibre is low loss which is below 0.45 dB/m between 3.2 and 4.6 μm wavelength range [90]. The MIR detector is a IS-1.0 InSb detector (InfraRed Associates Inc). The detector requires liquid nitrogen to keep it at a low temperature, and it has a noise floor around 0.1 mV. It works from 1 to 5.5 μm wavelength range [91]. A lock-in amplifier is also used which is from Signal Recovery, the product name is 7265 Dual Phase DSP Lock-in Amplifier [92]. It is able to achieve a high frequency of about 250 kHz and it allows two different frequencies for two channels. In this work 3.16, the lock-in amplifier was connected to both the MIR detector and the chopper controller. The MIR detector measures the signal of output power from the output fibre, the chopper controller sends the specific frequency to the chopper wheel. This alters the reference signal of the input power from the laser to the lock-in amplifier as well. The lock-in amplifier picks up the signal whose frequency is the same as the

reference signal's frequency and removes the noise, which is based on the orthogonality of sine and cosine waves [93]. In this work, the chopper works at a frequency of 405 Hz as a reference signal. The output from the lock-in amplifier will be collected through a GPIB cable by the Lab-View program in the computer.

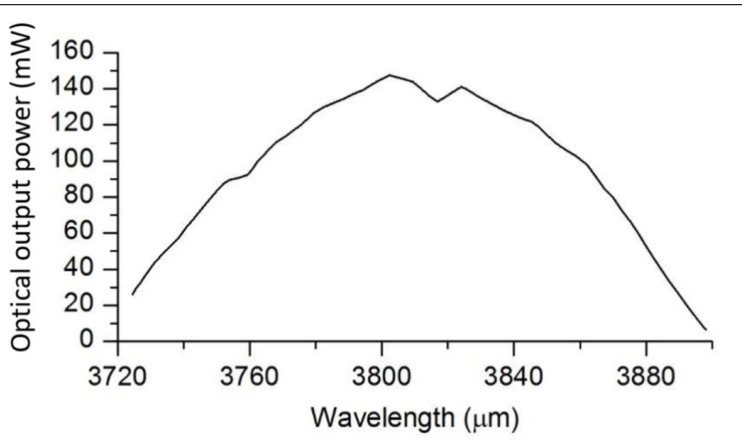

Figure 3.17: The spectrum of the Daylight Solutions QCL laser in the wavelength range of 3.725 - 3.888 μm [94].

Figure 3.18 shows a block diagram of another part of this set-up, which is the fluid delivery system. It is driven by a syringe pump (from KD Scientific) with a 1 ml (volume) syringe (from Nipro) and has an attached input tube. F1-clip tip pipettes can take different percentages of analyte and solvent and mix them in a 1 mm plastic tube. The varying mixture solutions were then put in syringes individually. The syringe pump then pumps the sample through the input tube into the microfluidic channel, which is bonded onto the chip. After passing through the chip, the liquid is pumped out through the output tube to a waste bottle. Between each measurement, the chip is cleaned with water flowed through the channel with a syringe pump, followed by a syringe pump filled with air. This should remove all residue from the chip.

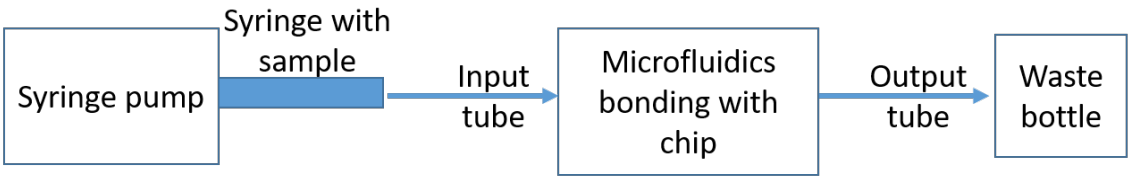

Figure 3.18: Block diagram of the syringe pump experimental set-up.

3.7 Measurements, data analysis, and comparison to theory

3.7.1 Measurements of IPA spectrum and sensitivity of IPA in DI water with SOI waveguides

In this work, mixtures of IPA and water were taken as example analytes to validate the device and microfluidics at MIR wavelengths, because IPA has an absorption peak around 3.725 - 3.888 μm. By using water as a solvent we emulated a more realistic environment which may have smaller or larger water content, even though it also has high absorption at 3.725 - 3.888 μm. In addition, both liquids are easily available, and do not react with the PDMS microfluidics.

As the Beer-Lambert law states the absorption is related to the interaction length (L) and concentration (C) of the sample, therefore, the work began by measuring pure IPA with different interaction lengths of the waveguide.
The aims of these measurements were:
1. To measure the effective interaction length of the waveguide.
2. To test and verify the pure IPA spectrum with different interaction lengths and to measure the absorption peak of pure IPA at 3.77 μm.

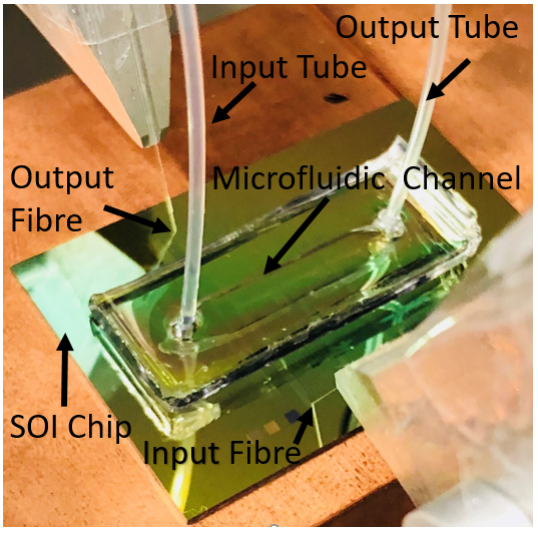

Figure 3.19: Image of the SOI chip with microfluidics and pump tubes.

Figure 3.19 shows the syringe pump system with an input tube connected to the SOI chip (39 mm × 27 mm) with microfluidics channel. The pure IPA solution was pumped into and out of the microfluidics channel with tubes (see figure 3.20). An initial background spectrum was collected by measuring the transmission spectrum of the waveguide when it is only surrounded by air. Firstly, the fibres are aligned to maximise the optical output signal, then the wavelength is scanned from 3.725 μm to 3.888 μm to get the

output signal $P_{background}(\lambda)$. The analyte transmission spectrum ($P_{analyte}(\lambda)$) was then measured with pure IPA being pumped through the channel. This process was repeated for the waveguides of different interaction lengths (150 μm - 640 μm). The absorption (α) in dB was then calculated from the ratio of $P_{analyte}(\lambda)$ and $P_{background}(\lambda)$ for waveguides with different interaction lengths.

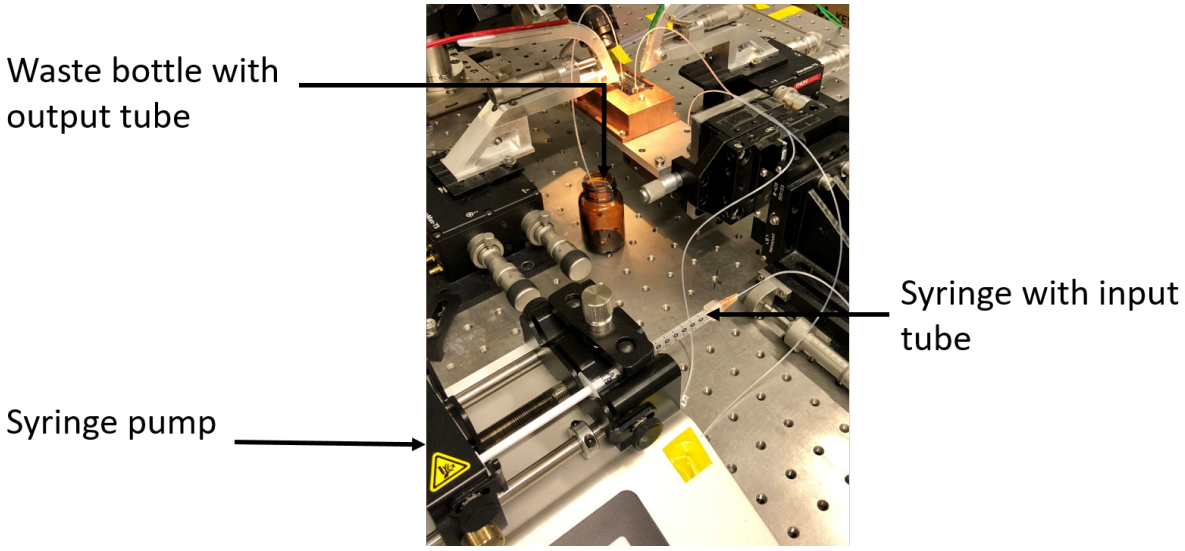

Figure 3.20: The syringe pump experimental set-up with sample in syringe, input tube, optical set-up and waste bottle.

Figure 3.21 shows the absorption spectra for waveguides of 150 μm, 190 μm, 240 μm, 340 μm, and 640 μm interaction lengths, where the absorption spectrum for IPA is clearly visible. The theoretical waveguide absorption spectrum for a waveguide length of 640 μm, taken from figure 3.12 and scaled for length, is also plotted on figure 3.21, showing excellent agreement between experiment and theory.

Figure 3.22 shows the measured waveguide absorption of pure IPA at a wavelength of 3.77 μm for interaction lengths of 150 μm, 190 μm, 240 μm, 340 μm and 640 μm. The gray line shows the theoretical prediction from the data in figure 3.3. There is very good agreement between the theoretical and experimental results. A clear trend showing that when the interaction length increased, the absorption also increased can be seen. The small deviations from the simulation may be from noise (e.g. fiber drift).

One aim of this sensing project is to obtain a spectrum which can be used to identify a specific sample. The other aim is to measure the concentrations of chemicals in the sample. Therefore, after getting the spectra of pure IPA with different interaction lengths, measuring concentrations of water-IPA solutions with different interaction length waveguides should be the next step.

A 150 μm interaction length waveguide was chosen for the first measurement. This would be the waveguide with the most output power as per the Beer-Lambert law.

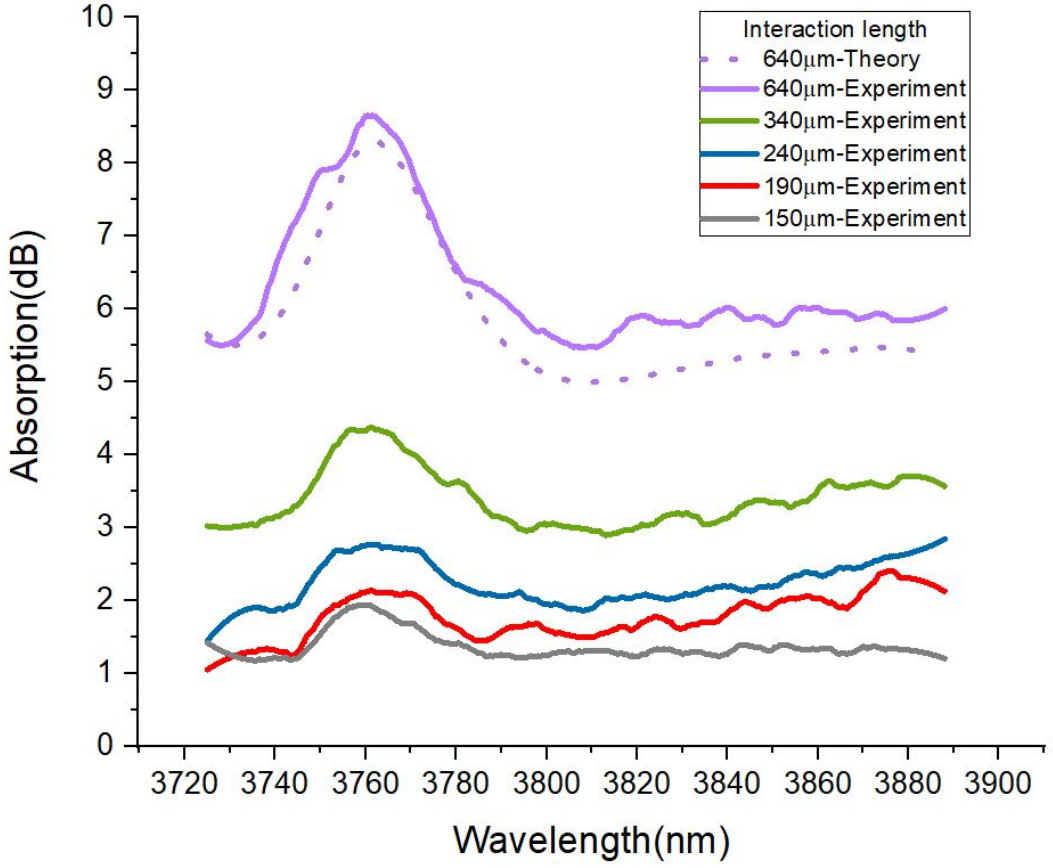

Figure 3.21: Measured absorption spectra of pure IPA on SOI rib waveguides with different interaction lengths and the simulated absorption spectrum for a waveguide of length equal to 640 μm.

Firstly, water was pumped into the microfluidic channel to coat the waveguide, and the background transmission signal (P_{water}) was measured with the waveguide being covered with pure water. Mixtures of 5%, 10%, 15%, 20%, 40%, 60%, 80%, 100% IPA (by volume in water) were then pumped through one by one. Between pumping each different concentration of the water-IPA mixture, air was pumped into the microfluidics channel to flush out the previously measured liquid sample. Once the sample was inside the microfluidic channel, a single output power was recorded from the photodetector, giving the value of the output signal ($P_{analyte}$). This was performed for each IPA solution.

After getting the output signal of pure water and water-IPA mixture solutions, the absorption (in dB) of the different concentration water-IPA solutions was calculated at 3.77 μm wavelength. The absorption (AB) was defined by equation 3.1:

$$AB(dB) = 10 * log_{10}\frac{P_{analyte}}{P_{water}} \tag{3.1}$$

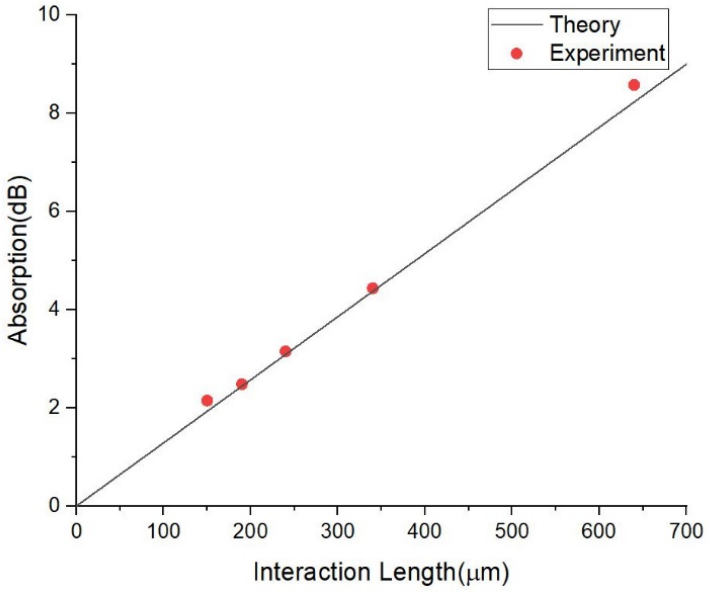

Figure 3.22: The experimental (red points) and theoretical absorption (straight line) of IPA at 3.77 μm, for varying interaction lengths.

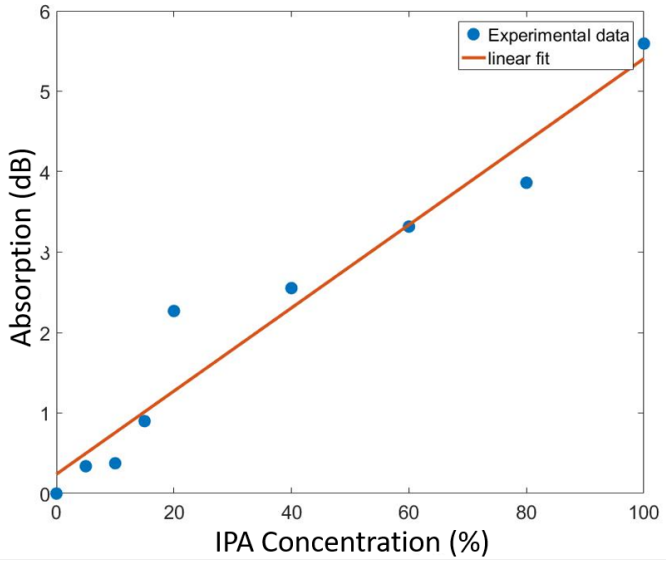

Figure 3.23: Absorption plot of a 150 μm interaction length SOI rib waveguide sensor with different IPA-water mixtures at 3.77 μm. The minimum concentration of IPA (in volume) that can be measured by the sensor on SOI waveguide is 5%. Due to the device being used for purely demonstrative purposes, error bars have not been added.

As figure 3.23 shows, when the concentration of IPA in water was increased, the absorption also increased. The lowest concentration of IPA (by volume) measured by the 150 μm interaction length SOI rib waveguide with microfluidics was 5%. This is because the interaction length is too short to detect lower concentrations of water-IPA mixtures.

To improve the sensitivity of this sensor system, a longer interaction length (640 μm) waveguide was used to measure lower concentrations of water-IPA mixtures.

The next step used the 640 μm interaction length waveguide to measure a minimum concentration of 3% of IPA with water by volume. The measurement with the 640 μm interaction length waveguide was consistent with the 150 μm interaction length waveguide measurements. Ten measurements were completed with 0%, 3%, 6%, 9%, 12%, 15%, 18%, 21%, 24%, 27% , 30% IPA (by volume in water), as seen in figure 3.24.

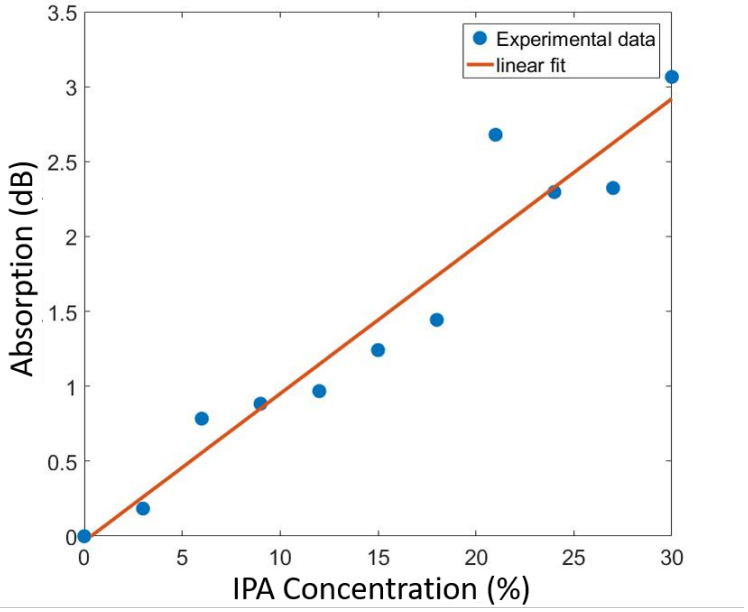

Figure 3.24: Absorption plot of a 640 μm interaction length SOI rib waveguide sensor with different IPA-water mixtures at 3.77 μm. The lowest concentration of IPA (in volume) that can be measured by the sensor on SOI waveguide was 3%.

As figure 3.24 shows, the lowest concentration of IPA (by volume) measured by the 640 μm interaction length SOI rib waveguide with microfluidics was 3%. However, the absorption spectrum sensing can not only just detect the concentration of a sample, but can also be used to distinguish between different samples' spectra. At 640 μm interaction length, the waveguide can also identify the spectrum of pure water and pure IPA, which are shown in figures 3.25 and 3.26. Compared to the literature results of water (figure 2.32) and IPA (figure 2.33) spectra between 3.725 - 3.888 μm, the experimental spectra can detect the IPA absorption peak at 3.77 μm, and the water spectrum is almost flat which is as expected.

With the success of the 640 μm devices, to try and push the capabilities of this sensor system to smaller concentrations, a longer interaction length (1893 μm) waveguide with a microfluidic channel was used to measure various concentrations of water-IPA mixtures at a wavelength of 3.77 μm. A longer interaction length should mean that a

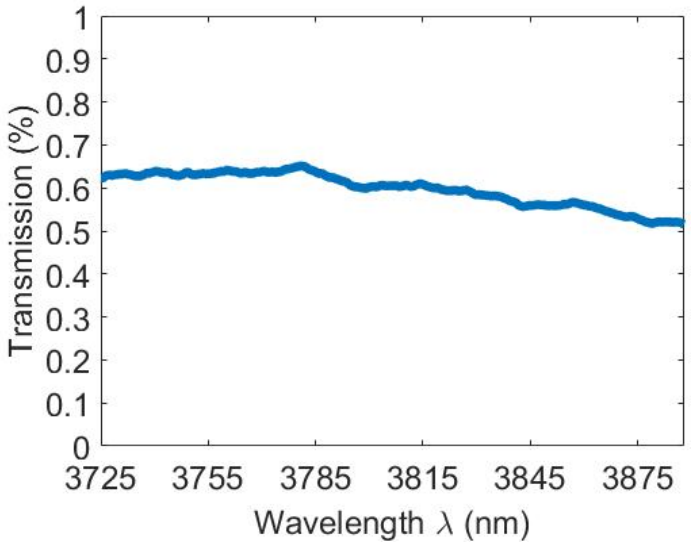

Figure 3.25: Pure water spectrum on 640 μm interaction length SOI rib waveguide with a microfluidic channel.

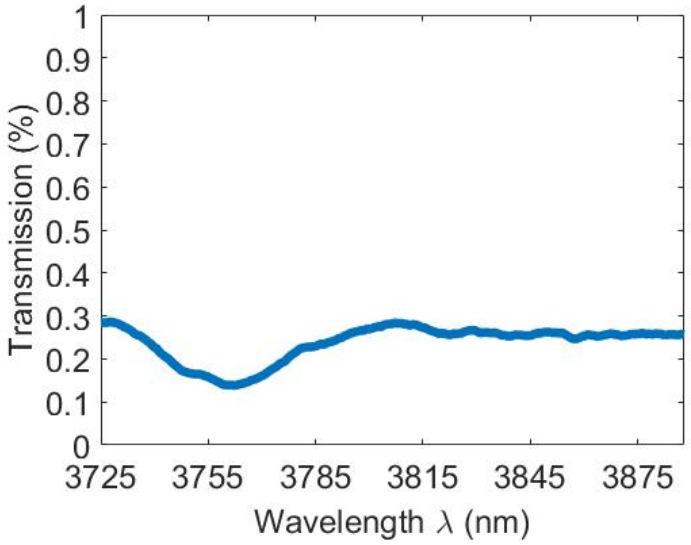

Figure 3.26: Pure IPA spectrum measured with a 640 μm interaction length SOI rib waveguide with microfluidics channel.

lower concentration of IPA in water could be detected. Firstly, to obtain the background transmitted power, DI water was pumped through the microfluidic channel to surround the waveguide, and the transmitted power (P_{water}) was measured. 10 mixtures of between 1% and 10% IPA (by volume) in water were then pumped through one by one, and the transmitted power ($P_{analyte}$) was recorded for each one. Figure 3.27 shows the measured waveguide absorption with IPA concentration together with a line of best fit (in red). The standard error Sy/x [95] is ± 0.25dB. This was calculated by equation 3.2:

$$Sy/x = \sqrt{\frac{\sum (y_i - \hat{y}_i)^2}{(n-2)}} \tag{3.2}$$

where y_i is the value of experimental absorption in dB, $\hat{y}_i$ is the value predicted from the actual absorption using the regression equation and n is the number of samples. This results in a limit of detection (deduced as the concentration corresponding to three times the standard error divided by the gradient 0.5) of 1.5% IPA in water. The error bars on figure 3.27 represent the standard error. The limit of detection comes from the smallest discernible change in transmission, which is limited by total absorption and background noise/fluctuations.

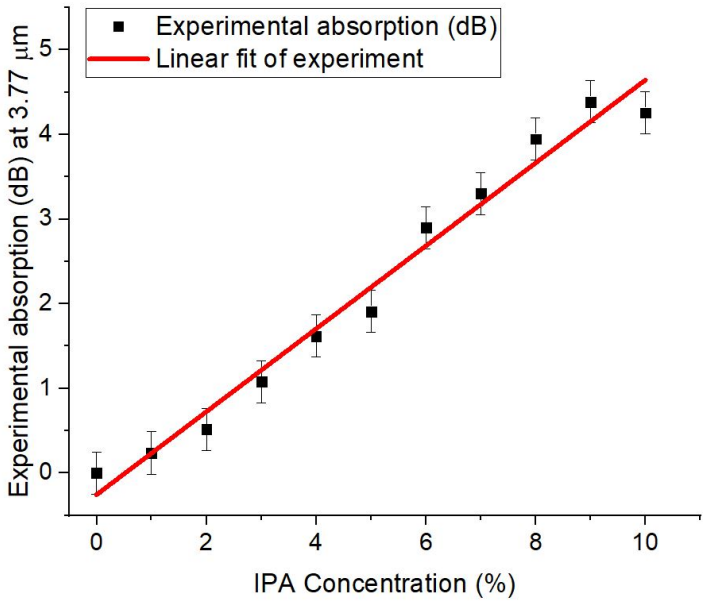

Figure 3.27: The experimentally measured absorption of water-IPA mixtures relative to transmission through 100% water, for varying IPA concentrations. The points show the experimental values and the red line is a linear fit to the data of 1893 μm interaction length SOI rib waveguide sensor, the error bars show the standard error $\pm$ 0.25dB.

Experiments were also performed on a waveguide with an interaction length of 3179.3 μm. Concentrations of 1% IPA in DI water and 2% of IPA in water were tested, as it was expected that these low concentrations could be analysed with such a large interaction length. However, the results showed a 10.28 mV and a 10.14 mV response in the detector for the 1% solution and the 2% solution respectively. This difference of 0.14 mV is close to the noise floor of the detector, of 0.1 mV. Furthermore, losses due to fibre drift also limit this response. It is expected that due to the large interaction length and bend loss in the design leads to too much absorption from water. To further characterise this device, a better detector would be needed, which would incur high cost, or for the noise arising from fibre drift to be removed.

In this apparatus, the major factor limiting the smallest measurable change in transmission is believed to be the drift and vibration of the fibre position. The temporal variation of input and output coupling efficiency was the dominant noise source. This could be eliminated in future designs by robustly packaging the input and output fibres with the chip or including an on-chip reference branch to normalise out fibre input coupling fluctuations.

3.7.2 Propagation loss measurements of SOI waveguide

Propagation loss measurements were performed using the well known cut-back method [96], in which 9 waveguides with different length (see figure 3.28) were used. The shortest waveguide's length was 1 mm, with the difference between waveguide being 1 mm to a maximum of 9 mm.

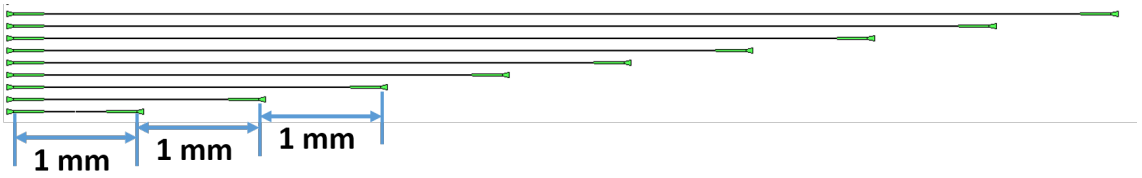

Figure 3.28: The mask design for cutback measurements to calculate propagation loss.

As figure 3.29 shows, the average propagation loss of the SOI waveguides at a wavelength range of 3.725 - 3.888 μm is 6.7 dB/cm. This value is higher than simulation value, as these waveguides were deposited with a 2 μm silica layer which are not present in the simulations, and silica has high absorption in the MIR range (see section 2.2.1.1). As Chapter 4 will use the same waveguide design, the propagation loss measurement was not repeated.

3.8 Conclusion

In summary, a SOI chip integrated with a microfluidic channel and operating at a wavelength range of 3.725 - 3.888 μm was used for detection of different concentrations of IPA in water. Several different interaction lengths of SOI waveguides (150-3179 μm) were used. A limit of detection (defined in section 3.7) of 1.5% IPA in water was achieved with an interaction length of 1893 μm.

From the results, it can be seen that the longer interaction length devices can produce a higher sensitivity. However, there are several visible limits of detection of this system, such as the intrinsic abilities of the detector, fiber drift causing noise and the bend loss of spiral waveguides lowering the output signal of the device. To therefore calculate

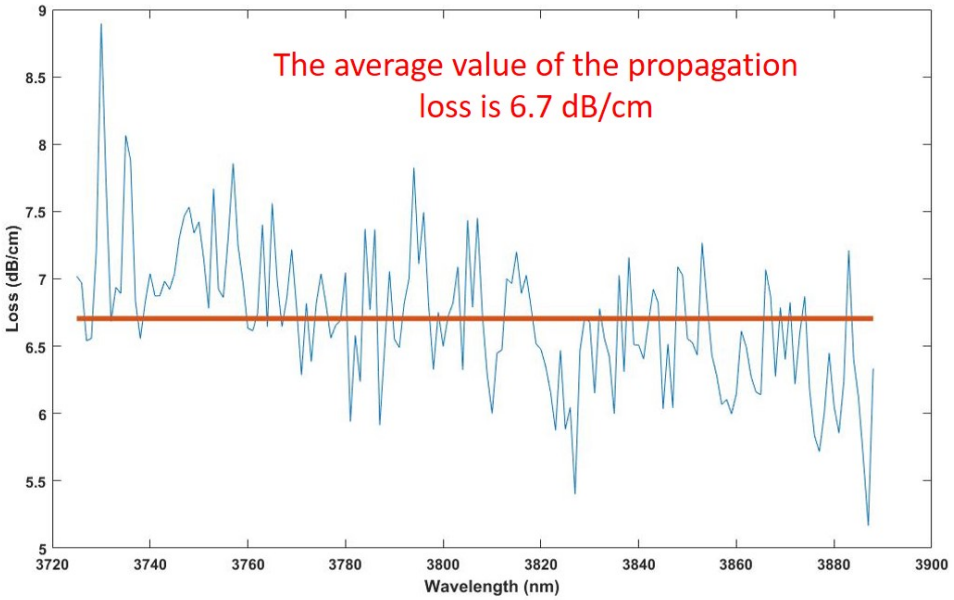

Figure 3.29: The propagation loss spectrum of SOI waveguides at a wavelength range of 3.725 - 3.888 μm, the average value of the propagation loss is 6.7 dB/cm.

a theoretical model of the detection limit of such a device plotted against interaction length, there are too many factors to accurately calculate a definitive detection limit. For the experiments discussed, the 1893 μm device was able to produce a high detection capability. Confidence in this interaction length means that it can be considered for future devices.

A modified version of this system will in the future be used to detect clinically relevant analytes in the 3.3 μm wavelength range. This device is a rib SOI waveguide with a width of 1.1 μm and it can function at 3.3 μm wavelength to detect aspirin and paracetamol. The input mechanism for the light is butt-coupling rather than grating coupling.

Chapter 4

Integrated switching circuit for low-noise self-referenced mid-infrared absorption sensing using silicon waveguides

This chapter will report a demonstration of an on-chip liquid absorption sensor in the mid-infrared wavelength region using low loss silicon-on-insulator (SOI) waveguides which incorporates switches and a microfluidic channel. The fatal dose of alcohol in the bloodstream for humans is calculated to be around 0.5% [97]. It is therefore important for medical devices to be able to measure concentrations at or below this value. Noise in absorption measurements can be a major limiting factor to the potential of many devices, and is often caused by random fluctuations of transmission through the sensor. Chapter 3 showed that SOI waveguide can be used to measure IPA-water mixtures, and an issue arose with the limit of detection (LOD) restricted by the noise arising from both the experimental setup and environmental issues, such as the vibration of the input and output fibers. This occurs due to the reference and sample measurements occurring asynchronously.

A solution to this problem is to lower the noise floor of a SOI waveguide evanescent absorption sensor by integrating a pair of switches into the circuit, so that the circuit switches the light between a sensor waveguide and a reference waveguide at a rate of a few kHz. If this switching frequency is higher than the noise frequency, measuring the relative transmission of the two arms in two successive measurements can help to reduce the noise of the absorption measurement. In all tests, an external light source and an external detector were used. The switch sensor was integrated with a microfluidic channel, and its performance was verified by using it to measure the absorption of water-IPA solutions. The device was used to detect an IPA absorption peak near 3.77

μm wavelength. It is hoped that the introduction of the switches to the device will make the low frequency common noise components to be removed from the measurement.

4.1 Sensing circuit and measurement scheme

Figure 4.1 shows a diagram of the integrated switching circuit (excluding grating couplers) for low-noise self-referenced sensing using silicon waveguides:

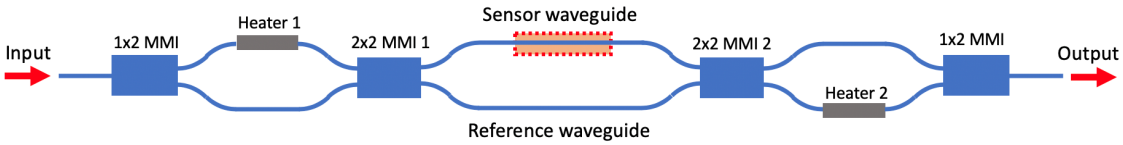

Figure 4.1: Schematic diagram of the sensing circuit.

The electric field output of the full device (E_{out}) can be calculated by multiplying together the input electric field (E_{in}) with the S-matrix elements of each component in the full circuit (where the S-matrices describe the relationships between the electric fields at the input and output ports of each device):

$$E_{out} = S_{2X1MMI} \times S_{heater2} \times S_{2X2MMI} \times S_{sensor} \times S_{2X2MMI1} \times S_{heater1} \times S_{1X2MMI} \times E_{in} \tag{4.1}$$

For simplicity we (unrealistically) assume that there is no insertion loss in any of the multimode interferometers (MMIs) in this model, since any insertion loss would simply contribute to the insertion loss of the whole switch. For the 1x2 MMI we also assume that there is no imbalance or phase error (since the 1x2 MMI is inherently symmetrical without significant fabrication defects):

$$S_{1\times2MMI} = \frac{1}{\sqrt{2}} \begin{bmatrix} 1 \\ 1 \end{bmatrix} \tag{4.2}$$

For the 2x2 MMIs we assume that there is an imbalance $B = \dfrac{P_{out}}{P_{in}}$ where P_{out1} and P_{out2} are the optical intensities at the two output ports, and the electric fields at the output ports are $E_{out1} \propto \sqrt{P_{out1}}$ and $E_{out2} \propto \sqrt{P_{out2}}$. We also assume that there is a phase error ξ between the two output ports. Then:

$$S_{2\times2MMI} = \frac{1}{\sqrt{B+1}} \begin{bmatrix} \sqrt{B} & e^{j(\frac{\pi}{2}+\xi)} \\ e^{j(\frac{\pi}{2}+\xi)} & \sqrt{B} \end{bmatrix} \tag{4.3}$$

For the two waveguide arms in the switch Mach-Zehnder interferometer (MZI), where the waveguides are of the same length but a thermo-optic phase shifter in the upper arm has a phase change $\Delta\phi$ applied to it, we insert a phase error θ (but do not include an unbalanced loss in the two arms as the 2x2 MMI imbalance creates a similar effect):

$$S_{heater1} = \begin{bmatrix} e^{j(\Delta\phi+\theta)} & 0 \\ 0 & 1 \end{bmatrix} \tag{4.4}$$

and

$$S_{heater2} = \begin{bmatrix} 1 & 0 \\ 0 & e^{j(\Delta\phi+\theta)} \end{bmatrix} \tag{4.5}$$

In this experiment the two heaters were placed in opposite arms of the two switches to simplify the layout design, and experimental measurement, but they could be placed in either arm of the switch, in which case the s-matrices should be adjusted accordingly. In the sensor arm the analyte introduces an absorption change$\Delta\alpha$ (in dB), with an accompanying transmission change ΔT=$10^{-\frac{\Delta\alpha}{10}}$ and an effective refractive index change Δn_{eff} that produces a phase change $\Delta\phi$. The s-matrix for the sensor arm and reference arm combined in parallel (assuming no phase error or insertion loss in the reference arm) is then:

$$S_{sensor} = \begin{bmatrix} \sqrt{\Delta T}e^{j(\Delta\phi)} & 0 \\ 0 & 1 \end{bmatrix} \tag{4.6}$$

Figure 4.2 (a) shows a map of the theoretically calculated transmission for all possible combinations of phase shift, for an ideal circuit with no fabrication errors. Three points are marked on the map:
1. "S"= (1.5 π, 0.5 π) – the phase shift to switch the light to the sensor arm and to receive the light from the sensor arm, i.e. the sensor arm transmission.
2. "R"= (0.5 π, 1.5 π) – the phase shift to switch light to the reference arm and to receive light from the reference arm, i.e. the reference arm transmission.
3. "Z"= (0.5 π, 0.5 π) – the phase shift to switch light to the sensor arm but to receive it from the reference arm, i.e. a "zero" position where the transmission is minimized.
The waveforms shown in figure 4.2 (b) and (c) are applied to the two phase shifters so that in time slot A (equal to half of the measurement time) the light is modulated between the "S" and "Z" positions, and in time slot B the light is modulated between the "R" and "Z" positions.

The resulting relative optical transmission for the whole device takes the form shown in figure 4.2 (d). The modulation in time slot A is applied at frequency f_A, while the

modulation in time slot B is applied at frequency f_B. The sensor waveguide transmission S-Z is then retrieved by using a lock-in amplifier operating in dual reference mode to isolate the signal at frequency f_A, and the reference waveguide transmission R-Z at a different frequency f_B is simultaneously retrieved in the same way. The change in transmission due to the analyte is then found from the ratio (S-Z)/(R-Z). When using thermo-optic phase shifters the two frequencies f_A and f_B can be in the kHz regime so that the modulation frequency is higher than the frequency of most mechanical vibrations in our setup.

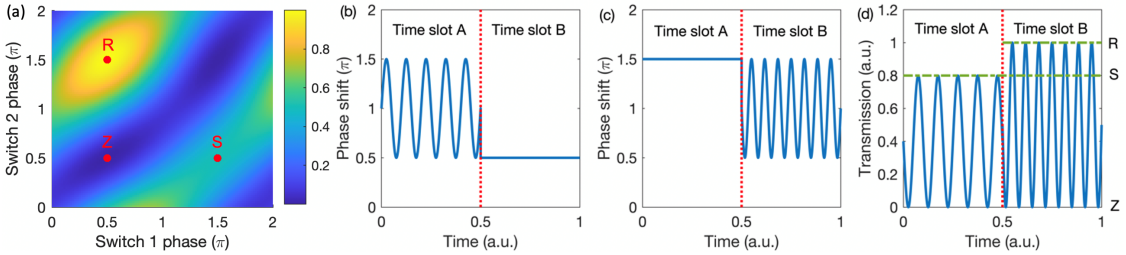

Figure 4.2: (a) Map of transmission intensity for varying switch phase shifts, (b) and (c) phase shifts applied to the first and second switches respectively in each full time period, (d) overall switch transmission over a full time period.

The definition of the following variables for transmission through the device in four possible cases:

I_S = transmission when the switches are configured for maximum transmission through the sensor arm, i.e. point "S"

I_R = transmission when the switches are configured for maximum transmission through the reference arm, i.e. point "R"

I_Z = transmission when the switches are configured for minimum overall transmission, i.e. point "Z"

I_{S0} = transmission when the switches are configured for maximum transmission through the sensor arm, i.e. point "S", in the specific case when no analyte has been introduced to the sensor. This is effectively the background transmission.

We can additionally assume that there are likely to be different losses in the sensor and reference arms even when no analyte is introduced to the sensor arm (e.g. because of a different waveguide top cladding absorption in the sensing windows, or from losses at the point where there is a transition in the sensing arm between the silica top cladding and an air or liquid top cladding), such that $I_{S0} = T_0\, I_R$. T_0 is the transmittance of the sensor arm when there is no analyte. In that case we can say that the transmittance of the waveguide when an analyte is introduced is T_a, and that it can be calculated from:

$$T_a = \frac{I_S}{I_{S0}} = \frac{I_S}{T_0 I_R} \tag{4.7}$$

Random variations in the laser power or in the coupling efficiency to and from the chip would have the effect of multiplying the transmissions at all operating points in a particular instant by the same scaling factor N, so that

$$T_a = \frac{NI_S}{I_0 N I_R} = \frac{I_S}{T_0 I_R} \tag{4.8}$$

Thus these noise components can cancel out if the two absolute transmissions are measured simultaneously. In this approach the time between measurements is kept as small as possible, so as to remove lower frequency noise components. However, if in this approach there is continuous modulation between the points "S" and "Z" in time slot A and between "R" and "Z" in time slot B, and a lock-in amplifier is used to measure the amplitude of the resulting optical signal in the two time slots, then the difference in intensities of "S" and "Z" compared to "R" and "Z" are measured, which is called M_S and M_R:

$$M_S = I_S - I_Z \tag{4.9}$$

$$M_R = I_R - I_Z \tag{4.10}$$

In a perfect MZI switch the value I_Z would be equal to zero, but in practice the MZI switches have finite extinction ratios, so that I_Z has a non-zero value. With the noise scaling factor N these become:

$$M_S = N(I_S - I_Z) \tag{4.11}$$

$$M_R = N(I_R - I_Z) \tag{4.12}$$

However, calibration measurements of the extinction ratios can be performed from the "S" and "R" positions compared to the "Z" position (ER_{S0} and ER_R), using a DC optical signal before an analyte is introduced, since these extinction ratios of the switches would not change after an analyte is introduced, and in this case the noise can be removed by averaging.

$$ER_{S0} = \frac{I_Z}{I_{S0}} \tag{4.13}$$

$$ER_R = \frac{I_Z}{I_R} \tag{4.14}$$

Combining equation 4.11 and equation 4.13 together:

$$M_S = N(I_S - I_{S0}ER_{S0}) = N(I_S - \frac{I_S}{T_a}ER_{S0}) \tag{4.15}$$

$$I_S = \frac{M_S}{N(1 - \frac{ER_{S0}}{T_a})} \tag{4.16}$$

And combining equation 4.12 and equation 4.14 together:

$$M_R = N(I_R - I_R ER_R) \tag{4.17}$$

$$I_R = \frac{M_R}{N(1 - ER_R)} \tag{4.18}$$

From earlier equation 4.7, equation 4.16 and 4.18

$$T_a = \frac{I_S}{T_0 I_R} = \frac{\frac{M_S}{N(1 - \frac{ER_{S0}}{T_a})}}{\frac{T_0 M_R}{N(1 - ER_R)}} \tag{4.19}$$

Finally, rearranging for T_a and substituting in equation $I_{S0} = T_0\ I_R$, equation 4.13 and equation 4.14 get:

$$T_a = ER_{S0} + \frac{M_S}{T_0 M_R}(1 - ER_R) = ER_{S0} + \frac{ER_{S0}M_S}{ER_R M_R}(1 - ER_R) \tag{4.20}$$

$$T_a(dB) = 10\log_{10}\left(ER_{S0} + \frac{ER_{S0}M_S}{ER_R M_R}(1 - ER_R)\right) \tag{4.21}$$

Alternatively, the absorption loss induced by introducing the analyte can be expressed as an absorption A_a(dB)= -T_a (dB). Notice that in this final expression the noise term N has been cancelled out. Therefore, if E_{S0} and ER_R before the analyte is introduced can be accurately measured, and if the set-up is able to simultaneously measure M_S and M_R in the presence of the analyte, then the analyte absorption A_a can be measured without multiplicative noise.

4.2 Theoretical investigation of the effect of fabrication and calibration errors on measured absorption

In this section the theoretical model described in section 4.1 is used to explore how design, fabrication, or calibration errors can affect the accuracy of the sensor region absorption measured using the device. The absorption error is defined as:

$$absorption\ error(\%) = 100 \times \left(\frac{measured\ sensor\ region\ absorption(dB)}{actual\ sensor\ region\ absorption(dB)} - 1 \right) \quad (4.22)$$

$$= 100 \times (\frac{A_a}{A} - 1) \quad (4.23)$$

The phase errors in the switch arms (θ_1 and θ_2) and the phase shifter efficiencies can be calibrated and compensated for by measuring a 2D map of the overall switch transmission with varying powers applied to the two heaters, in order to find the heating powers required to set the device to the "S", "R", and "Z" positions. The remaining principal fabrication errors that would alter the device response are then the imbalances of the two 2 ×2 MMIs (B_1 and B_2) and their phase errors (ξ_1 and ξ_2).

Figure 4.3 (a) shows a contour map of the absorption error for a range of imbalances and phase errors, with $B_1 = B_2$ and $\xi_1 = \xi_2$, when measuring an analyte with $A = 3$ dB and the calibration was carried out in the presence of an analyte for which $A = 5$ dB. From the contour map it can be seen that the error stays <1% if the imbalance is within approximately <±3 dB and the phase error < 5°, and also that this error can become very large for large imbalances and moderate phase errors.

Furthermore, the absorption error arising from the MMI phase error and imbalance depends strongly on the difference between the sensor region absorption during the measurement and during the calibration of the device extinction ratios E_{S0} and ER_R, as depicted in figure 4.3 (b), which shows the magnitude of the absorption error when the sensing region absorption is varied between 0 dB and 20 dB, and when the calibration is performed at three specific sensing region absorption values. In each case the errors are dramatically smaller when this difference in absorption is small, implying that the calibration should be carried out using a background sample whose absorption is as close as possible to the target analyte absorption.

It can also be expected that inaccurate estimation of the phase shifter efficiencies and phase errors (θ_1 and θ_2) will lead to error in the measured absorption since the positions of "R","S", and "Z" will be inaccurate. For simplicity we have estimated the absorption error when only one of these three measurement points is inaccurate at any one time, and find that absorption is most sensitive to the "Z" position. Figure 4.3 (c) shows the absorption error when the phase shift applied to each heater for the "Z" position

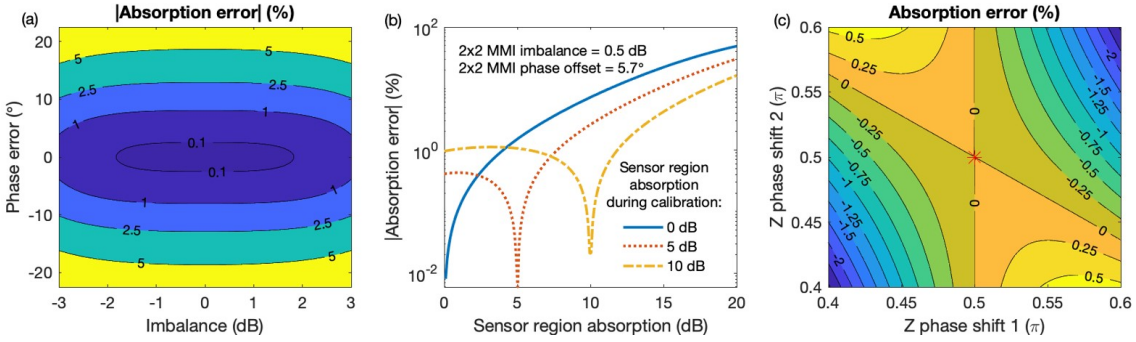

Figure 4.3: Plots showing the theoretical percentage error in the measured analyte region absorption (compared to the actual analyte region absorption) in the presence of different fabrication or calibration errors: (a) Contour map showing the error when different combinations of equal imbalances and phase errors are present in the two 2×2 MMIs. (b) Line plot showing how the magnitude of the error varies for different actual sensor region absorptions, in the situation when the 2×2 MMIs each have an imbalance of 0.5 dB and phase offset of 5.7°. Three lines are shown that illustrate how the error vs. actual absorption relationship changes when switch calibration is performed at different values of sensor region absorption. (c) Contour map showing the error when the "Z" is incorrectly calibrated, i.e. when the phase shifts applied using the heaters in the two switches are varied around the ideal "Z" position, 0.5π, 0.5π (which is marked on the figure with a red star). In figure (a) and (c) the sensor region absorption is set to 3 dB during calibration and 5 dB during measurement.

is varied in the range 0.4 - 0.6 π (with the ideal position being (0.5 π, 0.5 π)). This calibration error on its own appears to result in smaller absorption errors than the those arising from B and ξ.

Overall, these calculations suggest that great care should be taken to minimize the MMI imbalance and phase error during device design and fabrication, to accurately calibrate the thermo-optic phase shifters, and to perform the extinction ratio calibration at a background absorption close to the target analyte absorption. With typical fabrication and calibration errors the absolute error in the absorption measured using the device could be in the range of a few % even before noise is considered (as the fabrication error will affect the "Z", "R", "S" positions, and hence have an effect on the values of the E_{S0} and ER_R, based on equation 4.21. The measured absorption of the analyte will therefore be different to the actual absorption of the analyte).

4.3 Switch Sensor Mask design

The SOI waveguide design is the same as the waveguide in Chapter 3, comprising a Si rib waveguide this design integrated a switching circuit to switch the light between sensor waveguide and reference waveguide. As figure 4.4 shows, this mask design is made from multiple features. These include the quality control marks (labelled as QC in the

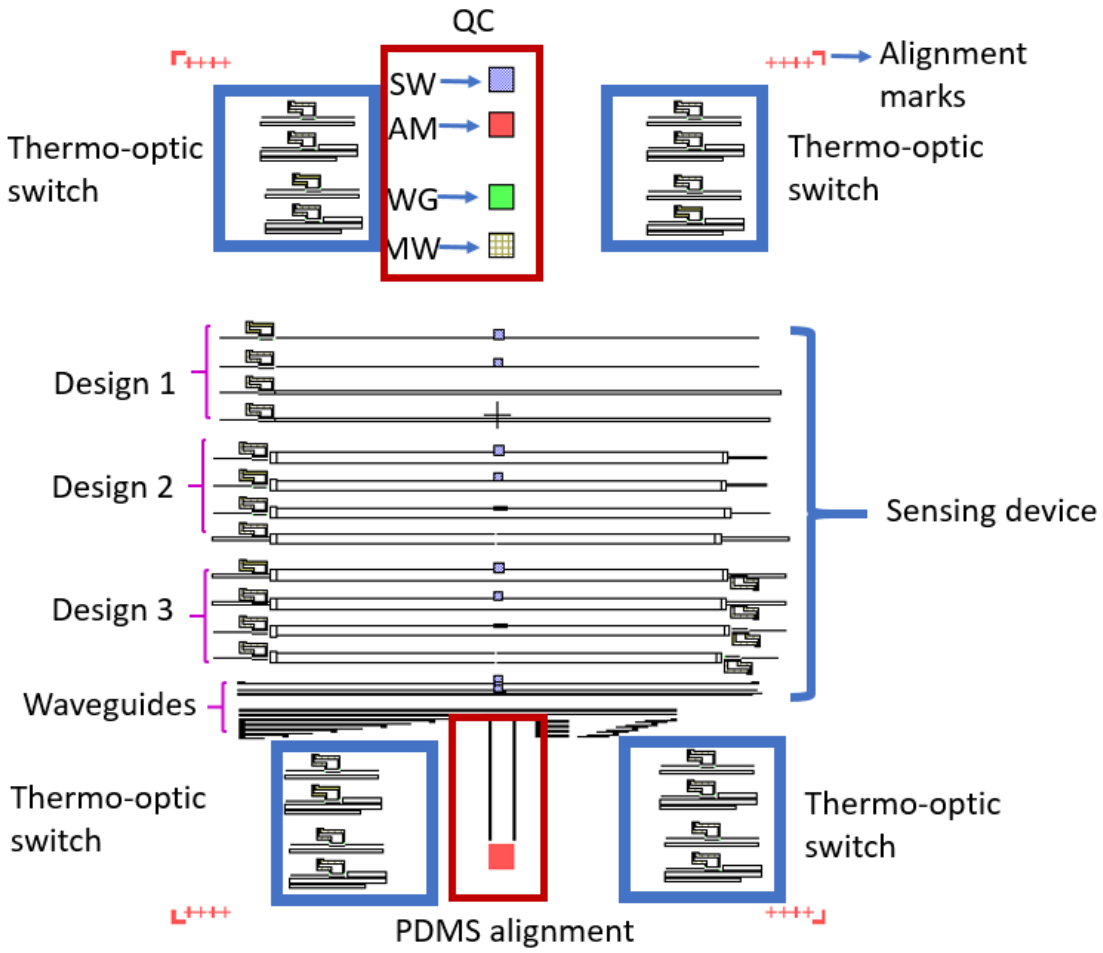

Figure 4.4: Mask design of the integrated switch on silicon rib waveguide for liquid sensor.

figure), alignment marks, the thermo-optic switches, the sensing device (including three different designs), and various waveguides.

The quality control marks show patterned boxes indicating the layers of the different parts of the device, which can be used for measuring the layer thickness during lithography and etching, by ellipsometry. There are five patterned boxes with each box representing one layer of the mask. The SW box corresponds to the sensing window layer, the AM box corresponds to the alignment mark layer, WG corresponds to the waveguide layer, and MW links to the layer of metal which is deposited on the heaters.

The alignment marks are at four corners in the mask, and are used to align the chip when the chip needs to be diced and they can also be used to help the e-beam lithography to find the chip position in the wafer. This allows for control during the e-beam exposure helping to reduce fabrication error.

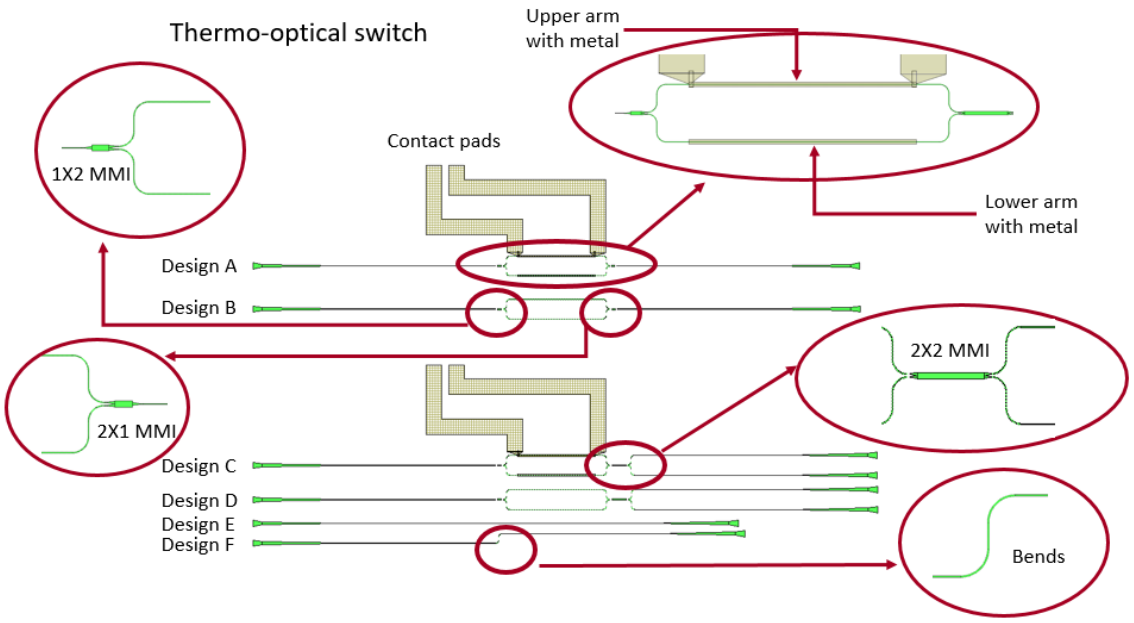

Figure 4.5: Mask design of the thermo-optic switch.

The design of the thermo-optic switch is highlighted in figure 4.5 as this mask design has multiple features such as design A, design B, design C, design D, design E, and design F.

Design A and design B are one set, which aimed to test the thermo-optic MZI to see if it works. Design A has one input and one output waveguide with grating couplers and tapers, and a thermo-optic MZI. The thermo-optic MZI includes a 1×2 MMI as a light splitter, an upper arm and a lower arm, and a 2×1 MMI as the light coupler. The upper arm and the lower arm have metal deposited on top, and contact pads which are used to connect with electrical probes. Compared to design A, design B does not have metal deposited on top of the upper arm and the lower arm. It also does not have contact pads. The overall aim of design B is it can be used to compare with design A.

Design C in figure 4.5 shows an integrated thermo-optic switch, which includes a 1×2 MMI, an upper arm and a lower arm, and a 2×2 MMI. The upper arm and the lower arm have metal deposited on top, and contact pads which are used to connect with electrical probes. Unlike design C, design D does not have metal deposited on top of the upper arm and the lower arm. If issues arise with design C, design D can be tested to see if the contact pads are the issue.

Design C and D are one set. Compared to design A and B, instead of one output port with a 2×1 MMI, they have two output ports with one 2×2 MMI which is used to test the 2×2 MMI element to ensure functionality. Design E and F are also one set, this set is used to test the waveguide to see if it can guide light. Design E is a straight waveguide, whereas Design F has two bends which can test if the bends are able to guide light well.

The sensing device area consists of three designs (see figure 4.4), which are design 1, design 2, and design 3. They all have sensor devices with four different interaction lengths. For each design, from top to bottom, the first device has an interaction length of 3.2 mm, the second device has an interaction length of 1.8 mm, the third of 500 μm and finally the bottom device has an interaction length of 100 μm. This therefore allowed the chip to be used for measurements of different concentrations, and potentially different analytes, which might have different absorption strengths, without the need for further fabrication. Design 3 is the switch sensing circuit, with the schematic diagram shown in 4.6. It has an input thermo-optic switch and an output thermo-optic switch (the principle of the thermo-optic switch is explained in section 4.1), as well as a sensor waveguide and a reference waveguide. This is the most complete design for the devices discussed in this section.

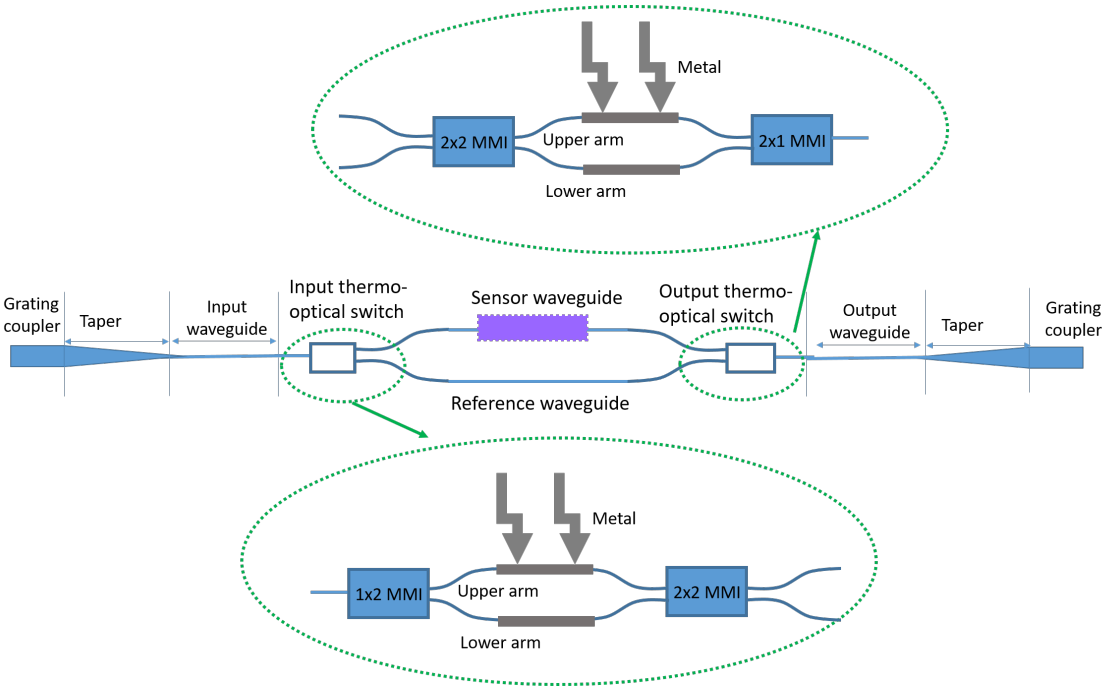

Figure 4.6: Mask design of the design 3 sensing device.

Design 2 is less complicated, it will be used in case design 3 does not work. Compared to design 3, design 2 (figure 4.7) does not have an output thermo-optic switch, instead a 2×1 MMI combines light from the sensor and reference arms into the output port. The other benefit of this design is that one thermo-optic switch needs to be driven instead of two, which would be a simpler experiment to perform. However, the disadvantage is that in theory you would get an extra -3 dB loss from not including the output switch. Unlike design 2, design 1 (figure 4.7) does not have a 1×2 input switch or a reference waveguide, it simply has a 1×1 thermo-optic MZI at the input, followed by a sensor waveguide. The main benefit of this design is to modulate the light; it removes the need to have another external bulk-optics component chopper. Instead the thermo-optic MZI is able to act as a chopper to encode a constant frequency onto the optical input. The

lock-in amplifier then isolates the signal at the desired frequency, and reduces the noise coming from other frequencies.

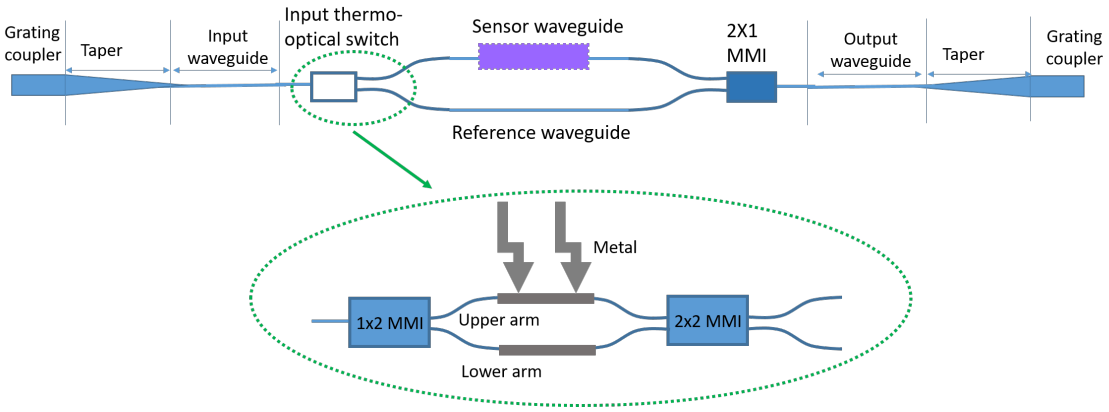

Figure 4.7: Mask design of the design 2 sensing device.

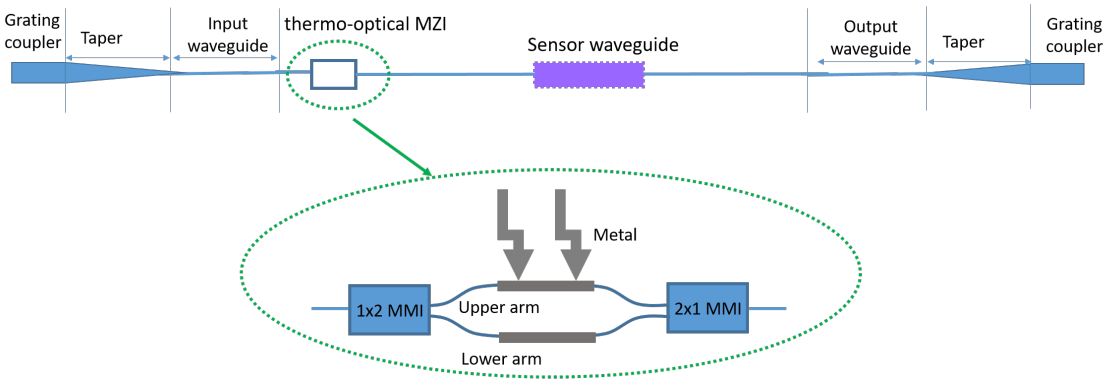

Figure 4.8: Mask design of the design 1 sensing device.

For the "waveguides" area of the mask, it includes a variety lengths of straight waveguides and bend waveguides. The straight waveguides will be used to test the propagation loss of the waveguide. The bend waveguides will be used to test if the waveguide can guide light or not, and it can also be used to measure the bend loss.

4.4 Fabrication

For the fabrication process (figure 4.9), the 500 nm thick silicon chips (figure 4.9 (a)) were patterned by electron-beam lithography, and etched using an Oxford Instruments ICP 380 system to etch 450 nm of Si and to create the rib waveguides (figure 4.9 (b)). This lithography process was described in Chapter 3. A 2 μm SiO_2 cladding layer was deposited on the top surface of the chips by PECVD (figure 4.9 (c)), then the sensing windows were opened by HF wet etching (figure 4.9 (d)). Figure 4.9 (e) shows a spiral waveguide with sensing window, the spiral waveguide is used for longer interaction length while maintaining a small footprint. The lighter regions are the open sensing areas, while

the darker regions are those covered by the SiO_2 cladding layer. A 150 nm thick layer of aluminium was deposited on the surface of the SiO_2 to act as the heaters (figure 4.9 (f)). When the aluminum is heated up, the temperature of the surrounding silica is also raised. Therefore, the Si layer underneath (the thermo-optical switches) are also heated which in turn affects the optical properties of Si. For further information on the principle of the heaters, see section 4.1. To create the heaters, the following steps were taken. In the process, the photoresists used were MMA and PMMA. Firstly, MMA was spun onto the substrate at a speed of 2.5k rpm. It was then baked at 150°C for 1 minute and 15 seconds, then allowed to cool to room temperature. Then, PMMA (PMMA 495) was spun, at a speed of 6k rpm. This was baked at 180°C for 1 minute and 15 seconds, and again allowed to cool to room temperature. The last step involved a third photoresist called Espacer. E-beam lithography was then used to pattern the heaters in the design. Once the lithography was completed, water was used to remove the Espacer in the patterned region, then a N_2 gun was used to blow dry the wafer. A developer solution of MIBK : IPA mixed in a ratio of 1:1 was created, and then the wafer was placed inside the solution for 1 minute, then the wafer was submerged in IPA for 30 seconds, followed by a DI water rinse. The wafer was allowed to dry via an N_2 gun.

The Al was deposited for 750 seconds using the leybold helios system. The excess Al on the surface of the wafer needed to be removed with a lift off process. The lift off is completed by putting the wafer in a sonic bath with NMP for 10 minutes and 40 seconds. Then the wafer was spun with S1813 photoresist as a protective layer for the dicing step. The dicing was done using the Disco Saw tool to dice the wafer into individual chips of 36 mm height and 27 mm width. After dicing, water was used to rinse the surface of the chips, to remove the particulates which may be have fallen onto the chips during the dicing process. Then the chips were submerged in NMP for 4 hours, with an initial heating step of the NMP for 20 minutes at 50°C. The chips were left in the NMP overnight to remove the S1813. This leaves the patterned Al heaters in the desired location, with high accuracy.

Figure 4.9 (g) shows the PDMS channel after the bonding process to the chip. PDMS was used to fabricate the microfluidic channel to be bonded onto the surface of the SiO_2 cladding layer, because mature fabrication techniques are already available for this material [88]. Although PDMS has high mid-infrared absorption, the silica top cladding prevents the light from interacting with the PDMS [98]. A plasma asher was used to heat the silica and PDMS in an O_2 environment to cause covalent bonding between the two surfaces. The entire visible area is covered by a microfluidic channel which was 3 mm wide, 0.5 mm high and 20 mm long.

Table 4.1 shows the summary of the most critical steps in the fabrication process.

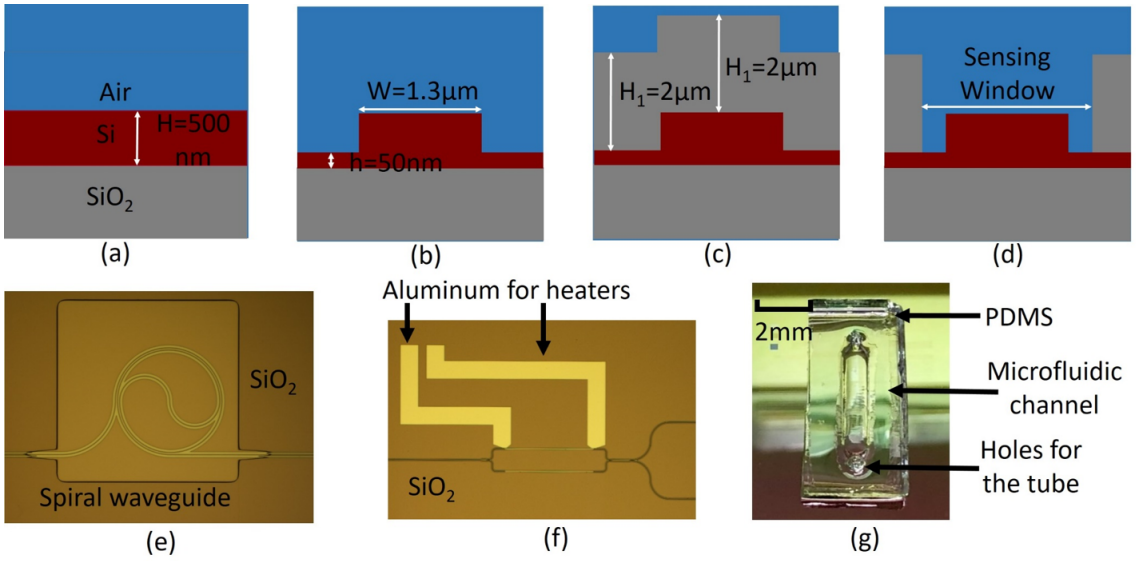

Figure 4.9: Fabrication process of SOI waveguides with PDMS microfluidics channel.

Challenge	Solutions
Lift off of Al	Use of an ultrasonic bath with NMP to remove the photoresist underneath the Al. To ensure that all the photoresist is removed, the chips are left in NMP overnight.
Ensuring ICP etching does not overetch	Calculating the total etching time needed based on experience of the Si etching rate, then perform 3 separate short etches. After every etch step, use of the ellipsometer to measure the thickness of etched Si.
Ensuring HF etching does not overetch	A low concentration of HF was used, HF:water = 1:20, which leads to a slow etching rate. This means there is more control on the etching of the silica.
Ensuring the Lithography is not overdeveloped	Use of the manufacturers suggested timing for development and use of gentle shaking when developing. By also using a large beaker for developing, it can be ensured that removing the chips from the developer liquid can be done easily and quickly, which helps keep the timing as accurate as possible.
Ensuring equal thickness of the photoresist on the chip	Resist was spun at a speed of 4370 rpm for 180 seconds. A high spin speed should correlate to good coverage of the chip. After the resist was deposited, the ellipsometer was used to measure the thickness of photoresist at different points of the chip.

Table 4.1: Summary of the most critical steps in the fabrication process.

4.5 Measurements

The experimental system is set up so that light can be coupled through the photonic circuit, and electrical signals can be applied to the two heaters through the use of electrical probes. The probes are held in place by clamps on 3-axis stages, and make mechanical contact with the heaters. A liquid sample can be pumped through the microfluidic channel by a syringe pump. The syringe pump's pump speed can be easily controlled, which is good for recording data at the computer. Figure 4.10 shows a diagram of the setup.

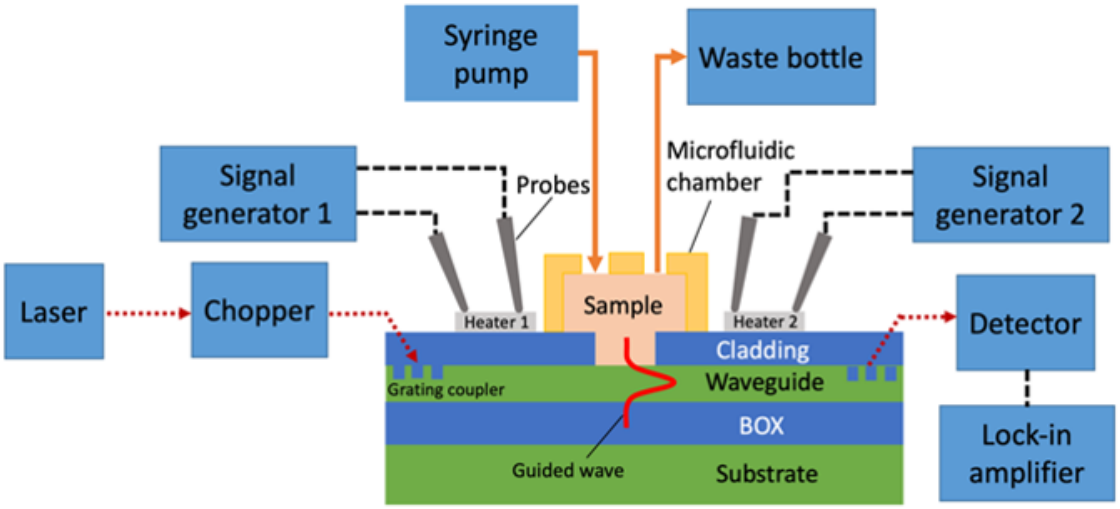

Figure 4.10: Diagram of the system layout.

Figure 4.11 shows a photograph of the system. The light source was a tunable QCL laser (3.725 - 3.888 μm) [43] and the light was coupled into a MIR fiber by a ZnSe lens, and then from the fibre into the waveguides using surface grating couplers (out of plane coupling). A pair of electrical probes were positioned on top of on-chip metal contact pads connected to each of the two heaters, using 3-axis micropositioners built in to the probe bases. At the output end of the photonic circuit, light was coupled to the output MIR fiber and subsequently to the MIR detector. A single use syringe pump forced the fluid sample through the microfluidic channel via input and output tubes. By using a new syringe pump for each measurement, it was ensured that there was no contamination to the sample. The chip (dimensions: 36mm $\times$ 27mm) was kept still during measurements using a vacuum stage.

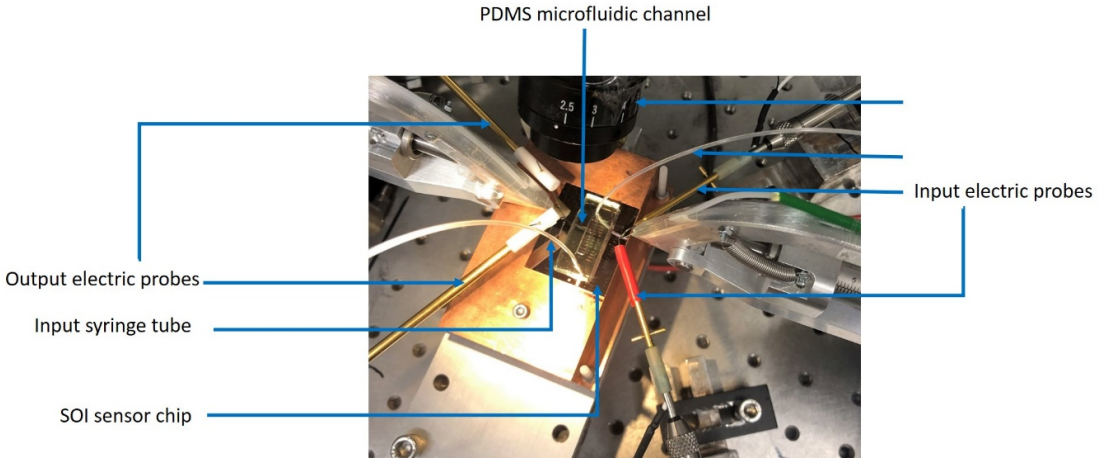

Figure 4.11: A photograph of the experimental apparatus for testing the sensor with a single use syringe pump, sample in the syringe, input tube, optical apparatus, output tube, and electrical probes.

4.5.1 Sensor calibration measurements

Before the sensor can be used, a calibration step is carried out to find the efficiency and phase offsets of the switches (mW/pi) (see figure 4.12). The power which needed to be applied to the heather was found which generates one π optical phase shift. The laser is set at 3.77 μm wavelength, because IPA has a signature absorption peak at 3.77 μm wavelength.

The first step is to find the heater's power range to make the light's phase change by 1.5 π, the reason was mentioned in chapter 4.1. Figure 4.12 shows the phase shift π corresponds to 0.0937 W, therefore, 1.5 π will correspond to 0.14 W. If the heater needs to make the light to shift 1.5 π phase shift, the heater should be able to withstand a power more than 0.14 W. The heater will need to withstand more than the power

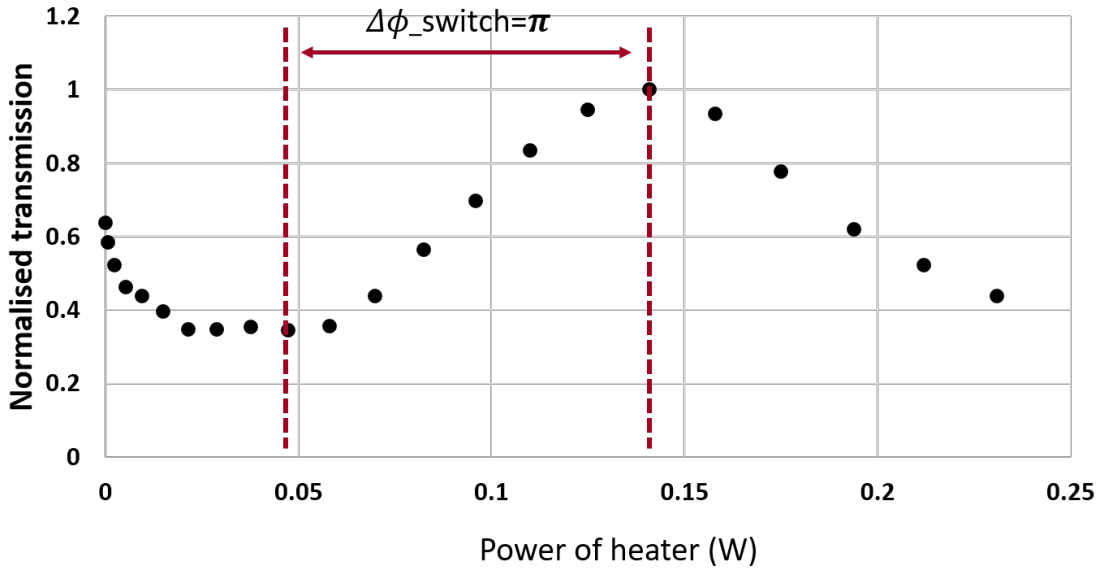

Figure 4.12: A normalised transmission with power of heater of a single thermo-optic switch device.

needed to create a 1.5 π phase shift, because there will also be some phase offset of the transmission. The second step is to test whether the heater can withstand more than 0.14 W or not. If it can work with more than 0.14 W, what is the maximum power that the heater can suffer, and for how long? The switch worked 0.2761 W power for more than 1 hour. It also can work under power 0.30 W, however after 30 minutes the heater stopped working. The heater's maximum power is 0.30 W, and the safe working power is around 0.2761 W. Considering that the calibration measurement might take longer than 30 minutes, 0 - 0.2761 W was chosen as the power range to perform a sweep over, which corresponding to voltage applied across each heater is swept (0 - 2.35 V). The time needed for the calibration measurements is based on the step of applied power. A smaller step size can produce more accurate results to find the heater's ability to change

the phase by 1.5 π. However, this aspect of the experimentation could be removed once the electrical probes are more permanently bonded to the heaters.

During the calibration a DC signal generator is used to apply a DC electrical signal to the probes, then the optical chopper is switched on, and the lock-in amplifier is used in single channel mode to retrieve the amplitude of the modulated optical signal. The voltage applied across each heater is swept (0 - 2.35 V) and at each voltage combination the electrical currents and optical transmission are recorded, then power was calculated by multiplying the voltage and current of the heater to produce a transmission map like the one shown in figure 4.13 (a). Water is then flowed through the microfluidic channel, and the measurement is then repeated, producing a map as shown in figure 4.13 (b), and the difference in optical transmission is plotted in figure 4.13 (c). The "S" position is then determined by finding the power combination with maximum change in transmission (0.2761 W, 0.2761 W), "Z" is a point at which the transmission is low in both cases and there is very little change in transmission (0.2761 W, 0.0020 W), and "R" is a point with there is high transmission in both cases and there is the minimum change in transmission (0.0814 W, 0.0814 W). It can be seen that the overall shape of the transmission map in figure 4.13 which corresponds to the theoretical transmission map shown in figure 4.2 a.

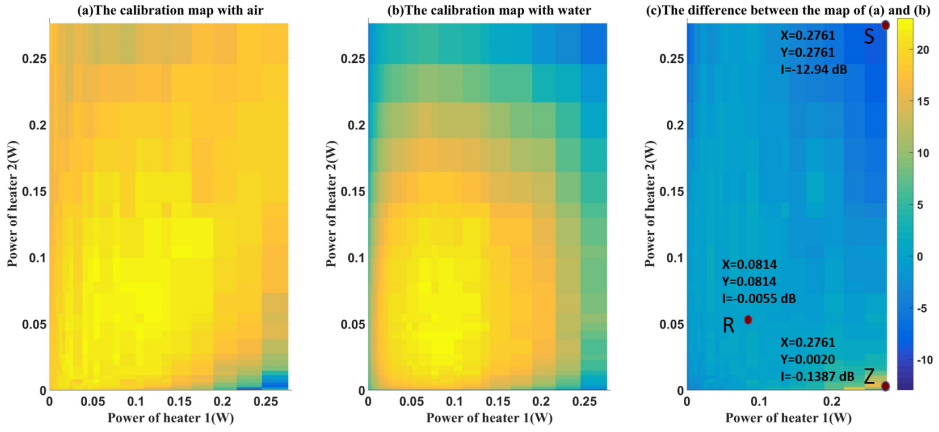

Figure 4.13: Experimental map of 2D transmission intensity for varying switch driving voltages (0 - 2.35 V), the plot shows the voltages covert to power (0 - 0.2761 W), the units of the colour scale is dB. (a) The calibration map with air, (b) The calibration map with water, (c) The difference between the calibration map with air and water over a full power period.

After finding the driving voltages of switch circuit required to tune to the "S","R", and "Z" operating points, a signal generator supplies waveforms with the shapes shown in figure 4.2 (b) and (c) to the thermo-optic phase shifters, where the voltages are chosen to correspond to the three operating points. The waveform is set up so that in time slot A the frequency $f_A = 6$ kHz (figure 4.2 (b)) and in time slot B the frequency $f_B = 7$ kHz (figure 4.2 (c)). The lock-in amplifier is then switched to dual channel mode so that

it retrieves the amplitudes of the optical transmissions at these two frequencies, where one corresponds to the measurement M_S and the other to the measurement M_R.

4.5.2 Time series measurements and stability performance of the switch sensor

Allan deviation measurement can be used as a method for analysing the noise and stability of the switch sensor [99]. When discussing the sensors used in this experiment, the switch sensor is the device fabricated in Chapter 4, which includes a integrated switching circuit. The waveguide sensors are the devices fabricated in Chapter 3. To compare the stability of the switch sensor and waveguide sensor, a time series of the transmission of the waveguide sensor over 47 minutes was measured with the laser on and recorded by a detector, as well as a time series of the transmittance of the sensing region of the switch sensor for the same length of time, both without an analyte present in the sensing region. Both time series were normalized to their mean values, and are plotted in figure 4.14 (a). During the measurement the time constant of the lock-in amplifier was set to 5 seconds.

As figure 4.14 (a) shows, qualitatively the normalized transmittance of the switch sensor (orange colour line) is flatter than that of the waveguide sensor (blue colour line), both in terms of high frequency fluctuations and in terms of long-term drift. The Allan deviation is a quantitative measure of the average deviation of the signal over varying time periods, and is shown for both of sets of time series data in figure 4.14 (b). It is evident that for all time periods, the deviation of the switch sensor is lower than for the waveguide sensor, and the minimum Allan deviations of the waveguide and switch are 2.1% and 0.2% respectively, showing that the switch sensor can reduce the minimum noise by a factor of 11.

Furthermore, from the Allan deviation results, for the waveguide sensor it can be seen that initially as the averaging time is increased to 10 s the deviation slightly increases, before reducing for a further increase to just over 100 s, when the deviation reaches a minimum. Beyond approximately 200 s the deviation increases, showing that drift of the signal becomes dominant, and preventing further noise reduction by averaging. On the other hand, for the switch sensor as the averaging time increases the deviation immediately decreases with a faster slope than the waveguide sensor until approximately 200 s, before also becoming dominated by drift for longer periods. This data shows that not only does the switch circuit reduce noise in the measured sensor transmittance, but it is also less susceptible to drift, which allows averaging to be used to even further reduce the noise.

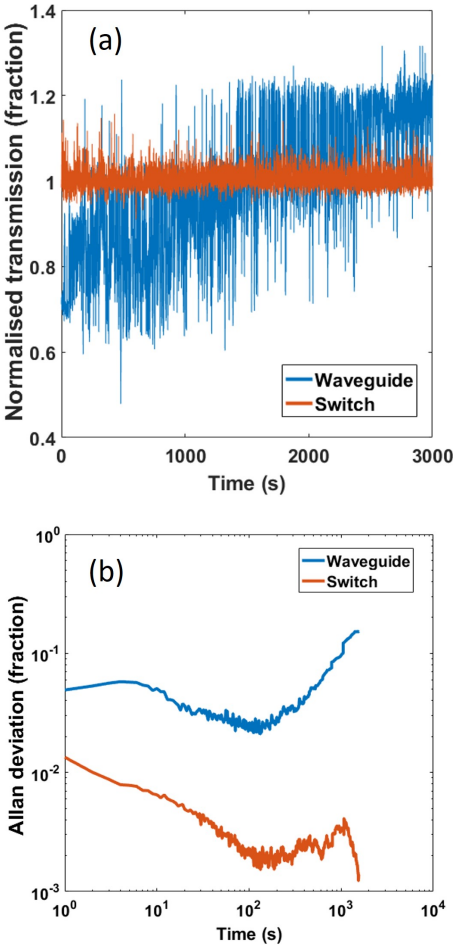

Figure 4.14: (a) Time series of the normalized transmissions of waveguide sensor and the calculated transmittance of the sensor arm of the switch sensor, (b) Allan deviation of the time series.

4.5.3 Sensing demonstration

4.5.3.1 Concentration series measurement of 2% IPA (by volume) in DI water sample with 1.8 mm interaction length switch sensor

After characterizing the noise properties of the sensor without an analyte, a test to see whether the switch is able to correctly measure the absorption of an analyte is performed, whilst at the same time reducing the noise of the measurement. The light from the sensing arm and the reference arm were measured, the extinction ratio of the sensing arm and reference arm were calculated as being E_{S0}= -2 dB and E_R= 13.12 dB. M_S, M_R, and T_a were measured using the switch over a period of 555 seconds with data points recorded every 0.2 seconds, and with the lock-in amplifier time constant set to 5 seconds. Figure 4.15 shows an example of the measured signals, for an experiment in which the switch sensing device is used to remove the noise and measure the normalized transmittance of the sensing arm and reference arm separately. There are 3 stages in this

measurement. The light was continuously switched between sensing arm and reference arm, and the computer was recording the signals at 6 kHz and 7 kHz measured by the lock-in amplifier.

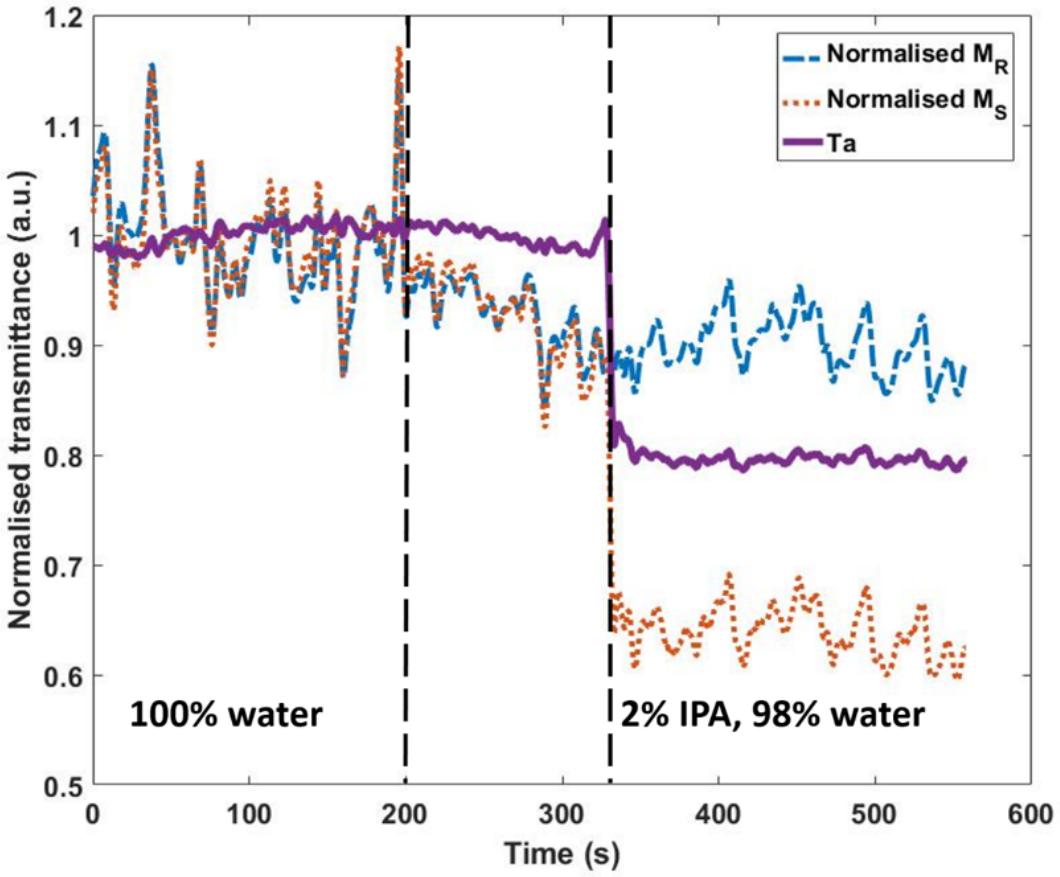

Figure 4.15: Time series measurement of transmission through the sensor arm (orange), the reference arm (blue), and the corrected relative transmittance of the analyte (purple) where each signal is simultaneously retrieved by the lock-in amplifier. The transmission in each arm is normalized to the mean of the water only transmission in that arm during this time series.

The first stage was from 0 - 200 seconds, during which there was DI water present in the microfluidic channel, and light was guided through the sensing arm and interacted with the DI water. The thermo-optic switch would switch it to the reference arm, with data being recorded from the sensing arm and the reference arm separately. From 200 - 330 seconds, a mixture of 2% IPA (by volume) and 98% DI water was pumped through the microfluidic channel until the mixture was in the microfluidic channel. Pumping of the mixture was then stopped, and data was recorded for the light output changing from the sensing arm and the reference arm. The third stage was the data from 330 - 555 seconds with the mixture remaining in the microfluidic channel, and the light interacting with the sample in the sensing arm waveguide only. The computer was recording the transmittance of the light from the sensing arm and the reference arm for this stage.

The data are plotted together in figure 4.15, each normalized to their mean values in the first period (where only water was in the sensing channel), so that their fractional changes can be directly compared. As the figure shows, there are three coloured lines which are blue (the normalized transmittance of reference arm), orange (the normalized transmission of sensing arm), and purple (the corrected relative transmittance of the analyte).

Initially, when only DI water flows through the microfluidic channel, the transmittance of the reference arm, sensor arm, and corrected relative transmittance each have a value close to 1. The transmittance of the reference arm and sensor arm follow very similar patterns to each other, but also quite noisy. However, the corrected sensor transmittance (purple line) is clearly less noisy than the normalised transmissions of the reference and sensor arms. This would be expected, since the M_S and M_R measurements would include similar noise in the optical input power to the switch, whereas that noise should largely be filtered from the T_a measurement. A simple waveguide sensor of the type in chapter 3 could be expected to have the same noise level as seen in the M_S and M_R measurements, since it would be equally susceptible to the optical input noise.

After approximately 330 seconds an IPA/water mixture flows through the device. A change in the transmission is seen for the sensing arm, because it interacts with the IPA/water solution, whereas the reference arm transmission remains unchanged. The value of the corrected sensor transmittance also changed with the transmission of the sensing arm, showing a change in the absorption of the sample at 3.77 μm wavelength with 1.8 mm interaction length of 0.99 dB. In chapter 3, a similar waveguide sensor was measured to have an absorption of 0.52 dB for a 1.9 mm interaction length, which is around 50% lower than measured using the switch sensor. The discrepancy could be caused by fabrication errors in the sensor region length or the waveguide dimensions in either experiment, causing an error in the assumed effective optical interaction length. However, there may indeed be an error in the absolute value of the absorption measured by the switch sensor that could be the result of calibrating the switch sensor to incorrect "S","R", and "Z" points. Such an error could be compensated for in an experimental setting by simply calibrating the sensor absorption using a sample with a known absorption value. The root mean square (r.m.s) of the T_a measurement before 200 seconds is 0.9%, while after 330 seconds is 1.3% of the normalized value, whereas for M_S it is 5.9% and 3.6% separately, showing that the switch reduced the noise by a factor of 7 times before 200 seconds and a factor of 2 times after 330 seconds in this measurement. A lower root mean square value would suggest data which has lower noise.

An SOI circuit with integrated thermo-optic switches and microfluidic channel has been demonstrated for use as a mid-infrared absorption sensor with reduced noise compared to a simple wave-guide absorption sensor. The circuit works by alternately measuring the relative sensor channel and reference channel transmissions, from which a change in absorption due to a liquid analyte can be observed. A calibration and measurement

scheme for using the device was proposed, and it was demonstrated by using it to measure the difference in absorption between 100% DI water and a solution of 2% IPA in 98% DI water. The results show that the switch sensor is able to lower the noise floor by a factor of 11 times compared to a simple waveguide sensor, which would ultimately allow the switch sensor to measure lower concentrations of a target analyte, to reach a lower limit of detection.

4.5.3.2 Current vs. time series measurement of the heaters on the switch sensor

Analysis of the results in this section suggest that the simple waveguide sensor's noise and drift is predominantly caused by variation of the input and output fiber positions, affecting the fiber-waveguide coupling efficiency. However, where does the remaining noise in the switch sensor measurement come from? There are a range of possibilities for the source of this noise, such as the contact of the electrical probes to the heaters, or even that the switch device does not act as quickly as predicted in our theory, and that there may in fact be a small time delay between measurements in each arm, meaning that not all of the noise is removed.

An experiment to analyse the noise occurring due to the contact of the probes was performed. Time series measurements of the currents passing through each of the switch heaters at constant voltage were taken. To do this, the input probes were placed on the input heater of the input switch, and the output probes contacted the output heater of the output switch. The DC power supply was set at 0.2 V, and the current was measured for 15 minutes. The current is measured by a Keithley 6487 picoammeter's current function which is connected to a computer via GPIB cables and the results are plotted on a normalised axis in figure 4.16. The input (blue markers) and output (orange markers) probes' current are changing over time and the output probes' current changes almost 3%, which might cause fluctuations in the phase change of the switch and influence the sensitivity of the sensor device.

Effectively this noise would manifest as a noise in the "S","R", and "Z" positions during the measurement, leading to varying errors in the absorption measurement. In a future experiment the susceptibility of the switch sensor to this noise source could be lessened by using a more mechanically stable method to electrically contact the heaters, for example by creating wire bonds between the heater contact pads and a driving PCB (printed circuit board).

Furthermore, the drift of the mechanical positions of the electrical probes meant that while performing the experiments, sometimes the voltages found to reach the "S","R",

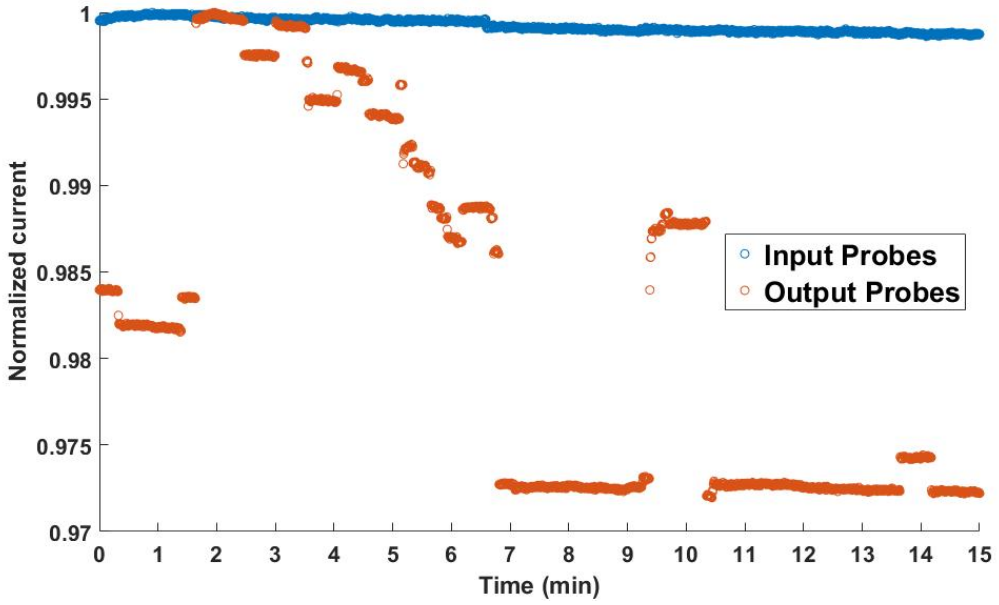

Figure 4.16: The current measurements of the electrical probes with heaters.

and "Z" positions during calibration would no longer be valid by the time the analyte measurement was performed, leading to inaccuracy in the calibration. Solving the mechanical issues would help to solve this issue too.

Beyond this, some of the remaining noise will come from the incorrect earlier assumption that the measurements of the transmissions through the sensor and reference waveguide are occurring simultaneously, when in fact there is a small time offset between the measurements, so that the common noise components do not cancel perfectly. The ultimate limit of the noise rejection improvement that can be achieved using this sensing scheme without the presence of significant electrical noise should be investigated in future work. The focus of this section is the switch device's ability reduce the noise. Time was therefore not spent on finding the limit of detection of this device. Due to the results shown in this section, it would be expected that the 2% IPA in DI water sample is not the lowest concentration detectable. In the future experiments, finding the limit of detection of the device would be of interest.

Chapter 5

Suspended Si with sub-wavelength grating and Ge-on-Si waveguides for sensing

5.1 Integration of suspended Si with sub-wavelength grating for liquid sensing for λ= 6 μm - 8.5 μm

For liquid sensing at longer wavelengths (λ= 6 μm - 8.5 μm) suspended Si waveguides with sub-wavelength gratings in the cladding can be integrated with microfluidic channels. The microfluidic channels are of the same design as Chapter 4 which is made by PDMS material. To bond the PDMS microfluidic channel, the device needs a SiO_2 cladding layer, which as observed in previous successful experiments, a 2 μm thick of cladding layer worked to bond the PDMS microfluidic channel effectively. However, the SiO_2 has strong absorption at this wavelength range. A protection cladding layer of ZnSe (zinc selenide) is therefore deposited between the suspended Si and the SiO_2 cladding. ZnSe has an almost zero absorption coefficient in this wavelength range meaning no further loss should occur due to absorption of this buffer material. The ZnSe protection layer is able to avoid the loss of SiO_2 cladding layer as the thickness of this layer should prevent any overlap of the guided light to the silica. Simulation results proved 2 μm thick ZnSe is sufficient to solve this issue.

Several substances (e.g. acetone, cocaine and heroin) have strong absorption peaks at this wavelength range [76]. The simulation, mask design and fabrication processes will be discussed in this chapter. Suspended Si waveguides with sub-wavelength grating claddings are explored because they can be made with a more mature fabrication process, and offer a more sensitive platform for sensing due to possibility to have a larger evanescent fields.

5.1.1 Simulations

The simulation of this design is based on figure 2.17, which was a low loss (3.1 ± 0.3 dB/cm) suspended silicon waveguide design (the principle of suspended silicon waveguides is discussed in 2.2.1.1) [55]. Figure 5.1 shows the cross section of the suspended Si with sub-wavelength grating. The height of Si-core layer which is 1.5 μm (h_2) instead of 1.4 μm, and the core waveguide width (w_1) is 2.9 μm wide. Additionally, this design has a top cladding of ZnSe 2 μm thick (h_3). The width (w_2) of the waveguide cladding (blue) is 3 μm.

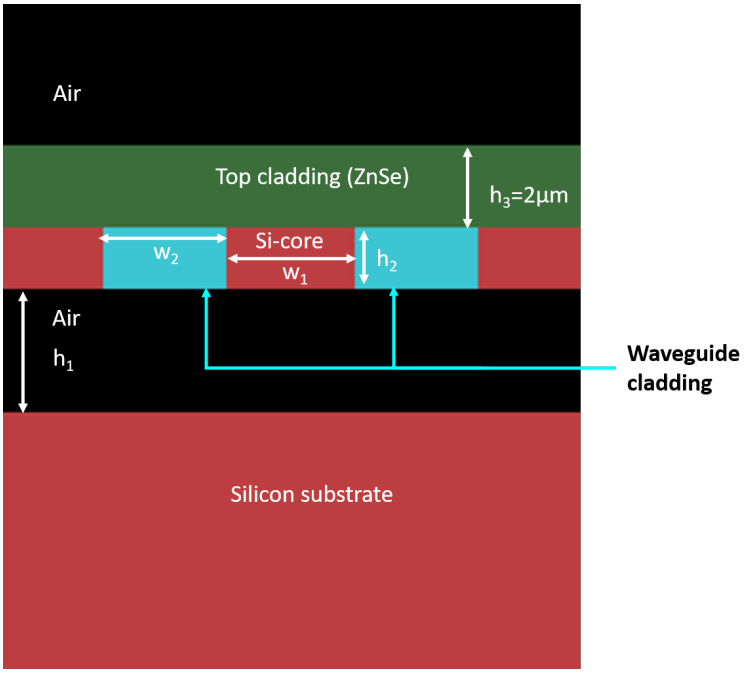

Figure 5.1: Simulation of a suspended Si waveguide with a sub-wavelength grating at 7.6 μm, with two holes (blue areas) covered with a cladding, and the waveguide covered with top layer zinc selenide (ZnSe) using literature data for the refractive index of ZnSe [100].

This simulation aims to check the loss of the suspended Si waveguide with a 2 μm thick layer of ZnSe at 7.6 μm wavelength. It is carried out using Lumerical MODE Solutions. The cross section of the waveguide is covered with a mesh. The meshing step lets the software use Maxwell's equations to analyse the mode profile of the light in a certain area [101]. If the size of the mesh is smaller, more points are calculated in the selected area, and the results will more accurate. However, it will cost more time, especially with large designs. Based on [102], the time of the simulation scales inversely to the mesh resolution cubed. In the simulations used for the experiments in this section, the mesh resolution setting is 0.05 μm. If the mesh resolution setting is reduced to 0.01 μm, using the relationship from [102] the simulation time would be 125 times slower.

The boundary condition of the simulated area is PML (Perfectly Matched Layer) which is a condition that essentially absorbs the light to reduce the reflection of the light at the

outermost interface. The optical properties of the Si material came from the Lumerial material library [103] and for the waveguide cladding the refractive index is given a value of 1.72, as per [55].

The ZnSe refractive index (n,k) data was taken from [100]. The refractive index of ZnSe is around 2.4 and the extinction coefficient can be considered as constant and close to zero at the wavelength range of 6 - 10 μm (actual value of k is 9 $\times 10^{-7}$) [100]. The layer between the Si-core and silicon substrate was a silica layer, which was 3 μm thick (h1). Since the silica layer has a high absorption at a wavelength of 7.6 μm [40], it has been removed. This structure is good for sensing applications, because there is more light than a strip structure waveguide in the air surrounding the core as it can be seen in figure 5.2(a), which leads to is higher light-analyte interaction.

Figure 5.2(a) shows the TE mode profile of the suspended Si core at 7.6 μm, as the simulation showed that the TM mode was not supported in this design. The results show that 18% of light is in air. The simulation shows a loss of the TE mode of 2.24 dB/cm. The loss come from the Si substrate's absorption, because the Si increased the absorption around 8 μm [52].

Between the wavelength range of 6 μm and 10 μm, the loss of the TE mode as a function of the wavelength was also investigated, which is plotted in figure 5.2(b). As figure 5.2(b) shows, the blue and orange lines are the loss of TE mode of the suspended Si waveguide with a ZnSe cladding layer and without a cladding layer. The blue line is showing the same trend as the orange line, however, the loss of suspended Si waveguide is slightly higher than the loss of the waveguide with the cladding layer. This is likely due to the Si having a high absorption after a wavelength of 8 μm. When the ZnSe is placed on the top of the suspended Si waveguide, the TE mode is less confined in the Si layer and that causes the loss to be reduced after a wavelength of 8 μm.

A simulation of the 2 μm thick SiO_2 cladding layer on the top of the ZnSe was also performed. The result showed that the extra silica layer did not change the loss, with the spectra being hard to distinguish from the spectra with just the ZnSe cladding layer show in figure 5.2(b). This would suggest the 2 μm thick ZnSe cladding layer ensures the light is not absorbed by SiO_2 cladding layer. The simulation results suggest the loss at the 6 - 8.5 μm wavelength range is acceptable, at about 2 dB/cm.

5.1.2 Mask design

The suspended Si waveguide can operate at longer wavelengths because the SiO_2 bottom cladding is removed. A 1.5 μm thick SOI suspended waveguide was designed with grating couplers at input and output for an initial test run. If it can operate at 7.6 μm wavelength, then a ZnSe cladding layer will be deposited later which can be used to create sensing windows and can also avoid absorption of PDMS at longer wavelengths.

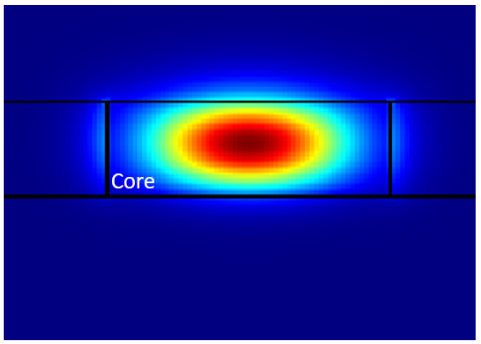

(a)

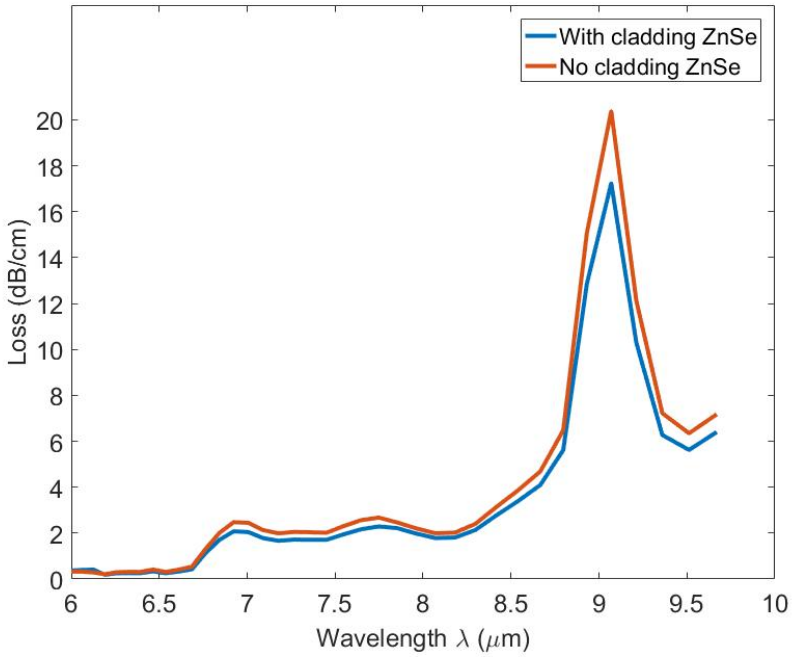

(b)

Figure 5.2: (a) Simulation of the TE mode profile of a suspended Si waveguide at 7.6 μm, (b) Simulated loss of the suspended Si waveguide in the wavelength range of 6 - 10 μm where zinc selenide (ZnSe) is deposited on top of the cladding (blue line), and a suspended Si waveguide without a cladding layer (orange line).

After obtaining the design of the waveguide, the mask design needs to be described. There are three sections: the sensing section (figure 5.3 (a)), the cutback loss section and the bend loss section (figure 5.3 (b)). As figure 5.3 (a) shows the three elements that constitute the sensing part are the straight waveguides (region highlighted with green) where the waveguides are under etched with HF, the walls (the section between the purple and green highlighted regions) are not etched with HF, and the sensing window (purple highlighted region). The width of the wall is 100 μm. As the HF etches isotropically, this thickness should ensure the HF does not etch away all of this wall. If

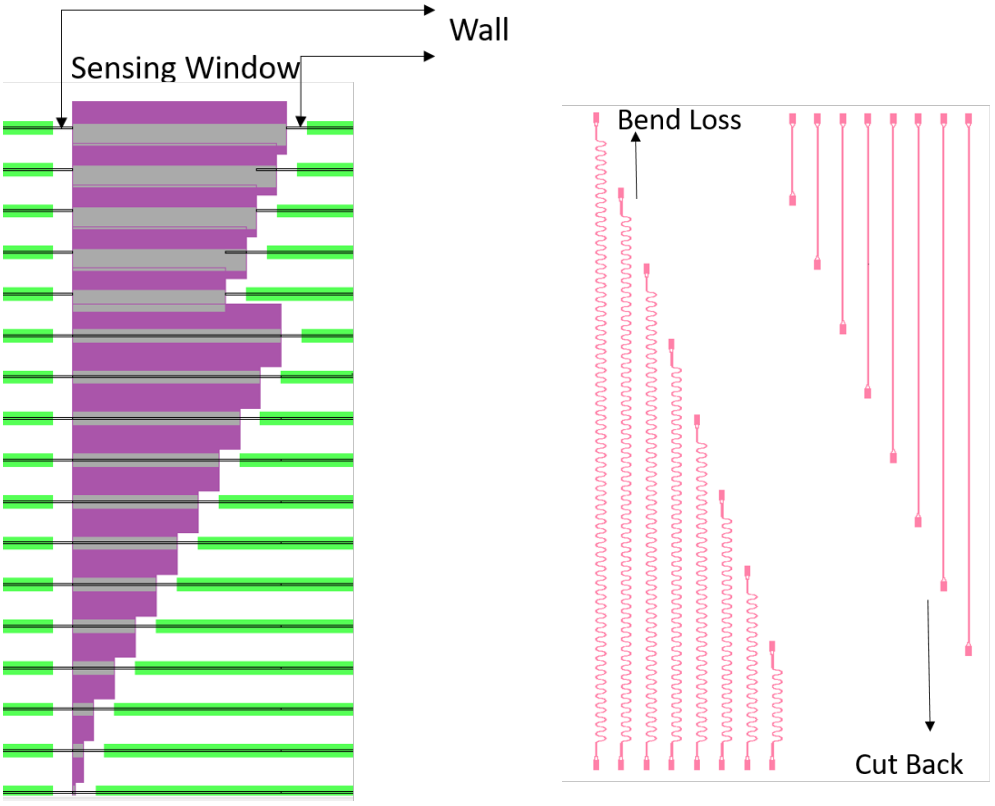

Figure 5.3: Suspended waveguide mask design. a) The sensing section with sensing window and walls. b) The bend loss and cut back section.

the wall is fully etched, the analyte will not be contained in the sensing window area, and the analyte will spread underneath without control.

Sensing window lengths from 10 μm to 1000 μm were designed using straight waveguides (figure 5.4 (a)). To make sensing lengths of 1.1 mm to 1.54 mm, bend waveguides (figure 5.4(b)) were used to fit the longer lengths into the 1 mm wide sensing region. Between sensing window and straight waveguide, there are two 100 μm thick walls which should theoretically be able to avoid leakage of the liquid underneath the waveguide along its length.

The cutback loss section and bend loss section (figure 5.3 (b)) are included for testing the waveguide propagation loss and the bend loss. Future work will include the use of the cut back method to measure the waveguide propagation loss. The loss coefficient (α) can be calculated using equation 5.1 for two lengths of the waveguide L_0 and L_1, the output intensity of the waveguide is I_1 and will be different for each waveguide, as the length of each waveguide is different. We assume the input intensity is the same which is I_0.

$$\alpha(dB/cm) = 10 * (\frac{1}{L_0 - L_1}) \log_{10}(\frac{I_1}{I_0}) \tag{5.1}$$

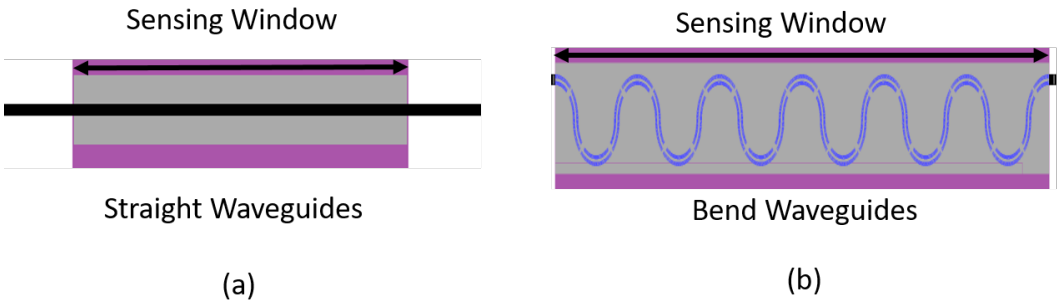

Figure 5.4: A schematic description of how the suspended waveguide masks fit into the sensing window. There are two designs. (a) shows how a straight waveguide looks, with light propagating through the black region in the centre of the device. (b) shows a bend waveguide, where light propagates through the blue region of the waveguide. For sensing windows of the same length, the bend waveguide is able to achieve a higher interaction length.

The input light for all waveguides is the same which is P_0, the output P of different waveguides are different due to different number of bends (Δn). Hence the bend loss ($Loss(dB/90^0)$) can be calculated using equation 5.2.

$$Loss(dB/90^o) = \frac{10 * \log_{10}(\frac{P}{P_0})}{\Delta n} \tag{5.2}$$

5.1.3 Fabrication

For the fabrication of the 1.5 μm thick suspended Si waveguides, a SOI wafer is used as the starting point (see figure 5.5 (a)). S1813 photoresist is then spun onto the wafer for protection, then it is diced into chips. Acetone, IPA and DI water are used to remove S1813. 900 nm thick ZEP photoresist is then coated onto the wafer before patterning by e-beam, and then the chip is fully etched (1.5 μm) by an Oxford Instruments ICP 380 system to make the holes through the Si layer (see figure 5.5 (b)). The holes allow HF to come underneath to remove the 3 μm SiO_2 bottom cladding (see figure 5.5 (c)), and at the same time, the stops are kept. This part of the fabrication process has been completed. The next process that will be done on these chips is to test their guidance quality, however, this work has been paused due to the outbreak of COVID-19. This caused the lab closure for almost 4 months, from 16/03/2020-07/08/2020. The chip could therefore not be measured in the lab.

Once the guidance quality of the chips can be verified, the fabrication process can continue. This will involve 2 μm PMMA will be spun onto the wafer, and e-beam patterning will be used to define windows for HF etching, which will determine which parts of the waveguide are under etched, and where walls are created underneath the waveguide. Next, the cladding layer of ZnSe will be deposited (figure 5.5 (d)), followed

by deposition of 2 μm thick SiO_2 cladding layer (figure 5.5 (e)) on which the PDMS microfluidic channel can be bonded to later. Finally, e-beam lithography will be used for the third patterning step to define different interaction length sensing windows, and then the ICP will be used to etch the sensing windows (figure 5.5 (f)).

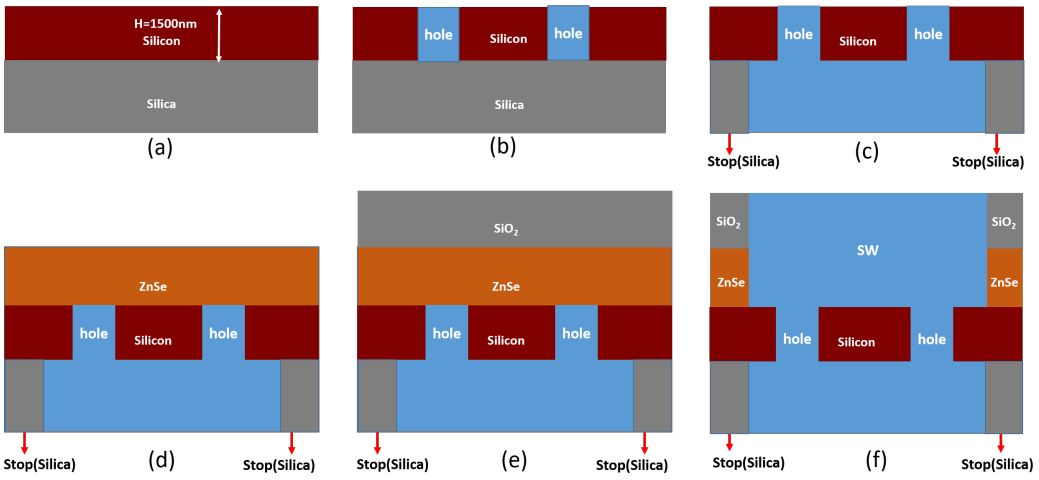

Figure 5.5: The fabrication process of the suspended Si with sub-wavelength waveguide with two silica stops, 2 μm thick ZnSe cladding layer, 2 μm thick SiO_2 cladding layer with a sensing window.

For the work discussed in this section, the simulation of the waveguide, the mask design of the suspended Si waveguide with sensing windows of varying lengths and structure, and a part of the fabrication of the chip has been achieved. However, due to the time constraints of the project and lab unavailability caused by the outbreak of the COVID-19 virus, the testing of the chip could not be completed. It is expected that this chip will be able to detect acetone in a host solvent using a wavelength range between 6 μm - 8.5 μm, which the future work of this project will revolve around.

5.2 Integration of Ge-on-Si waveguide for λ= 7 μm - 10 μm with microfluidics

Ge-on-Si waveguides are attractive because they have a very wide transmission range, which means they can work with samples with absorption features at very different wavelengths. In this chapter, the simulation of Ge-on-Si waveguides with Lumerical MODE Solutions will be described, as well as the fabrication process.

5.2.1 Simulation

In this part of the project, a Ge-on-Si rib waveguide was designed and simulated by Lumerical MODE Solutions with a script presented in the Appendix. At 7.6 μm wavelength, in order to both increase the overlap between the mode and an analyte, and to avoid mode substrate leakage from Ge to Si, the platform was chosen to have a height (H) of 2 μm germanium on silicon. Based on simulations results, the etch depth should be h = 1.75 μm and the rib width W = 3.8 μm. The mode confinement is 98.4%, which is calculated by Lumerical. Figures 5.6 (a) and (b) show the cross section of the waveguide and simulated TE and TM mode profile at 7.6 μm wavelength. The simulation results shows both TE and TM mode are supported, and the loss of this waveguide design is about 0.1 dB/cm, which is due to the absorption of Si at 7.6 μm.

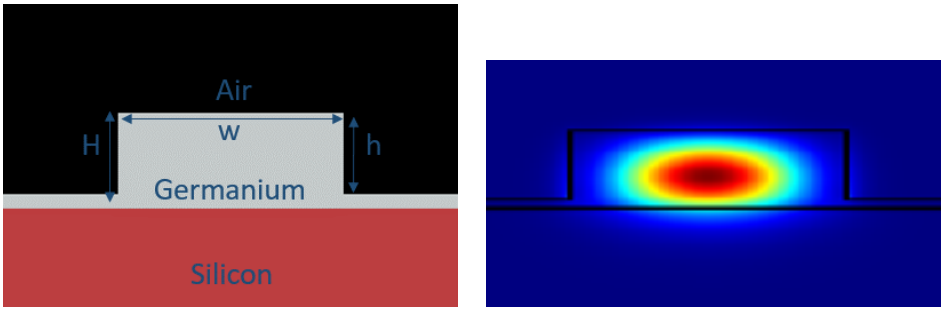

(a) (b)

Figure 5.6: The design of the Ge rib waveguide. (a) A diagram of the Ge rib waveguide cross-section with W= 3.8 μm, H= 2 μm, and an etch depth of rib waveguide h= 1.75 μm. (b) Simulated TE and TM mode profile at λ= 7.6 μm.

Considering the mode confinement of these waveguides and based on the Beer-Lambert law, for the case of an ideal waveguide with negligible loss, the longer interaction length will achieve higher sensitivity for chemical sensing [104]. The spiral structure was used to extend the optical path length and to reduce the device footprint in this mask design. Seven different lengths of spiral waveguides were designed in this project. The bend radius and bend loss were calculated and the results plotted by Matlab. Considering the bend loss and dimensions of the chip, 76.6 μm of bend radius was chosen, because this bend radius was simulated to give a negligible loss of 6×10^{-4}dB/90°.

5.2.2 Mask Design

The chip was divided in three parts: the cutback section, the normalisation section and the spiral waveguide section. Before the fabrication, the mask was required and it is designed by L-edit with C++ functions. The width of this mask is 15 mm, the height is 20 mm.

As figure 5.7 shows, there are seven different spirals with the same inner bend radius of 76.6 μm. The width of the spiral waveguide is 3.8 μm. Each design in the spiral waveguide section is a butt-coupling rib waveguide, and it consists of input and output tapers, bends, straight waveguides and spiral waveguides. The total length of the tapers, bends and the straight waveguide features are 23.5 mm. Each design has different lengths of the spiral waveguide; they are 1625 μm, 3000 μm, 4570 μm, 6205 μm, 8000 μm and 9799 μm. The reason this design uses bends is to make the output and input port not in line with one another. This is to ensure that during measurement, any output light collected at the waveguide facet is guided by waveguide, rather than directly transmitted from the input source.

The normalization section is used to measure the insertion loss of the spiral waveguides. The spiral waveguide section is used as the sensing part and the cutback section is used to measure the propagation loss of the waveguide. The end facets of the fabricated chip will be polished, then the butt-coupling setup will be used to measure it.

5.2.3 Fabrication

This fabrication of the Ge-on-Si chip was carried out in the Southampton Nanofabrication Centre.

Before fabrication, the chip was cleaned using Acetone, IPA, and DI water. After the cleaning, the chip was spun with ZEP photoresist, then baked on a hotplate for 2 minutes. The next step was to spin e-spacer to avoid charging effects during e-beam lithography. The chip was then patterned using e-beam lithography.

This chip was etched in the Oxford Instruments ICP 380 system. The etch time was based on the etch depth and material. The etch depth was 1.75 μm. The photoresist was removed with an O_2 plasma asher.

As the chip is designed for butt-coupling at the chip facets, the next step is dicing with S1813 photoresist covering the chip to minimize potential damage. After the dicing, this chip will be cleaned by acetone for 10 minutes in an ultrasonic bath and then with IPA.

As with the work in the previous section 5.1, the fabrication of the chip was completed, however it has not yet been able to be tested on. Like the work in the previous section, acetone in a host solvent will be used for sensing. The results of section 5.1 and 5.2 will then be compared to find the optimum waveguide design for a wavelength of 7.6 μm. To date, this work has not been completed, and will be an interesting direction for the future of this project.

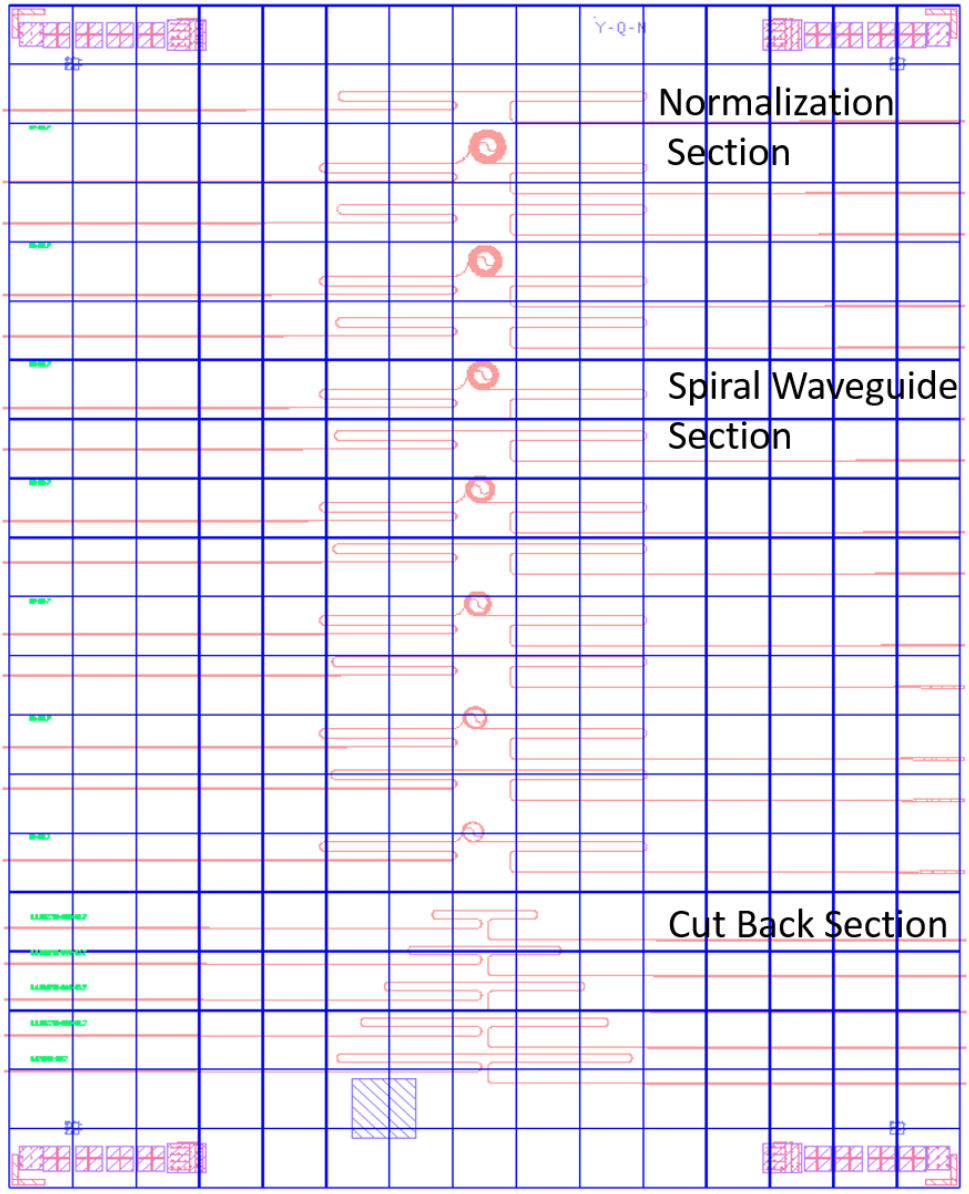

Figure 5.7: The Ge-on-si rib waveguide mask layout.

Chapter 6

Conclusions and Future Work

The projects described in this thesis focus on the development of SOI waveguide circuits that can be used for the detection of liquid analytes. By operating in the MIR wavelength range, the fingerprint absorption of an analyte can be used to locate the presence of certain molecules and the subsequent absorption changes can be used to find the concentration of a sample. It is envisaged that such a device could have applications in the medical sector, for use in drug testing of blood samples.

The conclusion section summarises the work performed in the project: the integration of a SOI rib waveguide with a microfluidic channel to detect the spectra of IPA, the integrated switching circuit on Si waveguide to improve the sensitivity of IPA detection, and the design and fabrication process of suspended Si and Ge-on-Si waveguides.

The future work section presents ideas for improvements of the integrated switches on a Si, and descriptions of the future analysis and improvements of a suspended Si and Ge-on-Si waveguides.

6.1 Conclusions

6.1.1 Development of a SOI rib waveguide with microfluidic channel

The initial experiments were based on a SOI rib waveguide structure. After a thorough literature review on MIR sensors, it was decided that an SOI device would work best, due to its low loss ($\sim$ <2 dB/cm) and the mature fabrication technology available. To calculate the optimum dimensions for such a waveguide, Lumerical Mode Solutions software was used to simulate the device, and to calculate the guidance properties of the contained mode. This was found to be a design with a 1.3 μm width and a height of 450 nm, made from pure silicon. The calculated TE mode overlap was around 10.6% of the light in air surrounding the Si core. The chip's mask design was created in L-edit with

C++ code, and different interaction lengths (10 μm -3 mm) were created, in order to determine an optimum length for sensing. SiO_2 was deposited on the waveguide surface as a cladding layer which was used for bonding a PDMS microfluidic channel and etching the sensing windows.

A PDMS microfluidic channel was selected to be integrated with the device to act as the host for the liquid analyte. This was chosen as it would not lead to liquid evaporation whilst detecting, which would affect our results. The microfluidic channel enabled a variety of benefits, such as the capability to guide liquids to the sensing area and the ability to clean the chip with ease. The microfluidic channel was fabricated at the University of Southampton's Nanofabrication Centre, in which Solidworks was used to design the microfluidic mould, which a 3D printer was able to realise.

Using the SOI rib waveguide chip, demonstration of IPA in DI water sensing which includes sensitivity measurements and spectra measurements were achieved. The absorption spectra of pure IPA on SOI rib waveguides with a variety of interaction lengths (of 150 μm, 190 μm, 240 μm, 340 μm, and 640 μm) was achieved. This was performed using a tunable QCL. The absorption peak of IPA at 3.77 μm wavelength was measured which agrees with the simulation results.

As a reference for assessing the quality of the sensing device, results from [23] are used as a comparison. They were able to detect a concentration of 5% IPA in DI water with an interaction length of 4.02 mm. The characterisation of SOI waveguide device aimed to improve on this value, looking for smaller concentrations at lower interaction lengths. Results presented in this thesis show the limit of detection of SOI rib waveguide sensor is 1.5% with a 1893 μm interaction length. To achieve this, a SOI rib waveguide sensor was integrated with a microfluidic channel, with a syringe system, an external light source, and an external detector was used. Further testing at other interaction lengths of 150 μm, and 640 μm found concentrations of 5%, and 3% of IPA in DI water respectively. This was possible due to the low loss waveguide, and the PDMS microfluidics channel helped to avoid the IPA evaporation.

The most obvious limitation in these experiments is that the input and output fibers contributed to the background noise, which influences the sensitivity of the measurements. The aim of the next work was to lower the noise floor of a SOI waveguide evanescent absorption sensor by integrating a pair of switches into the circuit, so that the circuit switches the light between a sensor waveguide and a reference waveguide at a rate of a few kHz. If this switching frequency is higher than the noise frequency, measuring the relative transmission of the two arms in two successive measurements can help to reduce the noise of the measurement.

6.1.2 Integrated switching circuit for low-noise self-referenced mid-infrared absorption sensing using silicon waveguides

The drift of the input and output fibres introducing noise led to the next aspect of the project: the integration of an input switch and an output switch into the Si waveguides with microfluidics channel to reduce the noise floor. By reducing the noise, the sensitivity of the device could be increased due to information not being hidden behind unpredictable data points. The switch circuit includes one input switch, one output switch, a reference channel and a sensor channel. The switch circuit worked by essentially producing two channels, a reference channel and a sensor channel which when compared with one another could show the change in absorption. By switching between the two channels at a frequency higher than that of the noise, the data would be unaffected by aspects such as fibre drift.

The theory of the thermo-optic switch circuit design is based on S-matrices which is used to describe the relationships between the electric fields at the input and output port. The theoretical calculation supports the concept of the switch being used to reduce the noise. The mask design has a variety of elements of the switch circuit, and the idea behind this is to help diagnose problems with the switch circuit should issues arise. The chip used an ICP etcher to remove 450 nm of Si to produce the rib waveguide. 2μm thick silica was deposited on the top of the SOI waveguides as a cladding layer. 150 nm of aluminium was then deposited as the heater on the switches. The chip was bonded with a PDMS microfluidic channel at the end.

A series of experiments were performed to characterise the new chip, and ultimately to show the sensing capabilities of the new design. They were split into calibration measurements of the heaters, stability performance measurements and sensing measurements.

The calibration measurement obtained the driving powers of the two heaters in input and output switches. For maximum transmission of the light to travel through the sensor arm, the power generator should supply 276.1 mW to both the input and output switches. For the light to be switched to the reference waveguide, the input and output switches need 81.4 mW each. This standard was maintained through the following experiments.

A stability performance experiment was performed on both the rib waveguide chip and the switch integrated waveguide. In these tests, light was allowed to propagate through the waveguides, and the output of the two designs was measured over a period of 47 minutes. The results were then compared. It was found that the integration of the switch produced less inherent noise than that of the rib waveguide. The Allan Deviation was calculated on each device, and it was found that the switch integrated waveguide had an order of magnitude lower value. The switching sensor was able to reduce the

noise floor by a factor of 11 times compared to the simple waveguide absorption sensor. This would suggest the switch integrated waveguide operates better by removing the noise for both high frequency and low frequency components. The performance of this switch circuit could be improved, the details are described in the future work section.

The initial results were able to show sensitivity measurements of 2% IPA in DI water for an interaction length of 1.8 mm. The results showed the reference arm and sensor arm operating in synchronisation, suggesting the switch operated effectively.

6.1.3 The design and fabrication process of suspended SOI waveguide and Ge-on-Si waveguides

Other work presented in the thesis focused on the challenging longer wavelength range, in which a suspended SOI waveguide was first used for 6 μm - 8.5 μm wavelength range. This wavelength was selected as it can be used to detect other analytes such as chemical liquid acetone, or drugs like cocaine and heroin. The difficult part is the fabrication processing to build two buried oxide walls to avoid liquid leakage. The chip design was carried out with Lumerical Mode Solutions and L-edit.

The purpose of the design of the suspended Si with sub-wavelength grating waveguide for liquid sensing measurement is to remove the absorptive silica layer. This will allow for the Si platform being able to operate at the wavelength range of 6 μm - 8.5 μm which is proved by the simulation of the suspended Si waveguide. The simulation shows that the loss is about 2 dB/cm and 82% of the light is confined in the waveguide. 18% of the light is in the air which should allow for sufficient interaction with the analyte.

The simulation results of the loss spectrum of the ZnSe cladding layer and silica cladding layer shows that the 2 μm thick ZnSe is thick enough to avoid the light interacting with the silica cladding layer. The ZnSe absorption coefficient is close to zero at the wavelength range of 6 μm -8.5 μm, which theoretically means the ZnSe as a cladding layer does not increase the loss.

The mask was designed so that the two stops (ie silica walls) underneath the waveguide can avoid leakage of the analytes. Another aspect of this mask design is that it can used for bend waveguides for longer interaction lengths to save space but still achieve high sensitivity.

In the fabrication process, the chip was initially patterned with photoresist. It was then etched with an ICP dry etching tool to open the holes on the Si layer. These holes allow the HF to go into the BOX layer to remove the silica and create the silica walls (stops). By controlling the timing of the etch, it can be ensured that the silica walls (stops) are not over etched. After this part of the fabrication process was complete, a microscope check was performed to check the quality of the design. This can be seen in

figure 6.1. The testing the waveguide quality of this chip has not started yet. This is due to limitations of the laboratory time and the effects of the COVID-19 virus.

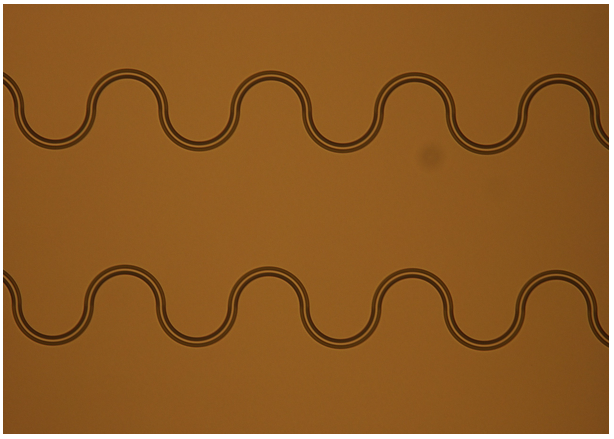

Figure 6.1: A microscope image of two of the suspended bend waveguides after HF etching.

When the testing of the chips is able to be completed, the next steps for the fabrication of this chip are to deposit 2 μm ZnSe on the top of the suspended Si waveguide, and then the 2 μm silica cladding layer will be deposited on the top of the ZnSe layer. The ZnSe is used to stop the light interacting with the silica cladding layer. The silica cladding layer is used to bonding the microfluidic channel later on in the fabrication process.

Another method of being able to detect at longer wavelength ranges is to change materials. Using Ge-on-Si waveguides due to Germanium's inherent low loss at longer wavelengths (7 μm - 10 μm), sensing at such wavelengths should be capable. The dimensions of the Ge rib waveguide is a width of 3.8 μm, etch depth of the rib waveguide of 1.75 μm, and the Ge layer thickness is 2 μm. This design supports TE and TM polarization and 98% of the light is confined in the Ge rib waveguide at a wavelength of 7.6 μm. The simulated loss is as low as 0.1 dB/cm. To test the experimental possibilities of such a design, for the mask design, there are seven different lengths of spiral waveguides which are between 1600 μm to 9800 μm. Each waveguide has a corresponding normalization waveguide, whereby the spiral is replaced with a straight waveguide. This allows for the loss of the spiral to be calculated. The fabrication of the Ge rib waveguide has been carried out. The Ge layer thickness is 2 μm, and the etch depth is 1.75 μm of the rib waveguide which is made by using an Oxford Instruments ICP 380 tool. The Ge on Si chips have been fabricated, and are currently awaiting characterisation. This work has been delayed due to issues regarding laboratory access which is restricted by the limitations in place caused by the COVID-19 virus.

6.2 Future work

6.2.1 Improvement of the integrated switches on Si waveguide

There are suggestions on how the sensitivity of switch circuit's measurements can be improved. One such method of achieving this could be creating wire bonds between the heater contact pads and a driving printed circuit board. That means their vibrations will not introduce additional noise. The current set up uses electrical probes that are held in place to the heaters by force, which is not particularly stable and could be influenced by vibrations to the setup. Another option is to replace the Al with a different metal contact that does not react with oxygen and can withstand high temperatures that may occur due to long measurement times.

Furthermore, for the 3.725 μm - 3.888 μm wavelength region, the liquid-liquid extraction could be used to move the analyte to a lower absorption solvent. For example, most organic solvents have lower MIR absorption than water so extraction would allow a lower limit of detection when the sample is characterised using the waveguide sensor [105]. This is particularly relevant to clinical analysis as biological samples are typically aqueous.

A modified version of the silicon waveguides integrated with microfluidics for mid-infrared evanescent absorption spectroscopy (chapter 3) will in future be used to detect clinically relevant analytes such as lipids, proteins and drugs (aspirin and paracetamol) in the 3.3 μm wavelength range.

6.2.2 Developments of suspended SOI waveguide and Ge-on-Si waveguides

For the longer wavelength region (7 μm -10 μm), suspended SOI waveguide and Ge-on-Si spiral waveguides will be used to measure acetone as an analyte with carbon tetrachloride as a solvent. Because acetone has an absorption peak at this wavelength range, acetone can be used as a test sample to qualify the performance of the waveguide. As it is an abundant solvent, it is cheap and easy to obtain. If the test is successful, the suspended SOI waveguide and Ge-on-Si spiral waveguides are able to be tested with more challenging analytes, such as cocaine.

Considering chemical reactions between analytes and waveguides, a capping material will be considered for cladding the waveguides to protect them. For example, SiO_2 and ZnSe will be used for shorter and longer wavelengths, respectively. The sensitivity of acetone in carbon tetrachloride measurements on these waveguides with integrated microfluidics will also be tested. As mentioned in Chapter 6, the challenging part of the suspended SOI waveguide needs to consider the leakage of analytes, and high loss from

silica. To avoid the leakage, the mask design will be improved, adding more dimensions of the separation of the buried oxide walls, which can balance the low loss and leakage problems.

6.2.3 Longer term objectives

The long term aims of the project are to be able to use the device in real world applications. Therefore the detection of analytes such as paracetamol are key. This would require the longer wavelength MIR testing, likely to be used with a Ge-on-Si waveguide. As yet, this type of waveguide has not been integrated with a switch circuit which has been proven to lower the noise floor of said device, and would hopefully allow for high sensitivity measurements to be made. The device would also benefit from a wider broadband guidance capability, so the possibility of multiple analytes can be performed in a single measurement. For this to become a reality, some components, such as the switch and the low loss waveguide would require further research to ensure the device functions at a wider wavelength range. A major development of the sensing waveguide would be the integration of other components, such as detectors, lasers and power sources, to create a pure lab-on-chip device. This would heavily decrease the footprint of the device, and allow for example bed-side measurements of patients, with rapid results, meaning prompt diagnosis can be made, possibly saving lives.

A further avenue for exploration is the use of the chip for gas sensing. By filling the microfluidic channel with gas, it would be of interest to see how the device performs, and how well encapsulated the channel is. Such a chip could allow for small, cheap devices to quickly warn of hazardous material.

6.2.4 Description of work complected by the author

Here is a description of the work undertaken by the author in the process of this project. In each chapter, the work that the author has completed is described.

Chapter 3:
1. Design and simulation of the SOI rib waveguide.
2. Mask design of the chip.
3. Fabrication of the chips and microfluidics channel.
4. Building of the setup of the SOI rib waveguide sensing system.
5. All measurements of waveguide loss and sensing measurements, and data analysis.

Chapter 4:
1. Theoretical sensing design with Dr. Milos Nedeljkovic's help.
2. Mask design of the chip.

3. Fabrication of the chips and microfluidics channel.
4. Building of the setup of the switch sensing system.
5. All measurements of waveguide loss and sensing measurements, and data analysis.

Chapter 5:

1. Design and simulation of the suspended SOI waveguide and Ge waveguide for sensing.
2. Mask design of the chip.
3. Fabrication of the chips.

Appendix A

Appendix

A.1 Preliminary measurements using filter paper, and calculating the length of the sensing windows

In this experiment 0.05 cm wide filter paper was used to apply pure IPA to the chip surface, in a similar way to that described in the thesis of Dr. Mittal [106]. The pure IPA is dropped on the filter paper, which is then placed on the surface of SOI with sub-wavelength grating waveguides. When this is carried out, the output signal from a detector measuring waveguide transmission is reduced from 1V to 0.1 mV at 3.8 μm. The loss (in dB) of pure IPA at 3.8 μm wavelength is then calculated to be 40 dB (see equation A.1).

$$Loss(dB) = -10 * log_{10}\frac{10^{-4}\ V}{1\ V} = 40\ dB \tag{A.1}$$

Got the loss of pure IPA and known the width of filter paper is 0.05 cm ((interaction length), which can calculate the attenuation coefficient (attenuation per cm) of pure IPA (in dB/cm) is presented by A, see equation A.2.

$$A(dB/cm) = \frac{Loss\ (40\ dB)}{0.05\ cm} = 800\ dB/cm \tag{A.2}$$

If the target of loss is 10 dB, then the interaction length (L) should 0.0125 cm (125 μm), see equation A.3.

$$L(cm) = \frac{Loss\ (10\ dB)}{A(800\ dB/cm)} = 0.0125\ cm \tag{A.3}$$

As same process of pure IPA, I repeated this process with pure water, got the output signal changed from 0.59 V to 0.512 V, after calculated with equation 3.1-3.3, the interaction length should 1200 μm. Considering this mask design will be used for identifying

water and IPA spectra and the concentrations of water-IPA mixture solutions, dosing 10um to 2 cm interaction length in this mask which include 100 um, 1200 um and 0.05 cm interaction length.

A.2 Lumerical simulation rib spiral waveguide (Ge-on-Si)

```
deleteall;
selectall;
delete;
# The cross-section of Ge-on-Si rib spiral waveguide
# Define structure
l=10e-6; #length of substrate
w=100e-6; #width of substrate
h1=10e-6; #height of substrate
h2=2e-6; #etch of rib waveguide
D=1.7e-6;
wg=3.8e-6;# width of rib



# Define Materials

wg_material= 'Ge (Germanium) - Palik'; # material of rib
sub_material = 'Si (Silicon) - Palik'; # material of substrate


#Draw Waveguide Ge-on-Si
deleteall;
selectall;
delete;

addrect;
set('name','rib');
set('z',0);
set('z span',l);
set('x',0);
set('x span',wg);
set('y max',D);
set('y min',0);
set('material',wg_material);

addrect;
set('name','wg');
set('z',0);
set('z span',l);
set('x',0);
set('x span',w);
set('y max',0);
set('y min',-h2+D);
set('material',wg_material);

addrect;
set('name','sub');
set('z',0);
set('z span',l);
```

```
set('x',0);
set('x span',w);
set('y max',-h2+D);
set('y min',-h2-h1+D);
set('material',sub_material);


# define simulation patameterd
wavelength=7.6e-6;
meshsize=0.1e-6;


# set general solver type
addfde;
set('solver type','2D Z normal');


# set geometry-center posiiton of the simulation region
set('x',0);
set('x span',16e-6);
set('y',h2/2);
set('y span',16e-6);

# mesh seting
set('define x mesh by', 'maximum mesh step');set('dx', 0.1e-6);
set('define y mesh by', 'maximum mesh step');set('dy', 0.1e-6);
set('min mesh step', 0.01e-6);

# set boundary conditions
set('x min bc','PML');
set('x max bc','PML');
set('y min bc','PML');
set('y max bc','PML');
set('allow symmetry on all boundaries',1);

addmesh;

# set Geometry
set("x",0);
set("x span",4.9e-6);
set("y",0.75e-6);
set("y span",2.5e-6);
set("z",0);
set("z span",10e-6);


# enable in X and Ydirection and disable in Z directions

set("override x mesh",1);
set("override y mesh",1);
set("override z mesh",0);
# restrict mesh by defining maximum step size
set("set maximum mesh step",1);
set("dx",0.01e-6);
set("dy",0.01e-6);


findmodes;
```

A.3 Mask design of spiral rib waveguide with L-edit

```
//////////////////////// main function ////////////////////////////////////
void MACRONAME(void)
{

//////////////////////Set up layers////////////////
LCell   pCell = LCell_GetVisible();
LFile   pFile = LCell_GetFile(pCell);
LPoint centre = LPoint_Set(0, 0);

//Initialize default layers:
layers_CLASS layers;
layers.list = layers.setdefaultlist(pFile);

//To add compatibility with previous code,
transfer layers.list into LLayer array "layer":
LLayer layer[25];
for (int a = 0; a < layers.list.size(); a++) layer[a] = layers.list[a];
//copy all elements of "layers" vector into "layer" array


//////  1. declare all component types, and set all common variables:

/* //Declare grating coupler struct and set variables:
GratingCoupler_TYPE GC;
GC.Period = 1.96 * 1000;
GC.W_grat = 25 * 1000;
GC.L_grat = 50 * 1000;
GC.W_wg = 10 * 1000;
GC.angle = 0;
GC.InPort = centre; */

//Declare waveguide struct and variables:
WG_TYPE WG;
WG.W = 3.8 * 1000;
WG.angle = 0;
WG.L = 500 * 1000;

// 1 Declare waveguide struct and variables:
WG_TYPE WG_cl;
WG_cl.W = 25 * 1000;
WG_cl.angle = 0;
WG_cl.L = 500 * 1000;

//Declare input taper struct and set variables;
Taper_TYPE TAPin;
TAPin.W1 = WG_cl.W ;
TAPin.W2 = WG.W;
TAPin.angle = 0;
TAPin.L = 5000*1000;;

//Declare output taper struct and set variables;
Taper_TYPE TAPout;
TAPout.W1 = WG.W;
TAPout.W2 = WG_cl.W ;
TAPout.angle = 0;
TAPout.L = TAPin.L;
```

```
//Declare Bend and set variables
long R=85*1000;
bend_TYPE Bend;
Bend.W = WG.W;
Bend.radius = R;

//1.5 Declare Spiral
Spiral_TYPE Spiral1;
Spiral1.gap = 7*1000;
Spiral1.n = 0;
Spiral1.R1 = R;
Spiral1.orient =-1;

/////// 2. Draw waveguides of different lengths, with with butt coupling both LHS and RHS:
long dyi = 700*1000;
int i, j;
int n = 7;                      //Set number of spiral waveguides
//long d_length = 100 * 1000;   //Set difference in length between each variation
long L0 = 2500 * 1000;          //Set the length of the shortest waveguide
long offset = 100 * 1000;               //Set offset between adjacent waveguides.
long L_total = 4000 * 1000;

long out_offset = 200 * 1000;

for (i = 0; i<n; i++)
{
//First set the changing length for each iteration
long PL_in = 2000*1000;
long PL_mid = 5000*1000;
long PL_out = 2000*1000;
long BendSep = PL_mid-PL_in-PL_out-2*R;



//0 Now draw butt coupling input section WG ,taper:
WG_cl.InPort.x = centre.x;      //Set LHS grating start point.
WG_cl.InPort.y = centre.y + i*2*(out_offset + offset + 4 * Bend.radius)+ i*dyi;
waveguide(pCell, layer[0], WG_cl, WG_cl.OutPort);

TAPin.InPort = WG_cl.OutPort;
TAPin.angle = 0;
Taper(pCell, layer[0], TAPin, TAPin.OutPort);

//1 Draw length of waveguide to the first bend:
WG.L = (L_total - BendSep) / 2;
WG.InPort = TAPin.OutPort;
waveguide(pCell, layer[0], WG, WG.OutPort);

//Draw first two input bends
Bend.InPort = WG.OutPort;
Bend.start_angle = 0;
Bend.end_angle = 90;
bend(pCell, layer[0], Bend, Bend.OutPort);      //bend 1

Bend.InPort = Bend.OutPort;
Bend.start_angle = 90;
Bend.end_angle = 180;
bend(pCell, layer[0], Bend, Bend.OutPort);      //bend 2
```

```
//2 Draw Prop loss section waveguide input part
WG.angle = 180;
WG.L = PL_in;
WG.InPort = Bend.OutPort;
waveguide(pCell, layer[0], WG, WG.OutPort);

//Draw two bends to middle part
Bend.InPort = WG.OutPort;
Bend.start_angle = 180;
Bend.end_angle = 90;
bend(pCell, layer[0], Bend, Bend.OutPort);      //bend 1

Bend.InPort = Bend.OutPort;
Bend.start_angle = 90;
Bend.end_angle = 0;
bend(pCell, layer[0], Bend, Bend.OutPort);      //bend 2


// Draw spiral input waveguide:
//3
WG.angle = 0;
WG.L= PL_in;
WG.InPort = Bend.OutPort;
waveguide(pCell, layer[0], WG, WG.OutPort);     //Draw spiral input waveguide


/* WG.L = centre.x + 5000 * 1000 - Spiral1.OutPort.x; */

/* //Draw Prop loss section waveguide middle part
WG.angle = 0;
WG.L = 500*1000;PL_mid;
WG.InPort = Bend.OutPort;
waveguide(pCell, layer[0], WG, WG.OutPort); */

// 2.2 Draw spiral1 :
Spiral1.InPort = WG.OutPort;
Spiral1.n = 1+ i;
Spiral1.R1 = R;
Spiral(pCell, layer[0], Spiral1, WG, Spiral1.OutPort);

//4 Draw spiral output waveguide:
WG.angle = 0;
WG.InPort = Spiral1.OutPort;
WG.L = PL_mid- (Spiral1.OutPort.x-Spiral1.InPort.x)-PL_in;
long L_mr = WG.L;
long distance = Spiral1.OutPort.x-Spiral1.InPort.x;
waveguide(pCell, layer[0], WG, WG.OutPort);

//Draw two bends to output waveguide part
Bend.InPort =  WG.OutPort;
Bend.start_angle = 0;
Bend.end_angle = 270;
bend(pCell, layer[0], Bend, Bend.OutPort);

Bend.InPort = Bend.OutPort;
Bend.start_angle = 270;
Bend.end_angle = 180;
bend(pCell, layer[0], Bend, Bend.OutPort);
```

```
//5 Draw Prop loss section waveguide output part
WG.angle = 180;
WG.L = PL_out;
WG.InPort = Bend.OutPort;
waveguide(pCell, layer[0], WG, WG.OutPort);

//Draw final two bends to chip output
Bend.InPort = WG.OutPort;
Bend.start_angle = 180;
Bend.end_angle = 270;
bend(pCell, layer[0], Bend, Bend.OutPort);      //bend 1

//6 Draw input/output offset waveguide
WG.angle = 270;
WG.L = out_offset;
WG.InPort = Bend.OutPort;
waveguide(pCell, layer[0], WG, WG.OutPort);

Bend.InPort = WG.OutPort;
Bend.start_angle = 270;
Bend.end_angle = 0;
bend(pCell, layer[0], Bend, Bend.OutPort);      //bend 2

//7 Draw length of waveguide to output taper:
WG.L = (L_total - BendSep) / 2;
WG.InPort = Bend.OutPort;
WG.angle = 0;
waveguide(pCell, layer[0], WG, WG.OutPort);



TAPout.InPort = WG.OutPort;     //Set LHS taper staring point
Taper(pCell, layer[0], TAPout, TAPout.OutPort); //Draw LHS Taper

WG_cl.InPort = TAPout.OutPort;  //Set LHS grating start point.
TAPout.angle = 0;
waveguide(pCell, layer[0], WG_cl, WG_cl.OutPort);       //Draw LHS grating.




//Now draw butt coupling input section:
WG_cl.InPort.x = centre.x;
WG_cl.InPort.y = centre.y + (i+1)*2*(out_offset + offset + 4 * Bend.radius)+ i*dyi;
waveguide(pCell, layer[0], WG_cl, WG_cl.OutPort);

TAPin.InPort = WG_cl.OutPort;
TAPin.angle = 0;
Taper(pCell, layer[0], TAPin, TAPin.OutPort);

//Draw length of waveguide to the first bend:
WG.L = (L_total - BendSep) / 2;
WG.InPort = TAPin.OutPort;
waveguide(pCell, layer[0], WG, WG.OutPort);

//Draw first two input bends
```

```
Bend.InPort = WG.OutPort;
Bend.start_angle = 0;
Bend.end_angle = 90;
bend(pCell, layer[0], Bend, Bend.OutPort);      //bend 1

Bend.InPort = Bend.OutPort;
Bend.start_angle = 90;
Bend.end_angle = 180;
bend(pCell, layer[0], Bend, Bend.OutPort);      //bend 2

//Draw Prop loss section waveguide input part
WG.angle = 180;
WG.L = PL_in-distance/2;
WG.InPort = Bend.OutPort;
waveguide(pCell, layer[0], WG, WG.OutPort);

//Draw two bends to middle part
Bend.InPort = WG.OutPort;
Bend.start_angle = 180;
Bend.end_angle = 90;
bend(pCell, layer[0], Bend, Bend.OutPort);      //bend 1

Bend.InPort = Bend.OutPort;
Bend.start_angle = 90;
Bend.end_angle = 0;
bend(pCell, layer[0], Bend, Bend.OutPort);      //bend 2


// 2.1 Draw spiral input waveguide:
WG.angle = 0;
WG.L= PL_in+distance/2;
WG.InPort = Bend.OutPort;
waveguide(pCell, layer[0], WG, WG.OutPort);


/* WG.L = centre.x + 5000 * 1000 - Spiral1.OutPort.x; */

/* //Draw Prop loss section waveguide middle part
WG.angle = 0;
WG.L = 500*1000;PL_mid;
WG.InPort = Bend.OutPort;
waveguide(pCell, layer[0], WG, WG.OutPort); */

// 2.2 Draw spiral1 :
//Spiral1.InPort = WG.OutPort;
//Spiral1.n = 1+ i;
//Spiral1.R1 = R;
//Spiral(pCell, layer[0], Spiral1, WG, Spiral1.OutPort);

// 2.3 Draw spiral output waveguide:
WG.angle = 0;
WG.InPort = WG.OutPort;
WG.L = PL_mid- (Spiral1.OutPort.x-Spiral1.InPort.x)-PL_in;
//long L_mr = WG.L;
//long distance = Spiral1.OutPort.x-Spiral1.InPort.x;
waveguide(pCell, layer[0], WG, WG.OutPort);     //Draw spiral output waveguide

//Draw two bends to output waveguide part
Bend.InPort =  WG.OutPort;
```

```
Bend.start_angle = 0;
Bend.end_angle = 270;
bend(pCell, layer[0], Bend, Bend.OutPort);      //bend 1

Bend.InPort = Bend.OutPort;
Bend.start_angle = 270;
Bend.end_angle = 180;
bend(pCell, layer[0], Bend, Bend.OutPort);      //bend 2

//Draw Prop loss section waveguide output part
WG.angle = 180;
WG.L = PL_out;
WG.InPort = Bend.OutPort;
waveguide(pCell, layer[0], WG, WG.OutPort);

//Draw final two bends to chip output
Bend.InPort = WG.OutPort;
Bend.start_angle = 180;
Bend.end_angle = 270;
bend(pCell, layer[0], Bend, Bend.OutPort);      //bend 1

//Draw input/output offset waveguide
WG.angle = 270;
WG.L = out_offset;
WG.InPort = Bend.OutPort;
waveguide(pCell, layer[0], WG, WG.OutPort);

Bend.InPort = WG.OutPort;
Bend.start_angle = 270;
Bend.end_angle = 0;
bend(pCell, layer[0], Bend, Bend.OutPort);      //bend 2

//Draw length of waveguide to output taper:
WG.L = (L_total - BendSep) / 2;
WG.InPort = Bend.OutPort;
WG.angle = 0;
waveguide(pCell, layer[0], WG, WG.OutPort);

//Draw Butt coupling output section:
//WG.InPort = Bend.OutPort;     //Set waveguide start point
//WG.L = L_total - (Bend.OutPort.x - TAPin.OutPort.x);  //Change wg length
//waveguide(pCell, layer[0], WG, WG.OutPort);   //Draw waveguide

TAPout.InPort = WG.OutPort;     //Set LHS taper staring point
Taper(pCell, layer[0], TAPout, TAPout.OutPort); //Draw LHS Taper

WG_cl.InPort = TAPout.OutPort;  //Set LHS grating start point.
TAPout.angle = 0;
waveguide(pCell, layer[0], WG_cl, WG_cl.OutPort);       //Draw LHS grating.

}//end for

}//end PropLossButt_offset (end main)


2 prop loss waveguide


////////////////////////// main function ////////////////////////////////////
```

```
void MACRONAME(void)
{

//////////////////////Set up layers////////////////
LCell   pCell = LCell_GetVisible();
LFile   pFile = LCell_GetFile(pCell);
LPoint centre = LPoint_Set(0, 0);

//Initialize default layers:
layers_CLASS layers;
layers.list = layers.setdefaultlist(pFile);

//To add compatibility with previous code, transfer layers.list into LLayer array "layer":
LLayer layer[25];
for (int a = 0; a < layers.list.size(); a++) layer[a] = layers.list[a];


//////  1. declare all component types, and set all common variables:

/* //Declare grating coupler struct and set variables:
GratingCoupler_TYPE GC;
GC.Period = 1.96 * 1000;
GC.W_grat = 25 * 1000;
GC.L_grat = 50 * 1000;
GC.W_wg = 10 * 1000;
GC.angle = 0;
GC.InPort = centre; */

//Declare waveguide struct and variables:
WG_TYPE WG;
WG.W = 3.8 * 1000;
WG.angle = 0;
WG.L = 500 * 1000;

// 1 Declare waveguide struct and variables:
WG_TYPE WG_cl;
WG_cl.W = 25 * 1000;
WG_cl.angle = 0;
WG_cl.L = 500 * 1000;

//Declare input taper struct and set variables;
Taper_TYPE TAPin;
TAPin.W1 = WG_cl.W ;
TAPin.W2 = WG.W;
TAPin.angle = 0;
TAPin.L = 5000*1000;;

//Declare output taper struct and set variables;
Taper_TYPE TAPout;
TAPout.W1 = WG.W;
TAPout.W2 = WG_cl.W ;
TAPout.angle = 0;
TAPout.L = TAPin.L;

//Declare Bend and set variables
long R=85*1000;
bend_TYPE Bend;
Bend.W = WG.W;
Bend.radius = R;
```

```
/////// 2. Draw waveguides of different lengths, with with butt coupling both LHS and RHS:
int i, j;
int n_lengths = 5;                      //Set number of length variations
long d_length = 1500 * 1000;    //Set difference in length between each variation
long L0 = 2500 * 1000;          //Set the length of the shortest waveguide
long offset = 100 * 1000;               //Set offset between adjacent waveguides.
long L_total = 4000 * 1000;
long BendSep = 100 * 1000;
long out_offset = 200 * 1000;
// L_min=L0+2*Bend.radius+BendSep=2753.2*1000,
//difference length= d_length =1500*1000
for (i = 0; i<n_lengths; i++)
{
//First set the changing length for each iteration
long PL_in = (L0 + i*d_length) / 4;
long PL_mid = 2 * Bend.radius + BendSep + (L0 + i*d_length) / 2;
long PL_out = (L0 + i*d_length) / 4;



//Draw grating coupler section:
//GC.InPort.x = centre.x;       //Set LHS grating start point.
//GC.InPort.y = centre.y + i*(offset + 4 * Bend.radius);
//GratingCoupler(pFile, pCell, layer, GC, GC.OutPort);


//Now draw butt coupling input section:
WG_cl.InPort.x = centre.x;      //Set LHS grating start point.
WG_cl.InPort.y = centre.y -i*(out_offset + offset + 4 * Bend.radius)-9000*1000;
waveguide(pCell, layer[0], WG_cl, WG_cl.OutPort);       //Draw LHS grating.

TAPin.InPort = WG_cl.OutPort;   //Set LHS taper staring point
TAPin.angle = 0;
Taper(pCell, layer[0], TAPin, TAPin.OutPort);   //Draw LHS Taper

//Draw length of waveguide to the first bend:
WG.L = (L_total - BendSep) / 2;
WG.InPort = TAPin.OutPort;
waveguide(pCell, layer[0], WG, WG.OutPort);

//Draw first two input bends
Bend.InPort = WG.OutPort;
Bend.start_angle = 0;
Bend.end_angle = 90;
bend(pCell, layer[0], Bend, Bend.OutPort);      //bend 1

Bend.InPort = Bend.OutPort;
Bend.start_angle = 90;
Bend.end_angle = 180;
bend(pCell, layer[0], Bend, Bend.OutPort);      //bend 2

//Draw Prop loss section waveguide input part
WG.angle = 180;
WG.L = PL_in;
WG.InPort = Bend.OutPort;
waveguide(pCell, layer[0], WG, WG.OutPort);
```

```
//Draw two bends to middle part
Bend.InPort = WG.OutPort;
Bend.start_angle = 180;
Bend.end_angle = 90;
bend(pCell, layer[0], Bend, Bend.OutPort);      //bend 1

Bend.InPort = Bend.OutPort;
Bend.start_angle = 90;
Bend.end_angle = 0;
bend(pCell, layer[0], Bend, Bend.OutPort);      //bend 2

//Draw Prop loss section waveguide middle part
WG.angle = 0;
WG.L = PL_mid;
WG.InPort = Bend.OutPort;
waveguide(pCell, layer[0], WG, WG.OutPort);

//Draw two bends to output waveguide part
Bend.InPort = WG.OutPort;
Bend.start_angle = 0;
Bend.end_angle = 270;
bend(pCell, layer[0], Bend, Bend.OutPort);      //bend 1

Bend.InPort = Bend.OutPort;
Bend.start_angle = 270;
Bend.end_angle = 180;
bend(pCell, layer[0], Bend, Bend.OutPort);      //bend 2

//Draw Prop loss section waveguide output part
WG.angle = 180;
WG.L = PL_out;
WG.InPort = Bend.OutPort;
waveguide(pCell, layer[0], WG, WG.OutPort);

//Draw final two bends to chip output
Bend.InPort = WG.OutPort;
Bend.start_angle = 180;
Bend.end_angle = 270;
bend(pCell, layer[0], Bend, Bend.OutPort);      //bend 1

//Draw input/output offset waveguide
WG.angle = 270;
WG.L = out_offset;
WG.InPort = Bend.OutPort;
waveguide(pCell, layer[0], WG, WG.OutPort);

Bend.InPort = WG.OutPort;
Bend.start_angle = 270;
Bend.end_angle = 0;
bend(pCell, layer[0], Bend, Bend.OutPort);      //bend 2

//Draw length of waveguide to output taper:
WG.L = (L_total - BendSep) / 2;
WG.InPort = Bend.OutPort;
WG.angle = 0;
waveguide(pCell, layer[0], WG, WG.OutPort);

//Draw Butt coupling output section:
//WG.InPort = Bend.OutPort;     //Set waveguide start point
```

```
//WG.L = L_total - (Bend.OutPort.x - TAPin.OutPort.x);  //Change wg length
//waveguide(pCell, layer[0], WG, WG.OutPort);   //Draw waveguide

TAPout.InPort = WG.OutPort;     //Set LHS taper staring point
Taper(pCell, layer[0], TAPout, TAPout.OutPort); //Draw LHS Taper

WG_cl.InPort = TAPout.OutPort;  //Set LHS grating start point.
TAPout.angle = 0;
waveguide(pCell, layer[0], WG_cl, WG_cl.OutPort);       //Draw LHS grating.


}//end for

}//end PropLossButt_offset (end main)


Write label text- spiral + reference waveguide

////////////////////////// main function ////////////////////////////////////
void MACRONAME(void)
{

//////////////////////Set up layers////////////////
LCell   pCell = LCell_GetVisible();
LFile   pFile = LCell_GetFile(pCell);
LPoint centre = LPoint_Set(0,0);
//LStatus statusLay = LLayer_New(pFile, LLayer_Find(pFile, "New Layer"), "Layer1");
LLayer pLayer = LLayer_Find(pFile, "labels");

// Set text size:
long txtSize = 100 * 1000;

// Initialise string variables:
std::stringstream sstm;
string name;
char *InName;

int n=7;
int i;
long dyi = 700*1000;
long out_offset = 200 * 1000;
long R=85*1000;
long offset = 100 * 1000;               //Set offset between adjacent waveguides.


for (i = 0; i < n; i++)
{
sstm << "N" <<  1+i << "-W" << 3.8;     //append different parts of name to string

name = sstm.str();      //create string in "name" from stringstream
char *innamechar = new char[name.length() + 1];
std::strcpy(innamechar, name.c_str());
sstm.str(std::string());

// Change y-position:
centre.x = centre.x ;
centre.y = centre.y + 2000*1000;        //Set textLabel start point.
//Draw text:
textLabel(pCell, pLayer, centre, innamechar, txtSize);
```

```
}

}//end BendLossButt (end main)

Write label text-prop loss waveguide




////////////////////////// main function ////////////////////////////////////
void MACRONAME(void)
{
//////////////////////Set up layers////////////////
LCell   pCell = LCell_GetVisible();
LFile   pFile = LCell_GetFile(pCell);
LPoint centre = LPoint_Set(0,0);
//LStatus statusLay = LLayer_New(pFile, LLayer_Find(pFile, "New Layer"), "Layer1");
LLayer pLayer = LLayer_Find(pFile, "labels");
// Initialise string variables:
std::stringstream sstm;
string name;
char *InName;


int n=5;
int i;
long d_length = 2000*1000;
long dyi = 700*1000;
long out_offset = 200 * 1000;
long R=85*1000;
long offset = 100 * 1000;

// Set text size:
long txtSize = 100 * 1000;
for (i = 0; i < n; i++)
{
sstm  << "L" <<  2753.2+i*d_length << "-W" << 3.8;
/*  sstm << "N" <<  1+i << "-W" << 3.7;  */
name = sstm.str();      //create string in "name" from stringstream
char *innamechar = new char[name.length() + 1];
std::strcpy(innamechar, name.c_str());
sstm.str(std::string());

// Change y-position:
centre.x = centre.x ;
centre.y = centre.y + 600*1000; //Set textLabel start point.
//Draw text:
textLabel(pCell, pLayer, centre, innamechar, txtSize);

}


}//end BendLossButt (end main)
```

References

[1] E. O. Voit, "Biochemical systems theory: a review," *International Scholarly Research Notices*, vol. 2013, 2013.

[2] A. Kumar *et al.*, "Biosensors based on piezoelectric crystal detectors: theory and application," *JOM-e*, vol. 52, no. 10, pp. 1–6, 2000.

[3] S. Coyle, V. F. Curto, F. Benito-Lopez, L. Florea, and D. Diamond, "Wearable bio and chemical sensors," in *Wearable sensors*. Elsevier, 2014, pp. 65–83.

[4] M. S.-C. Lu, "Lecture 5 biochemical sensor," https://www.ee.nthu.edu.tw/sclu/biosensor.pdf.

[5] P. M. Gschwend *et al.*, *Environmental organic chemistry*. John Wiley & Sons, 2016.

[6] A. Rao, M. Avula, and D. Grainger, "3.34 biomaterials challenges in continuous glucose monitors in vivo," in *Comprehensive Biomaterials II*, P. Ducheyne, Ed. Oxford: Elsevier, 2017, pp. 755–770. [Online]. Available: https://www.sciencedirect.com/science/article/pii/B9780128035818093140

[7] S. B. Hall, E. A. Khudaish, and A. L. Hart, "Electrochemical oxidation of hydrogen peroxide at platinum electrodes. part 1. an adsorption-controlled mechanism," *Electrochimica Acta*, vol. 43, no. 5-6, pp. 579–588, 1998.

[8] E. Bakker and M. Telting-Diaz, "Electrochemical sensors," *Analytical chemistry*, vol. 74, no. 12, pp. 2781–2800, 2002.

[9] P. Patimisco, G. Scamarcio, F. K. Tittel, and V. Spagnolo, "Quartz-enhanced photoacoustic spectroscopy: a review," *Sensors*, vol. 14, no. 4, pp. 6165–6206, 2014.

[10] I. Galli, S. Bartalini, S. Borri, P. Cancio, D. Mazzotti, P. De Natale, and G. Giusfredi, "Molecular gas sensing below parts per trillion: radiocarbon-dioxide optical detection," *Physical Review Letters*, vol. 107, no. 27, p. 270802, 2011.

[11] G. Shruthi, C. Amitha, and B. B. Mathew, "Biosensors: a modern day achievement," *J Instrument Technol*, vol. 2, pp. 26–39, 2014.

[12] A. Gutierrez-Arroyo, E. Baudet, L. Bodiou, V. Nazabal, E. Rinnert, K. Michel, B. Bureau, F. Colas, and J. Charrier, "Theoretical study of an evanescent optical integrated sensor for multipurpose detection of gases and liquids in the mid-infrared," *Sensors and Actuators B: Chemical*, vol. 242, pp. 842–848, 2017.

[13] K. Kneipp, Y. Wang, H. Kneipp, L. T. Perelman, I. Itzkan, R. R. Dasari, and M. S. Feld, "Single molecule detection using surface-enhanced raman scattering (sers)," *Physical review letters*, vol. 78, no. 9, p. 1667, 1997.

[14] J. C. Lindon, G. E. Tranter, and D. Koppenaal, *Encyclopedia of spectroscopy and spectrometry*. Academic Press, 2016.

[15] D. Caffey, M. B. Radunsky, V. Cook, M. Weida, P. R. Buerki, S. Crivello, and T. Day, "Recent results from broadly tunable external cavity quantum cascade lasers," in *Novel In-Plane Semiconductor Lasers X*, vol. 7953. International Society for Optics and Photonics, 2011, p. 79531K.

[16] M. Sigrist, "Trace gas monitoring by laser-photoacoustic spectroscopy," *Infrared Physics & Technology*, vol. 36, no. 1, pp. 415–425, 1995.

[17] G. Giubileo and A. Puiu, "Photoacoustic spectroscopy of standard explosives in the mir region," *Nuclear Instruments and Methods in Physics Research Section A: Accelerators, Spectrometers, Detectors and Associated Equipment*, vol. 623, no. 2, pp. 771–777, 2010.

[18] C. Wang and P. Sahay, "Breath analysis using laser spectroscopic techniques: breath biomarkers, spectral fingerprints, and detection limits," *Sensors*, vol. 9, no. 10, pp. 8230–8262, 2009.

[19] A. Ergin, R. Greene, and G. Thomas, "Spectroscopic distinguishability of glucose from tissues in the porcine eye," in *IEEE 30th Annual Northeast Bioengineering Conference, 2004. Proceedings of the.* IEEE, 2004, pp. 233–234.

[20] P. Skolik, M. R. McAinsh, and F. L. Martin, "Biospectroscopy for plant and crop science," in *Comprehensive analytical chemistry.* Elsevier, 2018, vol. 80, pp. 15–49.

[21] B. Stuart, "Infrared spectroscopy," *Kirk-Othmer encyclopedia of chemical technology*, 2000.

[22] A. Gutierrez-Arroyo, L. Bodiou, J. Lemaitre, E. Baudet, M. Baillieul, I. Hardy, C. Caillaud, F. Colas, K. Boukerma, E. Rinnert *et al.*, "Development of integrated platform based on chalcogenides for sensing applications in the mid-infrared," in *Integrated Optics: Devices, Materials, and Technologies XXII*, vol. 10535. International Society for Optics and Photonics, 2018, p. 1053513.

[23] W. Li, P. Anantha, K. H. Lee, H. D. Qiu, X. Guo, S. C. K. Goh, L. Zhang, H. Wang, R. A. Soref, and C. S. Tan, "Spiral waveguides on germanium-on-silicon nitride platform for mid-ir sensing applications," *IEEE Photonics Journal*, vol. 10, no. 3, pp. 1–7, 2018.

[24] V. M. Passaro, B. Troia, and F. De Leonardis, "Group iv photonic slot structures for highly efficient gas sensing in mid-ir," in *Proceedings of IARIA Conference on Sensor Device Technologies and Applications*, 2011, pp. 103–108.

[25] A. D. McNaught, A. Wilkinson *et al.*, *Compendium of chemical terminology*. Blackwell Science Oxford, 1997, vol. 1669.

[26] F. F. Crim, "Bond-selected chemistry: vibrational state control of photodissociation and bimolecular reaction," *The Journal of Physical Chemistry*, vol. 100, no. 31, pp. 12 725–12 734, 1996.

[27] A. M. Katzenmeyer, G. Holland, K. Kjoller, and A. Centrone, "Absorption spectroscopy and imaging from the visible through mid-infrared with 20 nm resolution," *Analytical chemistry*, vol. 87, no. 6, pp. 3154–3159, 2015.

[28] Chemistry, "Infrared spectroscopy," https://chem.libretexts.org/Bookshelves/Physical_and_Theoretical_Chemistry_Textbook_Maps/Supplemental_Modules_(Physical_and_Theoretical_Chemistry)/Spectroscopy/Vibrational_Spectroscopy/Infrared_Spectroscopy/Infrared_Spectroscopy.

[29] K. B. Bec, J. Grabska, Y. Ozaki, J. P. Hawranek, and C. W. Huck, "Influence of non-fundamental modes on mid-infrared spectra: anharmonic dft study of aliphatic ethers," *The Journal of Physical Chemistry A*, vol. 121, no. 7, pp. 1412–1424, 2017.

[30] L. Amand and C. Tullin, "The theory behind ftir analysis–application examples from measurement at the 12 mw circulating fluidized bed boiler at chalmers," *CECOST, Lund University, Sweden*, 1999.

[31] M. Paraskevaidi, P. L. Martin-Hirsch, and F. L. Martin, "Atr-ftir spectroscopy tools for medical diagnosis and disease investigation," in *Nanotechnology Characterization Tools for Biosensing and Medical Diagnosis*. Springer, 2018, pp. 163–211.

[32] S. De Bruyne, M. M. Speeckaert, and J. R. Delanghe, "Applications of mid-infrared spectroscopy in the clinical laboratory setting," *Critical reviews in clinical laboratory sciences*, vol. 55, no. 1, pp. 1–20, 2018.

[33] S. Lebedkin, K. Arnold, F. Hennrich, R. Krupke, B. Renker, and M. M. Kappes, "Ftir-luminescence mapping of dispersed single-walled carbon nanotubes," *New Journal of Physics*, vol. 5, no. 1, p. 140, 2003.

[34] D. R. Smith, R. L. Morgan, and E. V. Loewenstein, "Comparison of the radiance of far-infrared sources," *JOSA*, vol. 58, no. 3, pp. 433–434, 1968.

[35] Y. Chen, C. Zou, M. Mastalerz, S. Hu, C. Gasaway, and X. Tao, "Applications of micro-fourier transform infrared spectroscopy (ftir) in the geological sciences—a review," *International journal of molecular sciences*, vol. 16, no. 12, pp. 30 223–30 250, 2015.

[36] A. P. Michel, P. Q. Liu, J. K. Yeung, P. Corrigan, M. L. Baeck, Z. Wang, T. Day, F. Moshary, C. F. Gmachl, and J. A. Smith, "Quantum cascade laser open-path system for remote sensing of trace gases in beijing, china," *Optical Engineering*, vol. 49, no. 11, p. 111125, 2010.

[37] J. Midwinter, "Evanescent field coupling into a thin-film waveguide," *IEEE Journal of Quantum Electronics*, vol. 6, no. 10, pp. 583–590, 1970.

[38] V. M. Lavchiev, B. Jakoby, U. Hedenig, T. Grille, P. Irsigler, G. Ritchie, J. Kirkbride, and B. Lendl, "Silicon photonics in the mid-infrared: Waveguide absorption sensors," in *SENSORS, 2014 IEEE*. IEEE, 2014, pp. 645–648.

[39] J. Charrier, M.-L. Brandily, H. Lhermite, K. Michel, B. Bureau, F. Verger, and V. Nazabal, "Evanescent wave optical micro-sensor based on chalcogenide glass," *Sensors and Actuators B: Chemical*, vol. 173, pp. 468–476, 2012.

[40] R. Soref, "Mid-infrared photonics in silicon and germanium," *Nature photonics*, vol. 4, no. 8, pp. 495–497, 2010.

[41] V. Mittal, M. Nedeljkovic, D. J. Rowe, G. S. Murugan, and J. S. Wilkinson, "Chalcogenide glass waveguides with paper-based fluidics for mid-infrared absorption spectroscopy," *Optics letters*, vol. 43, no. 12, pp. 2913–2916, 2018.

[42] M. Nedeljkovic, J. S. Penadés, C. J. Mitchell, A. Z. Khokhar, S. Stankovic, T. D. Bucio, C. G. Littlejohns, F. Y. Gardes, and G. Z. Mashanovich, "Surface-grating-coupled low-loss ge-on-si rib waveguides and multimode interferometers," *IEEE Photon. Technol. Lett.*, vol. 27, no. 10, pp. 1040–1043, 2015.

[43] M. Nedeljkovic, A. Khokhar, Y. Hu, X. Chen, J. S. Penades, S. Stankovic, H. Chong, D. Thomson, F. Gardes, G. Reed *et al.*, "Silicon photonic devices and platforms for the mid-infrared," *Optical Materials Express*, vol. 3, no. 9, pp. 1205–1214, 2013.

[44] G. Z. Mashanovich, F. Y. Gardes, D. J. Thomson, Y. Hu, K. Li, M. Nedeljkovic, J. S. Penades, A. Z. Khokhar, C. J. Mitchell, S. Stankovic *et al.*, "Silicon photonic waveguides and devices for near-and mid-ir applications," *IEEE J. Sel. Top. Quantum Electron.*, vol. 21, no. 4, p. 8200112, 2015.

[45] P. Steglich and K. You, "Silicon-on-insulator slot waveguides: Theory and applications in electro-optics and optical sensing," in *Emerging Waveguide Technology*. IntechOpen, 2018, pp. 187–210.

[46] P. T. Lin, S. W. Kwok, H.-Y. G. Lin, V. Singh, L. C. Kimerling, G. M. Whitesides, and A. Agarwal, "Mid-infrared spectrometer using opto-nanofluidic slot-waveguide for label-free on-chip chemical sensing," *Nano letters*, vol. 14, no. 1, pp. 231–238, 2013.

[47] J. S. Penadés, A. Z. Khokhar, M. Nedeljkovic, and G. Z. Mashanovich, "Low-loss mid-infrared soi slot waveguides," *IEEE Photonics Technology Letters*, vol. 27, no. 11, pp. 1197–1199, 2015.

[48] U. Younis, A. A. Bettiol, and K.-W. Ang, "Mid-infrared waveguides in ge-on-soi," in *Optical MEMS and Nanophotonics (OMN), 2016 International Conference on*. IEEE, 2016, pp. 1–2.

[49] R. Kitamura, L. Pilon, and M. Jonasz, "Optical constants of silica glass from extreme ultraviolet to far infrared at near room temperature," *Applied optics*, vol. 46, no. 33, pp. 8118–8133, 2007.

[50] Y.-C. Chang, V. Paeder, L. Hvozdara, J.-M. Hartmann, and H. P. Herzig, "Low-loss germanium strip waveguides on silicon for the mid-infrared," *Optics letters*, vol. 37, no. 14, pp. 2883–2885, 2012.

[51] K. Gallacher, L. Baldassarre, R. W. Millar, A. Sorgi, V. Giliberti, J. Frigerio, G. Isella, I. Figliolia, P. Biagioni, M. Ortolani *et al.*, "Germanium-on-silicon waveguides for mid-infrared photonic sensing chips," in *Group IV Photonics (GFP), 2017 IEEE 14th International Conference on*. IEEE, 2017, pp. 63–64.

[52] M. Nedeljkovic, J. S. Penades, V. Mittal, G. S. Murugan, A. Z. Khokhar, C. Littlejohns, L. G. Carpenter, C. B. Gawith, J. S. Wilkinson, and G. Z. Mashanovich, "Germanium-on-silicon waveguides operating at mid-infrared wavelengths up to 8.5 μm," *Optics express*, vol. 25, no. 22, pp. 27 431–27 441, 2017.

[53] M. Montesinos-Ballester, V. Vakarin, Q. Liu, X. Le Roux, J. Frigerio, A. Ballabio, A. Barzaghi, C. Alonso-Ramos, L. Vivien, G. Isella *et al.*, "Ge-rich graded sige waveguides and interferometers from 5 to 11 μm wavelength range," *Optics express*, vol. 28, no. 9, pp. 12 771–12 779, 2020.

[54] J. Ramirez, Q. Liu, V. Vakarin, J. Frigerio, A. Ballabio, X. Le Roux, D. Bouville, L. Vivien, G. Isella, and D. Marris-Morini, "Graded sige waveguides with broadband low-loss propagation in the mid infrared," *Optics express*, vol. 26, no. 2, pp. 870–877, 2018.

[55] J. S. Penadés, A. Sánchez-Postigo, M. Nedeljkovic, A. Ortega-Moñux, J. Wangüemert-Pérez, Y. Xu, R. Halir, Z. Qu, A. Khokhar, A. Osman *et al.*, "Suspended silicon waveguides for long-wave infrared wavelengths," *Optics letters*, vol. 43, no. 4, pp. 795–798, 2018.

[56] G. Coppola, L. Sirleto, I. Rendina, and M. Iodice, "Advance in thermo-optical switches: principles, materials, design, and device structure," *Optical Engineering*, vol. 50, no. 7, p. 071112, 2011.

[57] A. Trenti, M. Borghi, S. Biasi, M. Ghulinyan, F. Ramiro-Manzano, G. Pucker, and L. Pavesi, "Thermo-optic coefficient and nonlinear refractive index of silicon oxynitride waveguides," *AIP Advances*, vol. 8, no. 2, p. 025311, 2018.

[58] E. D. E. Palik, "Chapter3 thermo-opticcoefficients," in *Optical Constants of Solids*. Academic Press, 1997, pp. 115–261.

[59] R. A. Soref, F. De Leonardis, and V. M. Passaro, "Multiple-sagnac-loop mach–zehnder interferometer for wavelength interleaving, thermo-optical switching and matched filteri," *Journal of Lightwave Technology*, vol. 36, no. 22, pp. 5254–5262, 2018.

[60] G. Salceda-Delgado, D. Monzon-Hernandez, A. Martinez-Rios, G. Cardenas-Sevilla, and J. Villatoro, "Optical microfiber mode interferometer for temperature-independent refractometric sensing," *Optics letters*, vol. 37, no. 11, pp. 1974–1976, 2012.

[61] C. Tan and J. Arndt, "Temperature dependence of refractive index of glassy sio2 in the infrared wavelength range," *Journal of Physics and Chemistry of Solids*, vol. 61, no. 8, pp. 1315–1320, 2000.

[62] L. B. Soldano and E. C. Pennings, "Optical multi-mode interference devices based on self-imaging: principles and applications," *Journal of lightwave technology*, vol. 13, no. 4, pp. 615–627, 1995.

[63] K. Cooney and F. H. Peters, "Analysis of multimode interferometers," *Optics express*, vol. 24, no. 20, pp. 22 481–22 515, 2016.

[64] M. Nedeljkovic, "Waveguide splitters and couplers," University Lecture, 2019.

[65] K. Voigt, "Interferometric devices based on 4μm soi material for application in optical telecommunications," 2012.

[66] H. Nikkhah, "Optical switch on a chip: The talbot effect, lüneburg lenses & meta-materials," Ph.D. dissertation, Thesis, University of Ottawa, Canada, 2013.

[67] M. C. Souza, A. Grieco, N. C. Frateschi, and Y. Fainman, "Fourier transform spectrometer on silicon with thermo-optic non-linearity and dispersion correction," *Nature communications*, vol. 9, no. 1, pp. 1–8, 2018.

[68] R. S. El Shamy, D. Khalil, and M. A. Swillam, "Mid infrared optical gas sensor using plasmonic mach-zehnder interferometer," *Scientific Reports*, vol. 10, no. 1, pp. 1–9, 2020.

[69] S. Romero-García, T. Klos, E. Klein, J. Leuermann, D. Geuzebroek, J. van Kerkhof, M. Büscher, J. Krieg, P. Leisching, and J. Witzens, "Photonic integrated circuits for multi-color laser engines," in *Silicon Photonics XII*, vol. 10108. International Society for Optics and Photonics, 2017, p. 101080Z.

[70] M. Nedeljkovic, S. Stanković, C. J. Mitchell, A. Z. Khokhar, S. A. Reynolds, D. J. Thomson, F. Y. Gardes, C. G. Littlejohns, G. T. Reed, and G. Z. Mashanovich, "Mid-infrared thermo-optic modulators in soi," *IEEE Photonics Technology Letters*, vol. 26, no. 13, pp. 1352–1355, 2014.

[71] Y. Gao, Q. Gan, Z. Xin, X. Cheng, and F. J. Bartoli, "Plasmonic mach–zehnder interferometer for ultrasensitive on-chip biosensing," *ACS nano*, vol. 5, no. 12, pp. 9836–9844, 2011.

[72] E. M. Yeatman, "Resolution and sensitivity in surface plasmon microscopy and sensing," *Biosensors and Bioelectronics*, vol. 11, no. 6-7, pp. 635–649, 1996.

[73] D. J. Rowe, D. Smith, and J. S. Wilkinson, "Complex refractive index spectra of whole blood and aqueous solutions of anticoagulants, analgesics and buffers in the mid-infrared," *Scientific reports*, vol. 7, no. 1, pp. 1–9, 2017.

[74] L. Ciaffoni, G. Hancock, J. J. Harrison, J.-P. H. van Helden, C. E. Langley, R. Peverall, G. A. Ritchie, and S. Wood, "Demonstration of a mid-infrared cavity enhanced absorption spectrometer for breath acetone detection," *Analytical chemistry*, vol. 85, no. 2, pp. 846–850, 2013.

[75] Y.-C. Chang, P. Wägli, V. Paeder, A. Homsy, L. Hvozdara, P. van der Wal, J. Di Francesco, N. F. de Rooij, and H. P. Herzig, "Cocaine detection by a mid-infrared waveguide integrated with a microfluidic chip," *Lab on a Chip*, vol. 12, no. 17, pp. 3020–3023, 2012.

[76] A. Kramida, Y. Ralchenko, J. Reader *et al.*, "Nist atomic spectra database (ver. 5.2)," *National Institute of Standards and Technology, Gaithersburg, MD*, 2013.

[77] K. Lumme-Sandt, A. Hervonen, and M. Jylhä, "Interpretative repertoires of medication among the oldest-old," *Social science & medicine*, vol. 50, no. 12, pp. 1843–1850, 2000.

[78] D. S. Krause, B. A. Wolf, and L. M. Shaw, "Acute aspirin overdose: mechanisms of toxicity," *Therapeutic drug monitoring*, vol. 14, pp. 441–441, 1992.

[79] M. Boczar, M. J. Wójcik, K. Szczeponek, D. Jamróz, A. Zieba, and B. Kawałek, "Theoretical modeling of infrared spectra of aspirin and its deuterated derivative," *Chemical physics*, vol. 286, no. 1, pp. 63–79, 2003.

[80] D. Camidge, R. Wood, and D. N. Bateman, "The epidemiology of self-poisoning in the uk," *British journal of clinical pharmacology*, vol. 56, no. 6, pp. 613–619, 2003.

[81] E. Yoon, A. Babar, M. Choudhary, M. Kutner, and N. Pyrsopoulos, "Acetaminophen-induced hepatotoxicity: a comprehensive update," *Journal of clinical and translational hepatology*, vol. 4, no. 2, p. 131, 2016.

[82] S. Heymsfield, T. Lohman, Z. Wang, and S. Going, *Human body composition*. Human kinetics, 2005, vol. 918.

[83] E. Sani and A. Dell'Oro, "Spectral optical constants of ethanol and isopropanol from ultraviolet to far infrared," *Optical Materials*, vol. 60, pp. 137–141, 2016.

[84] D. Calloway, "Beer-lambert law," *Journal of Chemical Education*, vol. 74, no. 7, p. 744, 1997.

[85] A. Gangnaik, Y. M. Georgiev, B. McCarthy, N. Petkov, V. Djara, and J. D. Holmes, "Characterisation of a novel electron beam lithography resist, sml and its comparison to pmma and zep resists," *Microelectronic engineering*, vol. 123, pp. 126–130, 2014.

[86] K. Koshelev, M. Ali Mohammad, T. Fito, K. L. Westra, S. K. Dew, and M. Stepanova, "Comparison between zep and pmma resists for nanoscale electron beam lithography experimentally and by numerical modeling," *Journal of Vacuum Science & Technology B, Nanotechnology and Microelectronics: Materials, Processing, Measurement, and Phenomena*, vol. 29, no. 6, p. 06F306, 2011.

[87] G. T. Edwards, "Fabrication of deep-etched distributed bragg reflectors in algain-p/gaas laser stuctures," Ph.D. dissertation, Cardiff University, 2007.

[88] G. M. Whitesides, "The origins and the future of microfluidics," *Nature*, vol. 442, no. 7101, p. 368, 2006.

[89] O. Ojuroye, R. Torah, and S. Beeby, "Modified pdms packaging of sensory e-textile circuit microsystems for improved robustness with washing," *Microsystem Technologies*, pp. 1–18, 2019.

[90] Thorlabs Inc., "Inf3 fiber specifications*," 2021. [Online]. Available: https://www.thorlabs.com/drawings/fe90fda5f0ea4b8f-4C79C414-02B5-F005-49E555B89A6A0822/P3-32F-FC-2-AutoCADPDF.pdf

[91] InfraRed Associates, Inc., "Insb detectors," 2021. [Online]. Available: http://irassociates.com/index.php?page=insb

[92] S. Recovery, "7265 dual phase dsp lock-in amplifier," https://www.ameteksi.com/products/lock-in-amplifiers/7265-dual-phase-lock-in-amplifier.

[93] P. K. Dixon and L. Wu, "Broadband digital lock-in amplifier techniques," *Review of scientific instruments*, vol. 60, no. 10, pp. 3329–3336, 1989.

[94] Y. Wu, "Group iv mid-infrared waveguide-based bolometers," Ph.D. dissertation, University of Southampton, 2020.

[95] D.C.Stone and J.S.Ellis, "Stats Tutorial - Instrumental Analysis and Calibration," 2020, https://sites.chem.utoronto.ca/chemistry/coursenotes/analsci/stats/ErrRegr.html#errregn.

[96] A. Peczek, C. Mai, G. Winzer, and L. Zimmermann, "Comparison of cut-back method and optical backscatter reflectometry for wafer level waveguide characterization," in *2020 IEEE 33rd International Conference on Microelectronic Test Structures (ICMTS)*. IEEE, 2020, pp. 1–3.

[97] L. Vonghia, L. Leggio, A. Ferrulli, M. Bertini, G. Gasbarrini, G. Addolorato, A. T. S. Group *et al.*, "Acute alcohol intoxication," *European Journal of Internal Medicine*, vol. 19, no. 8, pp. 561–567, 2008.

[98] Z. Han, P. Lin, V. Singh, L. Kimerling, J. Hu, K. Richardson, A. Agarwal, and D. Tan, "On-chip mid-infrared gas detection using chalcogenide glass waveguide," *Applied Physics Letters*, vol. 108, no. 14, p. 141106, 2016.

[99] N. El-Sheimy, H. Hou, and X. Niu, "Analysis and modeling of inertial sensors using allan variance," *IEEE Transactions on instrumentation and measurement*, vol. 57, no. 1, pp. 140–149, 2007.

[100] M. R. Querry, *Optical constants of minerals and other materials from the millimeter to the ultraviolet*. Chemical Research, Development & Engineering Center, US Army Armament, 1987.

[101] Z. Zhu and T. G. Brown, "Full-vectorial finite-difference analysis of microstructured optical fibers," *Optics Express*, vol. 10, no. 17, pp. 853–864, 2002.

[102] Lumerical Support, "Understanding mesh refinement and conformal mesh in fdtd," 2021. [Online]. Available: https://support.lumerical.com/hc/en-us/articles/360034382594-Understanding-Mesh-Refinement-and-Conformal-Mesh-in-FDTD

[103] E. D. Palik, *Handbook of optical constants of solids*. Academic press, 1998, vol. 3.

[104] Y. Mehmood, A. Tariq, U. Jamshaid, and M. Jumshaid, "Uv-visible spectrophotometric method development and validation of assay of iron sucrose injection," *Int J Pure App Biosci*, vol. 3, no. 2, pp. 41–53, 2015.

[105] R. Koeber, C. Fleischer, F. Lanza, K.-S. Boos, B. Sellergren, and D. Barceló, "Evaluation of a multidimensional solid-phase extraction platform for highly selective on-line cleanup and high-throughput lc- ms analysis of triazines in river water samples using molecularly imprinted polymers," *Analytical chemistry*, vol. 73, no. 11, pp. 2437–2444, 2001.

[106] V. Mittal, "Mid-infrared integrated photonic devices for biosensing," Ph.D. dissertation, University of Southampton, 2017.